

## ABSTRACT

Title of Dissertation: INVESTIGATION OF DELAYED  
ETTRINGITE FORMATION DAMAGE  
PROCESS USING SIMULTANEOUS  
NEUTRON AND X-RAY TOMOGRAPHY

Doctor of Philosophy, 2019

Dissertation directed by: Professor Amde M. Amde, Department of Civil  
and Environmental Engineering

Delayed ettringite formation (DEF) is a significant deterioration process in concrete which involves the growth of ettringite  $[\text{Ca}_6\text{Al}_2(\text{SO}_4)_3(\text{OH})_{12} \cdot 26\text{H}_2\text{O}]$  crystals leading to cracking and reduction of compressive strength. Conditions leading to DEF are well known and include among others cement chemistry, presence of humidity, heat curing of concrete structures, and the presence of cracks. The mechanisms and kinetics by which deterioration occur is still not well understood despite numerous investigations. Understanding the mechanism and kinetics of concrete deterioration due to DEF is important in order to prevent such costly deterioration and to improve concrete durability.

In this research, concrete specimens were prepared with type III Portland cement and under different conditions that were designed to either promote or inhibit DEF. These consisted of a control set, a set subjected to a heat cycle and a third set made with elevated potassium content of 1.72% and also thermally cycled. They were tested periodically up to 380 days

by conventional methods such as expansion and weight change measurements and compressive strength testing. Scanning electron microscopy with energy dispersive X-ray analysis (SEM-EDAX) confirmed the presence and the morphology of ettringite in voids at different ages. Simultaneous neutron and X-ray tomography, a new nondestructive microscopic method was used to scan the specimens at regular intervals in order to assess the feasibility of the method in monitoring the progress and characterizing DEF induced damages.

The linear regression analysis of the correlation of expansion with weight change data revealed that expansion and deterioration process occurred in three distinct successive stages. In the first stage, the ettringite fills the pores with little or no expansion; in the second, the expansion appears to be creep due to expansive stresses in the filled pores and in the third stage, crack propagation leads to significant expansion and loss of compressive strength. The results of the linear regression also revealed that the mechanism of DEF is the replacement of pre-existing calcium hydroxide crystals. Through non-linear curve fitting, the kinetic of deterioration was modeled using the Kolmogorov-Avrami-Johnson-Miehl model. The simultaneous neutron and X-ray tomography allowed visualization of the interior of the specimen due to enhance phase segmentation. MATLAB routines were developed to allow for correction for beam hardening and to enhance phase segmentation. The study showed that with improved resolution, proper sample sizing, the method can be effectively used to characterize concrete damage due to expansive phases.

INVESTIGATION OF DELAYED ETTRINGITE FORMATION DAMAGE  
PROCESS USING SIMULTANEOUS NEUTRON AND X-RAY TOMOGRAPHY

by

Serge Alain Feuze Lekem

Dissertation submitted to the Faculty of the Graduate School of the  
University of Maryland, College Park, in partial fulfillment  
of the requirements for the degree of  
Doctor of Philosophy  
2019

Advisory Committee:

Professor. Amde M. Amde, Chair/Advisor

Professor Sherif M. Aggour

Professor Chung C. Fu

Professor Mohamad Al-Sheikhly

Professor Sung W. Lee

© Copyright by  
Serge Alain Feuze Lekem  
2019

## Dedication

This dissertation is dedicated:

- to my late mom Adele Nguemdjo for her endless love and dedication to her children.  
May she rest in peace,
- to my late uncle Feuza Felix and late aunt Simeu Lucienne for raising me and teaching me the value of hard work.

## Acknowledgements

Thank you to my advisor Prof. Amde M. Amde, for his support and his guidance and suggestions throughout this research.

Special thank you to Dr. Richard Livingston, Adjunct Professor in the Department of Material Science and Engineering of the University of Maryland, College Park for his guidance, advise and knowledge during the course of this research.

Thank you to Drs. Jacob LaManna, David Jacobson and Daniel Hussey of the Physical Measurement Laboratory of the NIST Center for Neutron Research, Gaithersburg, Maryland for their technical support, assistance and knowledge in the Simultaneous Neutron and X-Ray Tomography System (NeXT).

Special thank you to Stuart Sherman of the National Ready Mixed Concrete Association Laboratory, Greenbelt, Maryland for his assistance in sample preparation and testing.

Thank you to Jonathan Hummel of the FabLab of the NanoCenter at the University of Maryland College Park, Maryland for his technical support and assistance in the SEM and EDAX sample scanning.

Special thank you to my wife Larisa Kakanou, my son Nathan Feuze, my friend Charles Kamhoua and my uncle Richard Fodouop for all their encouragement, support and understanding.

# Table of Contents

Dedication.....	ii
Acknowledgements.....	iii
Table of Contents.....	iv
List of Tables.....	xi
List of Figures.....	xii
List of Abbreviations.....	xviii
Chapter 1 : General Introduction.....	1
1.1. Introduction.....	1
1.2. Background.....	3
1.3. Problem Statement.....	5
1.4. Research Approach.....	6
1.5. Objectives and Scope.....	7
1.6. Structure of Thesis.....	8
Chapter 2 : Ettringite in Concrete.....	10
2.1. Delayed Ettringite Formation in Concrete.....	10
2.1.1. Introduction.....	10
2.1.2. Definition and Mechanism of DEF.....	10
2.1.3. Mechanism of Expansion Associated with DEF.....	12
2.2. Factors Influencing DEF.....	14
2.2.1. Effect of Curing Temperature.....	14
2.2.2. Effect of Humidity During the Service Life of the Structure.....	15
2.2.3. Effect of Cement Composition.....	16
a) - The Alkaline Content of Cement.....	16
b) – The Sulfate Content of the Cement.....	17
2.2.4. The Presence of Microcracks.....	18
2.2.5. Other Parameters.....	19
Chapter 3 : Conventional Methods for Characterizing DEF.....	21
3.1. Introduction.....	21
3.2. Destructive Methods.....	21

3.2.1.	The Microscopy Method: Petrographic Analysis .....	22
3.2.2.	Scanning Electron Microscopy (SEM) .....	22
3.2.3.	X-ray Diffraction (XRD) .....	23
3.2.4.	Thermogravimetry Analysis (TGA) .....	24
3.2.5.	Limitation of Destructive Methods in the Study of Concrete Degradation Mechanism .....	25
3.3.	Non-destructive Techniques for Characterizing Distributed Damages in Concrete .....	25
3.3.1.	The Ultrasonic Pulse Velocity Method .....	27
3.3.2.	Impact Echo .....	28
3.3.3.	Non-Linear Ultrasonic Testing .....	29
3.3.4.	Radiographic Imaging Techniques .....	29
Chapter 4 : X-ray and Neutron Tomography for Characterization of Concrete Damage.		31
4.1.	Introduction .....	31
4.2.	Background on X-ray and Neutron Tomography for Characterization Of Concrete Damages.....	31
4.2.1.	Introduction.....	31
4.2.2.	Historical Background .....	32
a)	X-ray Tomography .....	32
b)	Neutron Tomography .....	34
4.3.	General Principle of Radiographic Imaging.....	36
4.3.1.	X-ray Attenuation VS Neutron Attenuation .....	37
4.3.2.	Principle of Radiography .....	40
4.3.3.	Principle of Tomography .....	40
4.4.	Dual modality Imaging: Neutron and X-ray Tomography.....	41
4.4.1.	Complementarity of X-ray and Neutron Tomography .....	41
4.4.2.	Background on the Use of Dual Modality Tomography: Neutron and X-ray	46
Chapter 5 : Sample Preparation and Materials .....		49
5.1.	Introduction .....	49
5.2.	Experimental .....	49

5.2.1.	Sample Preparation .....	50
5.2.2.	Heat Treatment.....	53
a)	Introduction .....	53
b)	Overview of Different Thermal Cycling Approaches .....	54
-	The Duggan Cycle (1986) .....	54
-	The Fu Cycle (1996).....	55
-	Other Thermal Cycles.....	57
c)	Selection of Heat Treatment to Accelerate Ettringite Formation .....	57
d)	Heat Treatment of Concrete Specimens .....	59
5.2.3.	Storage .....	60
5.3.	Material .....	60
5.3.1.	Cement .....	60
5.3.2.	Fine and Coarse Aggregates .....	62
5.3.3.	Potassium Carbonate.....	64
5.3.4.	Internal Calibration Standards: Microspheres .....	65
a)	Polystyrene Microsphere .....	65
b)	Stainless Steel Microsphere.....	66
c)	Barium Titanate Glass .....	66
5.4.	Casting and curing of Concrete Specimens.....	68
5.4.1.	The Molds .....	68
a)	For 3in. x 3in. x 11.25in. Prismatic Specimens.....	68
b)	For 4in. x 8in. Cylindrical Specimens .....	69
c)	For 2in. x 2in. Cylindrical Specimens .....	69
5.4.2.	Moist room for Concrete Curing.....	70
5.5.	Computed Tomography Specimens Mounting .....	70
5.5.1.	Stainless Steel Base Plates .....	70
5.5.2.	Epoxy Adhesive .....	71
5.5.3.	Teflon Film .....	71
Chapter 6 :	Conventional Tests Procedures .....	73
6.1.	Introduction .....	73
6.2.	Expansion Measurement .....	73

6.3.	Weight Change Measurement .....	75
6.4.	Compressive Strength .....	76
6.5.	Scanning Electron Microscopy (SEM) and Energy Dispersive X-ray Analysis (EDAX) .....	78
6.5.1.	Introduction and Background .....	78
6.5.2.	Principle of SEM – EDAX .....	78
6.5.3.	Sample Preparation for SEM and EDAX .....	79
6.5.4.	SEM and EDAX Experiment.....	80
Chapter 7 : Simultaneous Neutron and X-ray Tomography: Experimental Approach....		83
7.1-	Introduction .....	83
7.2-	Overview of the NeXT Facility at NIST .....	84
7.2.1.	The Neutron Imaging System .....	85
7.2.2.	X-Ray Imaging System.....	86
7.3-	Sample Scanning .....	88
a)	Operating Parameters .....	88
b)	Image Acquisition.....	89
Chapter 8 : Computed Tomography Image Preprocessing, Reconstruction and Post processing .....		91
8.1-	Introduction .....	91
8.2-	Image Preprocessing .....	91
8.2.1.	Image Combination.....	91
8.2.2.	Image Deconvolution.....	92
8.2.3.	Correction of Optical Distortion .....	92
8.3-	Volume Reconstruction.....	93
8.4-	Tomography Image Post-Processing.....	97
8.4.1.	Image Registration .....	97
a)	Definition.....	98
b)	Classification of Registration Methods .....	99
c)	Criteria and Selection of an Image Registration Method .....	101
d)	Intensity Based Image Registration: The Approach Based on Maximization of Mutual Information.....	102

- Different Intensity-based Approach of Image Registration .....	102
e) Image Registration by Maximization of Mutual Information .....	104
f) Approach to Image Registration Used in this Project .....	105
- Preprocessing.....	105
- Processing.....	106
8.4.2. Beam Hardening .....	108
a) Introduction and Definition .....	108
b) Overview of Common Methods of Beam Hardening Correction.....	111
c) Complexity of Beam Hardening in a Multiphase Material Like Concrete...	113
d) Neutron Beam Hardening.....	116
e) X-ray Beam Hardening.....	117
8.4.3. Overview of Image Segmentation .....	119
a) Definition.....	119
b) Classification of Image Segmentation Methods.....	119
- Region based segmentation methods.....	119
- Edge based segmentation methods .....	119
- The segmentation base on clustering.....	120
- Histogram-based methods .....	120
- Other methods.....	120
8.4.4. An Approach of Simultaneous Beam Hardening Correction and Image Fusion Segmentation .....	121
a) 2-D Histogram .....	122
b) Pixel Classification.....	124
Chapter 9 : Tests Results.....	126
9.1- Concrete Expansion Results.....	126
9.2- Weight Change Measurement .....	130
9.3- Compressive Strength Results.....	133
9.4- Scanning Electron Microscopy with Energy Dispersive X-ray Analysis .....	135
9.5.1. Heat-treated Specimens with Normal Level of Potassium. ....	136
9.5.2. Heat-Treated Specimens with High Potassium.....	141
9.5.3. Control Specimens .....	145

9.5-	Summary on Conventional Measurement and SEM .....	150
9.6-	Computed Tomography Results .....	151
9.6.1.	Single Modal Observation of Cracks Growth, Propagation .....	152
9.6.2.	Dual-Modal Observation .....	154
9.6.3.	Segmentation.....	155
Chapter 10 :	Discussion .....	159
10.1-	Introduction .....	159
10.2-	Correlations .....	159
10.2.1.	Expansion and Weight Change of Specimens.....	159
10.2.2.	Expansion and Compressive Strength.....	163
10.3-	Stage Model of Expansion .....	164
10.3.1.	Stage 1: 0 Days to 20 Days of Age: Weight Gain But no Expansion ...	164
10.3.2.	Stage 2: 20 Days to 60 Days: Weight Gain with Little Expansion .....	165
10.3.3.	Stage 3: After 60 Days: Weight Gain Leading to Significant Expansion .....	165
10.4-	Derivation of the Slope for the Late Stage Linear Relationship .....	166
10.5-	Kinetics Modeling of Concrete Deterioration .....	170
10.5.1.	The Avrami Nucleation and growth Model .....	170
10.5.2.	Curve Fitting .....	171
10.5.3.	Physical Interpretation of Parameters .....	175
a)	The Rate Constant ' $K$ ' .....	175
b)	The Asymptotic Expansion Coefficient ' $A$ ' .....	175
c)	The Dimensionality ' $n$ ' .....	176
10.6-	Discussion on the Simultaneous Neutron and X-ray Tomography.....	177
10.6.1.	The Effective Image Resolution.....	177
10.6.2.	Computational Resources Limitations .....	178
10.6.3.	Reconstruction and Registration Issues.....	179
10.6.4.	Issues with Phase Detection and Separation .....	180
Chapter 11 :	Conclusions and Future Research .....	182
11.1-	Introduction and Summary.....	182
11.2-	Conclusion of the Study .....	184

11.2.1.	Conventional Testing Methods .....	184
11.2.2.	Simultaneous Neutron and X-ray Tomography .....	186
11.3-	Recommendation for Future Research .....	187
11.3.1.	Future Research with Simultaneous Neutron and X-ray Tomography .	187
11.3.2.	Other Future Research.....	188
References	.....	189

## List of Tables

Table 4-1: Periodic Table with X-ray Attenuation Coefficient of Elements for 125 KeV Energy (Grunauer 2005 Cited by De Beer et al. 2005 .....	43
Table 4-2: Periodic Table with Thermal Neutron Energy Attenuation Coefficient of Elements (grunauer 2005 Cited by De Beer 2015).....	43
Table 4-3: Neutron Attenuation Coefficient of Common Phases Found in Concrete .....	45
Table 5-1: Distribution of Microsphere Calibration Standards in 2in. x 2in. Concrete Cylinders.....	51
Table 5-2: Concrete Mix Design for 1 Cubic Yard .....	52
Table 5-3: Test Matrix for the Experiment.....	52
Table 5-4: Composition of Type III Portland Cement from XRF Spectroscopy.....	61
Table 5-5: Technical Information of Fine Aggregates .....	62
Table 5-6: Technical Information of Coarse Aggregates .....	63
Table 5-7: Mass Element Composition of Coarse Aggregates from Prompt Gamma Activation Analysis.....	64
Table 5-8: Attenuation Factors for Phases Found in Concrete for 25 meV Versus 45 keV X-ray Photons.....	66
Table 6-1: Tests Frequencies .....	73
Table 7-1: NeXT Operating Parameters .....	89
Table 8-1: Characteristics of Tomographic Stacks of slices.....	97
Table 8-2: Summary of Number of Slices from Reconstruction of Raw Data.....	97
Table 9-1: Average Compressive Strength of Concrete Specimens.....	134
Table 9-2: Summary of SEM/EDAX Results Showing Morphology of Ettringite and Other Phases Found in Voids of Specimens at Various Age.....	151
Table 10-1: Linear Equation for Expansion of Heat-Treated Concrete Specimens .....	163
Table 10-3: Fit Parameters of the KAJM Model for Concrete Specimens Expansion...	174

## List of Figures

Figure 1-1: Garboczi Single Spherical Aggregate Model.....	3
Figure 1-2: Characteristic Damage Feature .....	3
Figure 2-1: Expansion of Cement Mortars with Different Aggregate Types (Grattan-Bellew (Grattan-Bellew <i>et al.</i> , 1998)).....	19
Figure 3-1: Principle of X-Ray Diffractometer .....	23
Figure 3-2: Equipment Used in a Typical Ultrasonic Pulse Velocity (Genoves <i>et al.</i> , 2017). .....	28
Figure 3-3: Schematic of impact Echo Method (Zhang <i>et al.</i> , 2016).....	28
Figure 4-1: Interaction of Matter with X-Ray and Neutron (Strobl et al. 2009 cited by Kim (Kim, 2013)) .....	41
Figure 4-2: Comparison of 45 KeV X-ray and 25 meV thermal neutron Mass Attenuation Coefficients as a Function of Atomic Number, Where the neutron Cross Section Assumes Natural Isotropic Abundances. (Source: LaManna (Lamanna <i>et al.</i> , 2017)).....	42
.....	43
Figure 5-1: Approximate Location of Calibration Standard in a 2in. x 2in. Concrete Cylinders.....	51
Figure 5-2: Duggan Heat Cycle for Mortar and Concrete Samples.....	55
Figure 5-3: Fu Method to Assess DEF (Thomas, Personal Communication, 2000 after Fu 1996).....	56
The Kelham Cycle (1995).....	56
Figure 5-4: Kelham Method to Assess DEF (Thomas, Personal Communication, 2000 after Fu 1996).....	57
Figure 5-5: Specimens in Oven During Duggan Heat Treatment.....	59
Figure 5-6: Sample Storage in Saturated Limewater .....	60
Figure 5-7: Plot of Computed Attenuation Factor for Phases Found in Concrete for 25 meV versus 45 keV X-ray Photons.....	67
Figure 5-8: Placement of Polystyrene Microsphere (yellow arrows) During Casting.....	68
Figure 5-9: Polystyrene Microsphere Visible (yellow Arrow) in Neutron CT Slice.....	68
Figure 5-10: Overview of 2in. x 2in. Cylinder Molds .....	69

Figure 5-11: Steel Prism Molds and 4in. x 8in. PVC Cylinder Molds .....	69
Figure 5-12: Steel Gage Studs in Steel Prism Mold and 10in. Rod Spacer .....	70
Figure 5-13: 2in. x 2in. Concrete Cylinder on Steel Base Plate .....	72
Figure 5-14: 2in. x 2in. Concrete Cylinder Wrapped in Teflon Film Ready for Scanning .....	72
Figure 5-15: Location of Notches on Steel Base Plates.....	72
Figure 6-1: Comparator Set Up for Expansion Measurement .....	74
Figure 6-2: Concrete Specimen Positioned for Weight Measurement on a Digital Scale	76
Figure 6-3: Compressive Test Machine Used.....	77
Figure 6-4: Compression Testing of a Concrete Cylinder .....	77
Figure 6-5: SEM and EDAX Sample Preparation: (a) Drying, (b) Mounting of Sample Holder, (c) Carbon Coating.....	82
Figure 6-6: Hitachi S-3400 Variable Pressure SEM Scanner .....	82
Figure 7-1: Flowchart of Different Steps for Simultaneous Neutron and X-ray Imaging	84
Figure 7-2: Perspective View of the Thermal Neutron Facility at NIST in Gaithersburg	86
Figure 7-3: Plan View of the Thermal Neutron Facility of NIST in Gaithersburg.....	86
Figure 7-4: Engineering Model Representation of the NeXT System at NIST with the Neutron Beam in Red and the X-ray Beam in Blue (Source: LaManna (Lamanna <i>et al.</i> , 2017) ).....	87
Figure 8-1: X-ray Radiograph of a Concrete Specimen .....	93
Figure 8-2: Neutron Radiograph of a Concrete Specimen.....	93
Figure 8-3: Example Neutron Dark-Field Image.....	94
Figure 8-4: Example Neutron Flat-Field Image.....	94
Figure 8-5: Neutron Sinogram for DP1-2-6.....	95
Figure 8-6: X-ray Sinogram for DP1-2-6 .....	95
Figure 8-7: Quasi- Parallel Beam Configuration for Neutron Imaging.....	96
Figure 8-8: Cone Beam Configuration for X-ray Imaging.....	96
Figure 8-9: Bimodal registration a) Source: Neutron image, b) target X-ray image, c) registered X-ray image.....	107
Figure 8-10: Time series Neutron Image Registration a) Source: Scan DP1-2-5, b) target: Image Scan DP1-2-6, c) Registered Image of Scan DP1-2-6.....	108

Figure 8-11: Position of a profile line across a neutron CT slice and grayscale values of the profile showing the cupped pattern due to beam hardening .....	110
Figure 8-12: Position of a Profile Line Across an X-ray CT Slice and Grayscale Values of the Profile Showing the Cupped Pattern Due to Beam Hardening .....	110
Figure 8-13: X-ray Slice of the Steel Base Plate Showing Streak Artifacts Radiating from the Notches (a) and Slice of the Concrete Cylinder Showing Streak Radiating from the Steel Beads (b) .....	111
Figure 8-14: Neutron Slice Partitioned Into 50 Pixels Wide Rings.....	114
Figure 8-15: Grayscale Histogram for Individual Rings Of A Neutron CT Slice. Ring Width=50 Pixels; Outermost Ring Includes Air -Filled Pores .....	115
Figure 8-16: Plot of the Aggregate Peak Intensity of Individual Rings. The Variation is Shown for a Slice Taken at the Upper (Top), Middle (Center) and Lower (Bot) Sections of the Specimen.....	115
Figure 8-17: Plot of X-Ray Attenuation Factors VS Photon Energy.....	118
Figure 8-18: Synopsis of Image Segmentation Methods .....	120
Figure 8-19: Example 1D Histograms of Pixel Intensity of Neutron (a) and X-ray (b) volumes .....	123
Figure 8-20: 2D Binary Histogram of Pixel Intensity Summed over a Neutron and the Corresponding X-ray Volume.....	124
Figure 8-21: 2D Binary Histogram of Pixel Intensities over a Volume with .....	125
Figure 8-22: Registered and Fused X-ray and Neutron CT Slice.....	125
Figure 9-1: Plot of Expansion of Concrete Specimens .....	128
Figure 9-2: Rate of Expansion of Heat-Treated Specimens with Normal Potassium.....	128
Figure 9-3: Rate of Expansion of Heat-Treated Specimens with High Potassium.....	129
Figure 9-4: Rate of Expansion of Control Specimens .....	129
Figure 9-5: Appearance of Hairline Crack at the Surface of Heat-Treated Concrete Specimen with High Potassium at Age 357 days .....	130
Figure 9-6: Plot of Weight Change VS Age of Concrete Specimens .....	131
Figure 9-7: Rate of Weight Change for Heat-Treated Specimens with Normal Potassium .....	132
Figure 9-8: Rate of Weight change of Heat-Treated Specimens with High Potassium..	132

Figure 9-9: Rate of Weight Change for Control Specimens.....	133
Figure 9-10: Plot of Compressive Strength of Concrete Specimens .....	134
Figure 9-11: Typical Output of EDAX of Ettringite with the Characteristic Step Model of Al, S and Ca (Source: Ceary, 2007).....	136
Figure 9-12: SEM Image and EDAX Plot of Heat-Treated Specimens with Normal Level of Potassium at 40 days, Showing Sphere-Shape Ettringite Particles Layering the Interior of an Air Void at The Aggregate/Paste Interface.....	137
Figure 9-13: SEM and EDAX of Heat-Treated Specimens with Normal Potassium at 83 days Showing Clusters of Needle-Like Ettringite Particles in a Void at the Aggregate /Paste Interface.....	138
Figure 9-14: SEM and EDAX of Heat-Treated Specimens with Normal Level of Potassium at 120 Days Showing Needle-Like Ettringite Particles and Calcium Carbonate Balls in a Void at The Aggregate/Paste Interface.....	139
Figure 9-15: SEM and EDAX of Heat-Treated Specimen with Normal Potassium at 337 Days Showing ettringite Needles and Carbonate Calcium Balls.....	140
Figure 9-16: Ternary Plot of Al-Ca-S for Particles in Void at the Aggregate/Paste Interface of Heat-Treated Specimens with Normal Potassium.....	141
Figure 9-17: SEM and EDAX of Heat-Treated Specimen with High Potassium at 40 Days showing Clusters of Ettringite lamellae in a void at the Aggregate/Paste Interface.....	142
Figure 9-18: SEM and EDAX of Heat-Treated Specimens with High Potassium at 83 days Showing Sphere-Shape clusters of Ettringite Needle in void at the Aggregate/Paste Interface. A Microcrack is Also Visible. ....	143
Figure 9-19: SEM and EDAX of a Heat-Treated Specimen with High Potassium at 120 Days showing needle-like Ettringite crystals in a Void at the Aggregate/Paste interface .....	143
Figure 9-20: SEM and EDAX of Heat-treated Specimens with High Potassium at 337 Days Showing Dense needle Crystal of Ettringite and Plate Shape Crystals of Monosulfate in Void at the Aggregate/Paste Interface .....	144
Figure 9-21: Ternary Plot of Al-Ca-S for Particles in Void at the Aggregate/Paste Interface of Heat-Treated Specimens with High Potassium.....	145

Figure 9-22: SEM and EDAX of Control Specimens at 40 Days showing grain Particles of Calcium Hydroxide in Void at the Aggregate/Paste Interface .....	146
Figure 9-23: SEM-EDAX of Control Specimen at age 83 Days Showing Spars Crystals of Calcium Carbonate in Void at the Aggregate/Paste interface .....	147
Figure 9-24: SEM-EDAX of Control Specimen at 120 days Displaying Thin Needle-like Ettringite Crystals and Calcium Carbonate Particles in Voids at the Aggregate/Paste Interface .....	148
Figure 9-25: SEM-EDAX of Control Specimens at 337 Days Showing Needle Like Ettringite Crystals and Blobs Crystals of Calcium Carbonate in Voids at the Aggregate/Paste Interface .....	149
Figure 9-26: Ternary plot of Al-Ca-S for Particles in Void at the Aggregate/Paste Interface of Control Specimens .....	150
Figure 9-27: X-ray slice of heat-treated specimen with normal potassium at age 102 days (a) and at age 230 days. Red arrows show initial cracks, yellow arrows indicate existing cracks growth and blue arrows indicate new cracks. ....	152
Figure 9-28: X-ray slice of heat-treated specimen with high potassium at age 102 days (a) and at age 230 days. Red arrows show initial cracks, yellow arrows indicate new cracks. ....	153
Figure 9-29: X-Ray Slice of Control Specimen at Age 102 Days (A) and at Age 230 Days. Red Arrows Show Late Stage Crack Appearance. ....	153
Figure 9-30: X-ray (a) and Corresponding Neutron Slice (b) of Heat-Treated Specimens at Age 230 Days. Arrow in Red Indicate Cracks on X-ray slices that Appear Bright in Neutron Slice (Yellow Arrows) Meaning Water or Ettringite Filling. ....	155
Figure 9-31: Segmented fused CT Slice for Heat-treated Specimen with Normal Potassium at Age 102 Days (a) and 230 Days (b). The Blue Arrow Indicates Pores Ettringite Filing (yellow) .....	156
Figure 9-32: Segmented fused CT Slice for Heat-treated Specimen with High potassium at age 102 Days (a) and 230 Days (b). The Blue Arrow Indicates Pore Ettringite Filling (yellow) .....	156
Figure 9-33: 3D Rendering and Section through a Heat-treated Specimen with High Potassium at age 230 Days. The Blue Arrow Indicates Potential Ettringite in Pores ....	157

Figure 9-34: 3D Rendering of Paste Stack of Slices for a Heat-treated Specimen with High Potassium at Age 230 Days .....	157
Figure 9-35: 3D rendering of stack of slices from heat-treated specimen with high potassium at age 230 days.....	158
Figure 9-36: 3D Rendering of Suspected Ettringite Stack of Slices from Heat-treated Specimen with High Potassium at age 230 Days.....	158
Figure 10-1: Plot of Weight Change VS Expansion of Concrete Specimens.....	160
Figure 10-2: Early Age Expansion VS Weight Change of Concrete Specimens .....	161
Figure 10-3: Fitting Curve of Late Age Weight change VS Expansion of Heat-treated Specimens. ....	162
Figure 10-4: Plot of Expansion VS Weight Change of Heat-Treated Specimens with Normal Potassium Lag-Adjusted and With High Potassium Non- Adjusted .....	162
Figure 10-5: Plot of Expansion VS Compressive Strength of Heat-Treated Concrete Specimens .....	163
Figure 10-6: Plot of Expansion of Concrete Specimens Showing Three Stages Model	164
Figure 10-7: KAJM Fitting Curve of Expansion Data for Heat-Treated Specimens with Normal Potassium.....	173
Figure 10-8: KAJM Fitting Curve of Expansion Data for Heat- Treated Specimens with High Potassium .....	173
Figure 10-9: KAJM Fitting Curve of Expansion Data for Control Specimens .....	174
Figure 10-10: 2D Histogram of Pixel Intensities for X-ray and Neutron Volumes with Polygons Drawn for Segmentation .....	181

## List of Abbreviations

- AASHTO: American Association of State Highway Transportation Officials
- ACI: American Concrete Institute
- ACR: Alkali -Carbonate Reaction
- ASR: Alkali-Silica Reaction
- ASTM: American Society for Testing and Materials
- CDLE: Capacitive Double-Layer Expansion
- CSH: Calcium Silicate Hydrate
- CT: Computed Tomography
- DEF: Delayed Ettringite Formation
- EDS: Energy Dispersive Spectroscopy
- EEF: Early Ettringite Formation
- F-T: Freeze Thaw
- GB: Giga Bytes
- GIF: Graphics Interchange Format
- ITZ: Interfacial Transition Zone
- JPEG: Joint Photographic Experts Group format
- KAJM: Kolmogorov-Avrami-Johnson-Miehl model
- MDOT-SHA: Maryland Department of Transportation - State Highway Administration
- MI: Mutual Information
- NCNR: NIST Center for Neutron Research
- NDT: Non-Destructive Testing
- NeXT: Simultaneous Neutron and X-ray Tomography System

NIF: Neutron Imaging Facility at NIST

NIST: National Institute of Standard and Technology

NRMCA: National Ready-Mix Concrete Association

PGAA: Prompt Gamma Activation Analysis

PH: Power of Hydrogen

PNG: Portable Network Graphics format

PTFE: Polytetrafluorethylene (Teflon<sup>®</sup>)

R.H.: Relative Humidity

RAM: Random Access Memory

SEM-EDAX: Scanning Electron Microscopy with Energy Dispersive X-ray Analysis or

Energy Dispersive Analyzer X-ray

SSD: Sum of Square Difference

TGA: Thermogravimetric Analysis

TIFF: Tagged Image File Format

UMD: University of Maryland, College Park

XRD: X-ray Diffraction

XRF: X-ray Fluorescence

# Chapter 1 : General Introduction

## *1.1. Introduction*

Concrete durability has always been a concern and one of the main problems in the construction industry. Premature concrete deterioration requires costly maintenance, rehabilitations and repairs of buildings and infrastructures. For example, the American Association of State Highway Transportation Officials (AASHTO) estimated in 2008 that 40% of the more than 575,000 bridges on primary and secondary road in the US would require repairs, protection and strengthening to solve problems among which premature deterioration of material (Nawy, 2008). As a specific example, in the state of Maryland, for the fiscal years 2016, on the 1.27 billion of the capital project funds spent, 445 millions of dollars was spent on the maintenance of existing structures. Almost 1/3 of this amount (151 millions) was spent in the maintenance and rehabilitation of concrete structures including bridges (MDOT-SHA). The main causes of this premature deterioration have been identified as alkali silica reaction (ASR), freeze-thaw (F-T) and potentially delayed ettringite formation (DEF) (Ceary, 2003; Amde *et al.*, 2005). A study done by the Texas department of Transportation in 2009 in the Houston District found that damages caused by these three agents could be estimated at up to \$ 1 billion (Deschenes, 2009). It is therefore important to produce concrete that is more durable especially in aggressive environments. Even though ASR, DEF and FT are all expansive phases, they have different expansion mechanisms. Identifying and understanding the mechanism by which each of this phenomenon damages concrete is of paramount importance in finding a cure and mitigating their effect.

DEF arose as a problem in heat cured concrete in 1980's through the works of Ghorab (Ghorab *et al.*, 1980) and then Heinz and Ludwig (Heinz e Ludwig, 1987) who observed significant DEF induced expansion in concrete leading to cracking and deterioration. The most notable cases of concrete deterioration due to ettringite were observed on railroad precast concrete ties in the US and in Canada. Initially thought to be a problem only in precast heat cured concrete, it has been found to be a worldwide problem that affects also cast-in-place concrete structures. There have been numerous studies over the years aimed at understanding the causes, the physico-chemical mechanism and the kinetics of reactions leading to expansion due to delayed ettringite formation and identify the parameters leading to those reactions. Despite those numerous studies, there is still a lot of controversies and unknowns surrounding DEF. For example there is still no consensus on whether DEF is the cause of microcracking or just an opportunistic phenomenon that takes place in existing cracks, some researchers have even suggested that there is no direct correlation established between the amount of ettringite detected and expansion of the heat-cured mortars (Famy *et al.*, 2001). Garboczi proposes a general theoretical model of stress distributions in a heterogeneous material like concrete, which assumes a single spherical aggregate particle embedded in a matrix, with an interfacial zone or rim surrounding it (Garboczi, 1997)(Figure 1-1). The rim, also called interfacial transition zone (ITZ) or simply aggregate/paste interface is a region close enough to the nearest aggregate to be affected by its presence (Diamond, 2007). Three cases are considered: uniform expansion of the matrix, expansion of the rim only and expansion of the aggregate only. Those models have been extensively studied (Scherer, 1999; Yan *et al.*, 2001; Famy *et al.*, 2002), but there is an ongoing debate as to which one is the leading cause of concrete expansion due

to DEF from these cases. The objective of this study is to shed some light on the debate by emphasizing how expansion of the matrix is the leading mechanism behind concrete expansion due to internal sulfate attack. To investigate the correlation between expansion and microscale damage caused by DEF, a nondestructive simultaneous neutron and X-ray tomography method is investigated.

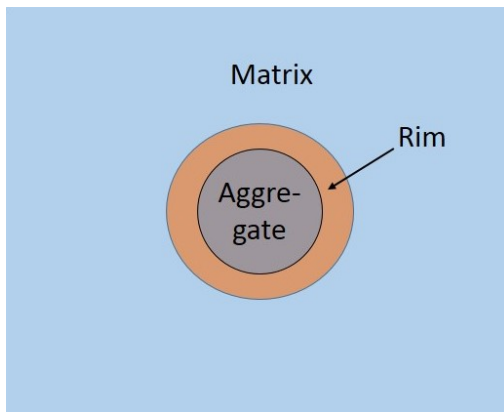


Figure 1-1: Garboczi Single Spherical Aggregate Model

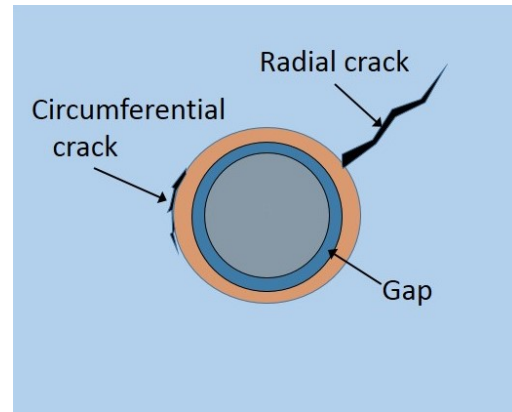


Figure 1-2: Characteristic Damage Feature

### 1.2. Background

Delayed ettringite formation (DEF) is a concrete pathology due to the formation of a hydrate, ettringite, ( $[\text{Ca}_6\text{Al}_2(\text{SO}_4)_3(\text{OH})_{12} \cdot 26\text{H}_2\text{O}]$ ) into hardened concrete. Ettringite is an expansive material naturally present into cementitious material at early stages as a product of cement hydration. It is formed within the first few hours after cement is mixed with water when gypsum ( $\text{CaSO}_4 \cdot 2\text{H}_2\text{O}$ ) reacts with tricalcium aluminate ( $\text{C}_3\text{A}$ ) (Scrivener e Pratt, 1984). This process is termed as Early Ettringite Formation (EEF) and the ettringite thus formed is called primary ettringite. It does not cause any significant localized disruptive action even though it has a higher volume than its reactants. As concrete is still in the plastic stage, this expansion is harmless and often un-noticed. At this

stage, ettringite is uniformly and discretely dispersed throughout the cement paste at a sub-microscopic level.

At high curing temperatures 65°C- 70°C, the primary ettringite formed will be decomposed, and the sulfate and alumina held in the C-S-H gel of the cement paste or partially converted to monosulfate (AFm) and sulfate ions. As the temperature of concrete falls below 70°C, the ettringite subsequently re-forms causing expansion in the concrete that has already been hardened. This process is called Delayed Ettringite Formation (DEF) and the ettringite thus formed is called secondary ettringite. This secondary ettringite can lead to expansion of concrete and subsequently to microcracks into concrete. Concrete damage occurs only when a threshold amount of ettringite is formed (Clifton e Pommersheim, 1994). There are been numerous studies to understand the mechanism by which DEF induces damage in concrete.

One of the earliest studies on DEF induced expansion was the work of Mehta (Mehta, 1973). Long before it was seen as a problem, secondary ettringite had been found in many concrete structures without receiving specific attention. In 1965, Kennerly found ettringite in deteriorated areas of cold joint of the Roxburgh Dam, Otago, New Zealand. It was concluded that ettringite was formed as a result of the variation of calcium hydroxide (CH) concentration. In 1980, Pettifer and Nixon observed ettringite in the pores, voids and around aggregates in concrete bases in English Midlands, Western England and South Wales In this case ettringite was found in conjunction with alkali silica gel. Pettifer and Nixon also found ettringite in the Pirow Street Bridge in Cape Town, South Africa just four (4) years after placement (1980). Acknowledgement of the expansive nature of ettringite in concrete started in 1970 with the report of the ACI Committee 223 on Expansive Cement

Concrete (1970). Mehta (Mehta, 1973) was one of the first researchers to hypothesize on the mechanisms of expansion of concrete due to delayed ettringite formation.

### *1.3. Problem Statement*

Delayed ettringite formation is a form of internal sulfate attack. It produces distributed damage in concrete in the form of micro-cracking which result in loss of strength and stiffness and affects the durability of concrete by changing the chemical and microstructure of the cement paste. The mechanism by which this occurs is still not well understood despite the numerous studies carried out over the years. Most of the studies so far have been conducted at the macroscopic level through tests like expansion and weight change measurement, compressive strength testing which does not allow for understanding of the mechanisms occurring at the microscopic level. In additions the few studies done at the microscopic level were mostly through destructive testing methods. At the microscopic level, conventional analytical methods used to study ettringite in concrete include X-ray diffraction, thermal analysis, and scanning electron microscopy. These methods have the disadvantage that they use small sample which are not necessarily representative of the overall concrete volume. In addition, there is loss of spatial information as they focus on small areas and do not allow for visualization of the overall concrete volume. Most and foremost, these methods are all destructive and do not allow for monitoring of the development of damage in concrete. This study hereby explores the use of a novel method combining neutron and X-ray tomography which have the advantage of being nondestructive and allows for visualization of the whole sample volume. In addition, simultaneous neutron and X-ray tomography can provide quantitative information on the damage progress at the microscale nondestructively.

#### *1.4. Research Approach*

Delayed ettringite formation has been identified as one of the primary causes of premature deteriorations of concrete structure along with alkali silica reaction and freeze-thaw. The relationship between ettringite formation, expansion, and damage in DEF-affected cement-based materials is not well understood. Some models based on thermodynamic considerations have been developed to explain the different reactions leading to DEF (Flatt e Scherer, 2008; Grimal, Sellier, Yann, *et al.*, 2008; Salgues *et al.*, 2014) however they are highly nonlinear, as several coupled equations have to be solved simultaneously (Sellier e Multon, 2018). Chemical and thermochemical models have been proposed (Sellier e Multon, 2018). From a mechanical point of view, efficient nonlinear models exist to analyze structural behavior affected by swelling problems in general (Karthik *et al.*, 2016) (Grimal, Sellier, Le Pape, *et al.*, 2008; Comi *et al.*, 2009; Seignol *et al.*, 2009) but they are not yet able to consider all the chemical particularities of DEF. There have also been some Finite element (FE) modeling (Roubin *et al.*, 2014) performed to better understand the degradation of cement-based materials during DEF development. Despite those attempts to better understand DEF induce degradation of concrete structures, no general relationship between the increase in the ettringite content, DEF-related expansion, and damage has been developed (Taylor *et al.*, 2001).

The current research project has been conducted in three phases. In the first phase, concrete specimens were made, cured in a moist room with R.H. at 97% and stored in limewater. Some of the specimens were made with additional potassium carbonate in order to increase the level of potassium in their mix. Storage in limewater was chosen as previous research

conducted at the University of Maryland (Ceesay, 2007; Amde *et al.*, 2014) have shown that it inhibits the growth of delayed ettringite. Among those specimens, some were subjected to a heat treatment in order to initiate microcracks. The heat cycle was carried out 24 hours after casting the specimens. It took fifteen (15) days from casting to storage of the specimens in limewater. Phase 2 and 3 were conducted concomitantly. In phase 2, the specimens made for expansion measurement (3in. x 3in. x 11.25in. specimens) were measured at regular time interval for length and weight change. In this same phase, specimens made for strength measurement were tested for compressive strength. Samples were taken from these specimens and tested by Scanning Electron Microscopy with Energy Dispersive X-Ray Spectroscopy (SEM-EDAX) in order to identify the presence and location of ettringite. In phase 3, the 2in. by 2in. cylinders were scanned at the NIST Center for Neutron Research with the simultaneous neutron and X-ray tomography system (NeXT) at regular intervals. The raw images collected were processed and 3D images of the specimens reconstructed, which shows the interior of the specimens. Analysis of these images would allow for characterization of DEF induced degradation process in concrete.

### *1.5. Objectives and Scope*

1. Perform a literature review to identify parameters and damage mechanisms associated with DEF in concrete.
2. Perform a literature review of conventional destructive and nondestructive methods of characterizing DEF induced damage in concrete at macroscopic and microscopic scale.
3. Prepare concrete specimens based on proven techniques for initiating distributed damage. These techniques will be based around the selection of materials and

additives, the curing method of the concrete and processes to accelerate distributed damage; namely the UMD Modified Duggan Cycle.

4. Apply conventional macroscopic and microscopic testing methods to monitor the process and progress of damage in the concrete specimens. These tests include length change, weight change, and compressive strength and SEM-EDAX images.
5. Analyze data from macroscopic testing methods to make correlation analysis and study the kinetics of concrete deterioration due to DEF.
6. Perform simultaneous Neutron and X-ray tomography of concrete specimens in order to gather data on specimen condition over time and explore the feasibility of the method to characterize DEF induced damages in concrete.
7. Use advanced computer methods to process and reconstruct tomography data and in order to perform qualitative analysis

### *1.6. Structure of Thesis*

This thesis consists of eleven (11) chapters. The first chapter gives a brief introduction to the subject of the research, provides the background, states the problem, and gives the main objectives and the research significance. Chapter 2 defines ettringite, gives an overview of the conditions required for development of late ettringite in concrete and discusses the mechanisms of expansion associated with DEF. In Chapter 3, we present a comprehensive review of destructive and non-destructive techniques used to characterize DEF induced damage in concrete and a background on the use of neutron and x-ray tomography in concrete research and an overview of the tomography image processing. Chapter 4 provides the background and the general principle of neutron and X-ray tomography. In Chapter 5 and 6 we outline the sample preparation method, the curing and heat cycle used

to inhibit DEF in concrete. A brief description of conventional tests used to monitor concrete specimens in this study is also provided. In chapter 7, we present the experimental approach used for the simultaneous neutron and X-ray tomography while chapter 8 describes the data processing and reconstruction of tomography images. The results of tests are provided and analyzed in Chapter 9 and discussed in Chapter 10. Chapter 11 summarizes and provides conclusions for the research and opens venues for future research work.

## Chapter 2 : Ettringite in Concrete

### 2.1. Delayed Ettringite Formation in Concrete

#### 2.1.1. Introduction

Concrete is typically a durable material. However, its durability can be affected by material –related distress among which the most common are corrosion, alkali silica reaction (ASR), sulfate attacks, alkali-carbon reaction (ACR) and freeze /thaw cycle (FT). Of the sulfate attacks, the most common form is delayed ettringite formation (DEF) is a form of sulfate attack and occurs when ettringite forms with no external source of sulfate (Taylor *et al.*, 2001).

#### 2.1.2. Definition and Mechanism of DEF

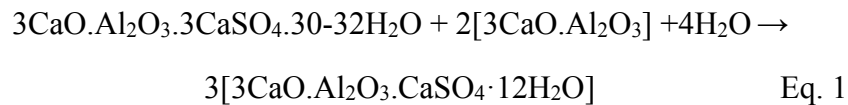
Ettringite or tri-sulphoaluminate of calcium  $3\text{CaO} \cdot \text{Al}_2\text{O}_3 \cdot 3(\text{CaSO}_4) \cdot 30-32\text{H}_2\text{O}$  is a crystal rare in nature, but in civil engineering in general and cement chemistry in particular, it represents one of the most important products of cement hydration. It forms in concrete both moments after mixture of the concrete components with water, and later in the life of the hardened concrete (months or years later).

The main components of Portland cement that are involved in the hydration process are clinker and gypsum. Clinker is a compound of tri-calcium silicate, di-calcium silicate, tri-calcium aluminate, alumino ferrites and other components present in small amount. The table below shows notations adopted in cement chemistry:

Table 2-1: Cement Chemistry Notation

Notation	C	S	H	$\bar{S}$	F	A
Chemical Formula	CaO	SiO <sub>2</sub>	H <sub>2</sub> O	SO <sub>3</sub>	Fe <sub>2</sub> O <sub>3</sub>	Al <sub>2</sub> O <sub>3</sub>

Portland cement typically has the following composition by weight: 60% of tri-calcium silicate (C<sub>3</sub>S), 15% of di-calcium silicate (C<sub>2</sub>S), 8% of tri-calcium aluminate (C<sub>3</sub>A) and 10% of alumino ferrites (C<sub>4</sub>AF). The amount of gypsum added is usually between 4 and 5%. Other components present in small quantities include sulfate, manganese dioxide, magnesium oxide and alkali (K<sub>2</sub>O, Na<sub>2</sub>O). Gypsum (CaSO<sub>4</sub>.2H<sub>2</sub>O) is of great importance in the hydration process of cement. Without gypsum, the cement paste would immediately harden when concrete is mixed due to the rapid hydration of the aluminates (C<sub>3</sub>A), not allowing the formation of the concrete matrix. The addition of gypsum retards the rapid hydration of C<sub>3</sub>A and controls the rate of hardening. The retardation occurs because when gypsum reacts with aluminates C<sub>3</sub>A it produces ettringite (3CaO.Al<sub>2</sub>O<sub>3</sub>.3(CaSO<sub>4</sub>).30-32H<sub>2</sub>O) which then forms a coating around the other C<sub>3</sub>A particles, permitting enough time for the hydration of silicates C<sub>3</sub>S (Collepardi *et al.*, 1987) and permits the natural setting to occur. The reaction of gypsum and C<sub>3</sub>A continues until gypsum is exhausted. The formation of ettringite during the setting process is called Primary Ettringite Formation and does not cause damage to concrete. It is often accepted that this primary ettringite is thermodynamically unstable and breaks down after a few hours into monosulfate Ca<sub>4</sub>Al<sub>2</sub>O<sub>6</sub>(SO<sub>4</sub>).14H<sub>2</sub>O (Christensen *et al.*, 2004). This is done by reacting with the remaining aluminate C<sub>3</sub>A.



For concretes cured at temperatures above 70°C the sulfate release by decomposition of primary ettringite does not react completely with aluminates (C<sub>3</sub>A) and therefore they become available to the pore solution (Yang *et al.*, 1996). These available sulfates are

trapped by physical adsorption on the surfaces of the calcium silicate hydrate (C-S-H gel) (Fu, 1996) whose hydration has been accelerated as a result of heat curing (Divet e Randriambolona, 1998). When the material is subsequently stored at ambient temperature and moisture, the C-S-H gel releases the trapped sulfates which then diffuse into the nearest microcracks to the pores where they react with the pore solution and monosulfate to form ettringite (Scrivener *et al.*, 1999; Taylor *et al.*, 2001). Ettringite which forms at this stage of the structure's life when concrete has already hardened is called Delayed Ettringite formation (DEF or Secondary or Late Ettringite Formation).

### 2.1.3. Mechanism of Expansion Associated with DEF

Despite the numerous studies consecrated to ettringite, there is still no agreement on the mechanism by which DEF expands and damages concrete. Various theories have been developed to this regard. Cohen (cited by Day (Day, 1992)) initially summarized those into two main theories: the crystal growth theory and the swelling theory. Later, other theories were hypothesized like the uniform paste Theory and the Electric (Capacity) Double Layer Expansion Theory.

#### *The topochemical Reaction with Directional Growth or Crystal growth Theory*

This theory stipulates that expansion is caused by the formation of ettringite crystals at the surface of Aluminum-bearing particles and in the solution. The growth of these crystals causes expansion through generation of crystallization pressure in regions of limited space like crack tips (Fu, 1996). A better understanding of this theory can be obtained through Scherer's discussion on the physical chemistry of crystal growth in porous material (Scherer, 1999). Scherer suggested that the highest expansive pressures will be exerted at

locations where the supersaturation is high and the crystals are formed in relatively isolated regions like small poorly connected pores containing ionic species and specially of  $\text{Al}(\text{OH})_4^-$  (Taylor *et al.*, 2001).

#### *The swelling Theory of Expansion*

Also called Theory of water absorption of colloidal ettringite, this theory suggested by Mehta in 1973 (Mehta, 1973) is the oldest even though it did not get a lot of attention in the literature compare to other theories. Mehta hypothesized that in presence of portlandite ( $\text{Ca}(\text{OH})_2$ ), ettringite is formed as colloidal, hydrophilic and expansive particles. These gel-like particles have a large specific surface area analogous to C-S-H gel and absorb water, resulting in overall expansion. Several works have tried to corroborate this hypothesis including the research of Yan (Yan *et al.*, 2001).

#### *The Uniform Paste Theory*

This theory was proposed by Taylor (Taylor *et al.*, 2001) and adopted by many authors (Scrivener *et al.*, 1999). The theory suggest that in a concrete cured at high temperature, microcrystalline ettringite will form initially in cement paste, leading to uniform and isotropic expansion of the paste. This expansion of the material produces microcracks both in the paste and at the aggregate interfaces. Ettringite would then later recrystallize in these cracks without generating any significant additional expansive pressures.

#### *Other theory: The theory of the Electric (Capacitive) Double-layer Expansion (CDLE)*

The theory of the electric or capacitive double-layer expansion is one of the lesser known. It is derived from the swelling theory due to the fact that it relies on colloidal ettringite

particles. It is based on the principle of repulsive forces due to the electrical double-layer proposed by Li (Li *et al.*, 1996). According to this theory, negatively charged colloidal ettringite particles attract and fix alkaline ions ( $\text{Na}^+$ ,  $\text{K}^+$ ) present in the pore solution. Due to the leaching of the material, alkaline ions will subsequently diffuse outwards and the concentration inside the colloidal ettringite will significantly decrease. Due to this decrease, electrostatic repulsion forces will increase and become higher than the Van der Waals forces and thus, the distance between ettringite particles will increase, leading to expansion. This theory however did not gain a lot of traction within the scientific community.

## 2.2. Factors Influencing DEF

The numerous studies have shown with evidence that there are two conditions required but not sufficient for delayed ettringite formation to occur:

- Curing at high temperature beyond 70°C
- The presence of humidity during the service life of the structure.

Beyond these two parameters, many others play an important role in late ettringite formation.

### 2.2.1. Effect of Curing Temperature

Numerous studies have shown the importance of curing temperature in delayed ettringite formation. Heinz (Heinz e Ludwig, 1986; 1987; Heinz *et al.*, 1989), Lewis (Lewis, 1996), Ghorab (Ghorab *et al.*, 1980), and Ludwig (Ludwig, 1991) all demonstrated that high temperature curing above 70°C was essential for DEF induced expansion to occur. Lawrence (Lawrence, 1995) found that the critical curing temperature for DEF is between

65 and 70°C. Heinz (Heinz e Ludwig, 1987) and later Odler (Odler *et al.*, 1987; Odler e Chen, 1996) found that at temperature above 70°C, primary ettringite is broken down into monosulfate. Later, when the concrete is exposed to moisture at normal temperatures, the monosulfate is reconverted to ettringite in the hardened concrete where it induced expansion (Yang *et al.*, 1999; Famy *et al.*, 2001; Pavoine *et al.*, 2003). However, some recent researches have contested those findings as delayed ettringite formation has been found to have caused damages to structures cured at temperature below the critical temperature of DEF. Sahu et al. (Sahu e Thaulow, 2004) observed microcracks on railroad ties that have been cured at temperatures below 60°C. They concluded that DEF might occur at temperatures below 70°C when certain conditions are present like high content of the cement in alkaline, sulfate or C<sub>3</sub>S, or cement with high specific surface or concrete mix with high cement content and low water to cement ration.

Some other researchers hypothesized that DEF can occur in concrete cured at high temperature or not (Colleparidi, 1999). They believed that DEF occurs even in non-steam-cured concrete specimens at temperatures much lower than 70°C that are insufficient to cause thermal decomposition of the “normal” ettringite, which contradict the hypothesis that DEF is necessarily caused by decomposition of primary ettringite at temperature of 70°C.

### 2.2.2. Effect of Humidity During the Service Life of the Structure

Most cases of DEF have been found in environment with high humidity or complete immersion. In fact, water plays an important role in formation of secondary ettringite, as it is one of the reactants in the reaction leading to ettringite from monosulfate in the following equation:



In addition, water is the medium where the reaction takes place and is the vehicle for transport of ions involved. Heinz et al. (Heinz e Ludwig, 1987) found that DEF related expansion could be avoided if concrete is store in an environment with relative humidity below 60%. Odler (Odler e Chen, 1996), Famy (Famy *et al.*, 2001) found that specimen stored in an environment with relative humidity less than 90% did not display significant DEF induced expansion while they expanded significantly when stored immerse in water or in ambient air with relative humidity of 100%. This confirmed the role played by water in the development of DEF.

### 2.2.3. Effect of Cement Composition

#### a) - The Alkaline Content of Cement

Alkalis have been shown to play a significant role in DEF. They are present in cement as soluble salts like sodium sulfate ( $\text{Na}_2\text{SO}_4$ ), potassium sulfate ( $\text{K}_2\text{SO}_4$ ) (Bruneteaud, 2005) or mixture of sodium and potassium sulfate  $(\text{Na,K})_2\text{SO}_4$  (Pettifer e Nixon, 1980; Day, 1992). In contact with water, these salts are dissolved rapidly. The main effect of alkaline, like temperature, is to increase the solubility of ettringite and to lower that of lime (Barbarulo *et al.*, 2002). Fu (Fu e Beaudoin, 1996b) reported that ettringite is formed at PH 13.3 and low alkaline concentration (0.08M), however, it becomes unstable at temperature above 60°C and high alkaline concentration (0.2 to 1M). Under these conditions, monosulfate is the most stable phase. At the macroscopic level, Kurdowski (Kurdowski, 2001), Baghdadi (Baghdadi *et al.*, 2008), Lewis et al. (Lewis *et al.*, 1994) show that by adding alkali to mortar or concrete leads to expansion up to three times those obtained with no addition of alkalis.

### - Potassium Content of Cement

Multiple studies have shown that potassium plays an important role in the development of secondary ettringite in concrete. Gress (Gress, 1997) observed a significant correlation between the potassium content of the concrete and the degree of damage in field studies of concrete pavement. Livingston (Livingston *et al.*, 2000) surveying DEF related damages on bridges in Maryland concluded that the highest level of potassium in concrete were observed in areas with the DEF induced map cracking. It was then suggested that there might be a correlation between the potassium concentration and expansive damages. Potassium present in cement in the form of potassium sulfate reacts during cement hydration to produce a dilute potassium hydroxide solution and calcium sulfate.



The solution reacts with the atmosphere over time to produce potassium carbonate.



Since potassium carbonate has a very low critical relative humidity for deliquescence (RH=43%), under prevailing temperate conditions the compound is typically in a saturated solution rather than in solid form. That is why the cracks network associated with DEF usually appears wet or dripping with water (Livingston *et al.*, 2000).

### b) – The Sulfate Content of the Cement

Heinz and Ludwig (Heinz e Ludwig, 1987) showed that one of the main influence of cement composition on DEF derives from the  $\text{SO}_3/\text{Al}_2\text{O}_3$  ratio. However, the sulfate proportion appears to have a higher weight in determining behavior; therefore, they suggest that the ratio  $(\text{SO}_3)^2/\text{Al}_2\text{O}_3$  is a parameter that shows the strongest correlation to subsequent

effects of secondary ettringite formation. According to their research, cements with a ratio of 2.0 are not susceptible to secondary ettringite formation. According to Hime (Hime, 1996), some of the sulfur in the clinker phase is present as relatively slow soluble sulfate. These sulfates, which are not available for the primary ettringite formation, enter into the pore solutions and after hardening of the concrete, they react with  $C_4AH$  and water to form secondary ettringite.

#### 2.2.4. The Presence of Microcracks

Porosity, especially microcracking is one of the most important factors in delayed ettringite formation. Microcracks may be generated during manufacturing (localized high stress in prestressed elements for example). They can also be caused by freeze thaw, ASR or other causes including those related to high temperature curing (steam curing). Microcracks usually appear at the paste-aggregate interface (interfacial transition zone) and at the steel-paste interface (Fu e Beaudoin, 1996c). Microcracks serve as nucleation sites where ettringite crystals grow, expand and produce damages. Microcracks weaken concrete structure by reducing its modulus of elasticity and its resistance in tension, characteristics which are important to prevent expansion. In general, DEF induced expansion depend on the amount of microcracks present in concrete, their size, their location and the underlying causes. Microcracking is also important as it allows for the transport of ions required for formation of ettringite into the pores (Khelil, 2014).

Some researchers have minimized the role of microcracking in the development of secondary ettringite. Petrov (Petrov e Tagnit-Hamou, 2004) and Escadeillas (Escadeillas *et al.*, 2007) have shown that microcracking is not a necessary condition for DEF but that it accelerates DEF related expansion by allowing transfer within the material.

### 2.2.5. Other Parameters

Other parameters have been shown to play a role in the formation of delayed ettringite.

- The Type of Aggregates Used.

Grattan-Bellew (Grattan-Bellew *et al.*, 1998) show that the type of aggregate determines the amount of ettringite and expansion in heat-cured mortar samples. By comparing mortars made from six different types of aggregates (quartz, basalt, dolomite, granite, limestone, Spratt limestone), they noticed that mortar samples made with quartz were the only one to undergo significant expansions ( $> 0.1\%$ ) at 57 days (Figure 2-1). XRD analysis shows that the amount of ettringite is more important for mortars containing quartz (at the paste-aggregate interface in particular) than limestone.

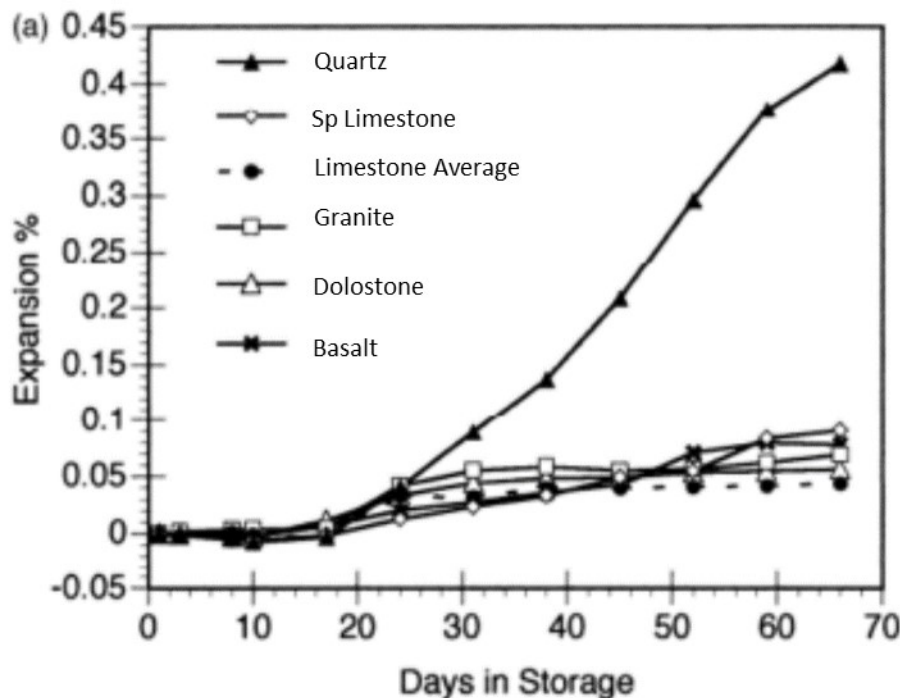


Figure 2-1: Expansion of Cement Mortars with Different Aggregate Types (Grattan-Bellew (Grattan-Bellew *et al.*, 1998))

In the same study, Grattan-Bellew et al. show that expansion is also dependent on the specific surface area of aggregates: the smaller the aggregate grain size, the more expansion and quantity of ettringite increase (inverse proportionality) with an acceleration of marked expansions as soon as the diameter of the grain fell below 1mm.

More recently, Amde et al. (Amde *et al.*, 2014) assess the influence of fine aggregate lithology of DEF related expansion of concrete specimen made with high early strength cement (type III cement). The study compared expansion of specimen made with fine aggregates having different lithology (place of origin, method of production and petrographic makeup) notably sand milled from limestone gravel from Millville, a siliceous sand produced from highly heterogeneous alluvial gravel from Brandywine and a siliceous very expansive natural sand from Silver Hill. The study showed that the specimens made with siliceous aggregates expanded significantly compare to those made with the crushed limestone sand.

## Chapter 3 : Conventional Methods for Characterizing DEF

### *3.1. Introduction*

Conventional methods for characterizing DEF in concrete at the microscopic scale can be classified in two main categories: Destructive methods and non-destructive methods. Destructive methods include petrographic examination, X-ray diffraction (XRD) and thermogravimetric analysis while nondestructive methods include ultrasonic pulse velocity, impact echo, the non-linear ultrasonic testing, the thermography, electromagnetic testing and radiographic imaging methods. Some of these techniques are extensively used on the field to assess concrete condition and detect deficiencies, while others are more suited as research tools used in laboratories. Most of these methods are subject of an abundant literature and have been commonly used in the study of DEF in concrete while others like the tomography are still in the experimental stage, and there are few cases where they have been used for this purpose.

### *3.2. Destructive Methods*

Destructive methods can be defined as those that require the use of equipment which produce an irreversible alteration of the chemical composition of the material being analyzed, their mechanical properties or their dimensional geometry. Destructive testing methods offer the advantage that they are usually cheaper and less complex to perform than non-destructive methods; however, their main drawback is that the specimens are not reusable.

### 3.2.1. The Microscopy Method: Petrographic Analysis

Petrography is the use of an optical microscope to examine concrete or rock samples in order to determine their mineralogy, chemical characteristics or microscopic structure. Petrography is the most commonly used method to characterize concrete damages at the microscopic level. Petrographic examination can render a range of concrete parameters like the type, proportion, shape and condition of aggregates, nature of cement paste and additives, and the presence of deleterious material, evidence of sulfate attack, frost or ASR. Petrographic examination of concrete samples is outlined in ASTM-C856-18 Standard Practice for Petrographic Examination of Hardened Concrete. Two types of specimens are commonly used: large polished surfaces and thin sections. Petrography has been intensively used to study the process of concrete deterioration due to DEF (Hime *et al.*, 2000; Matos *et al.*, 2010).

### 3.2.2. Scanning Electron Microscopy (SEM)

Scanning Electron Microscopy is a method to examine the microscopic structure of concrete using an electronic microscope that produces images of a sample by scanning the surface with a focused beam of high-energy electrons. The principle of the SEM is that a beam of accelerated electrons is directed towards a solid sample where the energy of the beam is dissipated as a variety of signals is produced by the electron-sample interaction when the incident electrons are decelerated in the solid sample. These signals include secondary electrons (That produce SEM images), backscattered electrons (that are used to determine the crystal structures and orientation of minerals), photons (Characteristics X-rays that are used for elemental analysis and continuum X-ray), visible light and heat. When equipped with appropriate detectors and electronics for Energy Dispersive X-ray

Spectroscopy, SEM can provide a rapid semi-quantitative compositional analysis of individual components within a specimen. SEM can be used as a standalone method or in conjunction with petrography. SEM for concrete specimens is governed by ASTM C1723-16 Standard Guide for Examination of Hardened Concrete Using Scanning Electron Microscopy. The method is discussed in more details in Chapter 6.

### 3.2.3. X-ray Diffraction (XRD)

The X-ray diffraction is a method that relies on the dual wave/particle nature of x-rays to obtain information about the structure of crystalline materials. The method relies on the Bragg's law which explains why the cleavage faces of crystals appear to reflect x-rays beams at certain angle of incidence (Khondker e Lakhani, 2015). Based on this principle, different crystals will produce different angle of diffraction, therefore, every crystalline phase in a sample has its own diffraction signature (Jumate e Manea, 2012). XRD method allows for the performance of the following studies: determination of crystalline structures, phase quantitative and qualitative analysis, the study of phase transformation, the study of crystallographic texture, the internal stresses in the sample, etc. (Jumate e Manea, 2012).

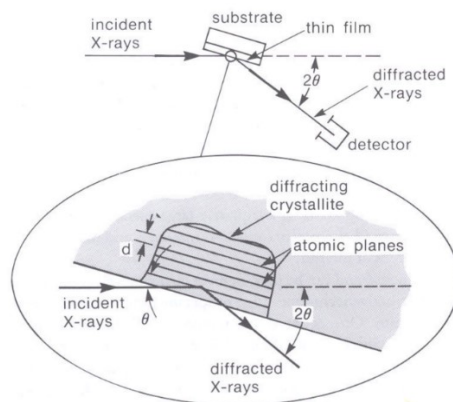


Figure 3-1: Principle of X-Ray Diffractometer

XRD has long been extensively used to study the cement hydration process. XRD is a useful technique for direct identification of crystalline phases in cement (Klug e Alexander, 1974), and its use have been extended to the study of cement hydration process in concrete (Jumate e Manea, 2012). It has been used to provide real time investigation of early hydration reactions such as the synthesis of ettringite (Muhamad *et al.*, 1993) and the rapid conversion of calcium aluminate cement hydrates (Rashid *et al.*, 1992). XRD has also been used in the rapid strength determination of Portland slag cements (Goswami *et al.*, 1994). XRD is performed on powder samples, therefore, concrete specimens that are to be analyzed are pulverized to a homogeneous powder ( $0.1\mu\text{m} < \text{particle size} < 40\mu\text{m}$ ) prior to been analyzed.

#### 3.2.4. Thermogravimetry Analysis (TGA)

Thermogravimetry Analysis or thermal gravimetric analysis (TGA) is a technique in which the mass of a substance is monitored as a function of temperature or time as the sample specimen is subjected to a controlled temperature program in a controlled environment. TGA provides quantitative measurement of mass change in material associated with thermal degradation. Thermogravimetry analysis is based on the principle that as a sample is heated, its mass changes. This change can then be used to determine the composition of the sample. The weight loss observed as the temperature increase is due to decomposition, reduction or evaporation of the constituents. TGA is relevant in the field on concrete because it can help quantify the amount of water and characterize and identify the phases from the complex cement matrix. TGA is commonly used to assess the behavior of concrete to the effect of temperature and fire (Alarcon-Ruiz *et al.*, 2005; Menedez e Vega, 2009). TGA can be used to detect the presence of ettringite in concrete because dehydration of

ettringite is characterized by an endothermic peak at 80-100°C. TGA has been used to detect primary and secondary ettringite in cementitious material (Vedalkshmi *et al.*, 2008; Collier, 2016; Tantawy, 2017). TGA is governed by ASTM E1131-08 Standard Test Method for Compositional Analysis by Thermogravimetry.

### 3.2.5. Limitation of Destructive Methods in the Study of Concrete Degradation Mechanism

There are numerous disadvantages in using destructive techniques mentioned above to study the mechanisms of concrete deterioration at the microscopic scale, specifically DEF induced damages. The most commonly mentioned drawbacks include:

- The lack of representativeness of very small sample volumes for heterogeneous concrete, the loss of spatial information such as the relationship of the ettringite growth to cement paste/aggregate interfaces; and
- These techniques are destructive which makes it impossible to monitor the progress of damage in a given specimen over time.

### 3.3. Non-destructive Techniques for Characterizing Distributed Damages in Concrete

In recent years, the use of nondestructive technique in the study of concrete damages has gained a lot of traction since it allows the understanding of concrete deterioration mechanisms without the need to destroy concrete samples. Non-destructive testing (NDT) is defined as the course of inspecting, testing, or evaluating materials, components or assemblies without destroying the serviceability of the part or system (Workman & O. Moore, 2012 cited by Helal et al. (Helal *et al.*, 2015)). Recent technological advances in imaging techniques have contributed in the development of various experimental imaging techniques used to visualize the interior microstructure of concrete and thus allow

characterization of damages with more accuracy. These imaging techniques include optical microscopy, scanning electron microscopy (SEM), and X-ray and neutron tomography. Each of these imaging modalities often shows different features at different spatial resolutions and Field of View.

DEF, ASR and FT induced damages in concrete do not necessarily contain large cracks or voids but are characterized by the existence of large numbers of small cracks or microcracks distributed throughout the concrete structure. These distributed damages that are usually initiated at the Interfacial Transition Zone (that is the interface between the paste and the aggregate) weakens the concrete and are precursor to large scale cracking and delamination.

There are numerous NDT methods that are used to detect damages in concrete. Most of them were designed and are more suitable for detection of large cracks and voids in concrete structure. Some of those methods like the ground penetration radar, the electric resistivity, the capacitive method (Metalssi *et al.*, 2015) have not yield reliable results so far for the detection and characterization of distributed damages like the ones caused by DEF, ASR or FT. The majority of the NDT are deductive by nature because they cannot provide the cause of the damages, nor the nature, the extent or the type of damage in concrete. The current research project aims at exploring the use of an innovative method to characterize damages in concrete. The criteria that guided the choice of the method are:

- It is nondestructive i.e. it preserves the integrity of the sample;
- It can allow for the visualization of the interior of the material, thus providing information on the nature and type of damage;

- It does not alter the microstructure and the composition of the sample;
- It can provide information on material property and its microstructure;
- It can allow for visualization of spatial distribution of damage in concrete and special distribution of concrete phases; and
- It allows for use of a representation sample of concrete.

We present herein a brief summary the most commonly used and some of the method that are being experimented for the detection and characterization of distributed damages like those caused by ettringite in concrete.

#### 3.3.1. The Ultrasonic Pulse Velocity Method

Ultrasonic pulse velocity methods involve propagating ultrasonic waves in solids while measuring the time taken for the waves to propagate between a sending and receiving point (Helal *et al.*, 2015). This is a standard method govern by ASTM C597 Standard Test Method for Pulse Velocity through Concrete. This test method is used to assess the uniformity and relative quality of concrete, to indicate the presence of voids and cracks, and to evaluate the effectiveness of crack repairs. It is also used to indicate changes in the properties of concrete, and in the survey of structures, to estimate the severity of deterioration or cracking.

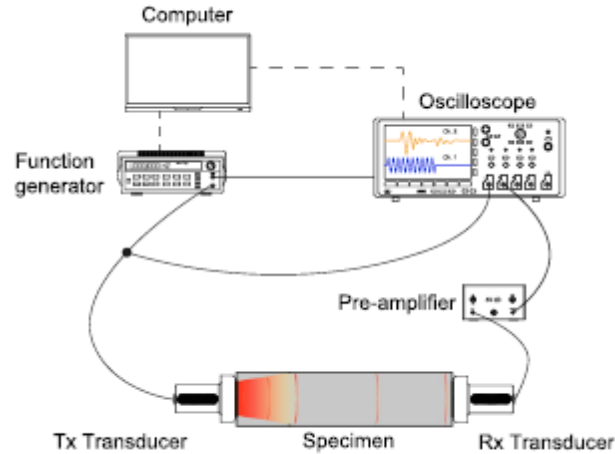


Figure 3-2: Equipment Used in a Typical Ultrasonic Pulse Velocity (Genoves *et al.*, 2017).

Recent studies have shown that UPV measurement can be accurately used to monitor the effect of DEF on concrete (Genoves *et al.*, 2017) and the effect of sodium sulfate and wetting drying cycles on concrete (Cruz *et al.*, 2016).

### 3.3.2. Impact Echo

This method is used on detection of defect in concrete based on stress wave propagation. The impact echo detects defects based on analysis of the reflection signals of impact-generated stress waves that propagate through the testing element (Zhang *et al.*, 2016). The principle of the impact echo is illustrated in Figure 3-3 and Figure 3-4 below.

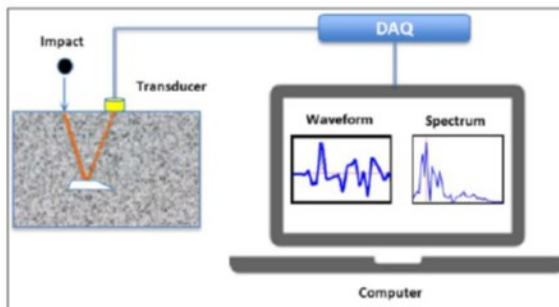


Figure 3-3: Schematic of impact Echo Method (Zhang *et al.*, 2016)

The impact-echo is used to evaluate integrity and flaws in concrete elements and structures, notably to detect internal cracks and voids. It has been intensively used in research since the inception of the method by Sansalone in the mid 80's. Recently McMorris demonstrated that the Q-factor generated from the impact echo can be used to quantify the amount of distributed damage induced in concrete specimen subjected to DEF and freeze thaw.

### 3.3.3. Non-Linear Ultrasonic Testing

The objective of ultrasonic methods is to measure the changes in characteristics of the ultrasonic signals propagating through the tested concrete. For linear methods, these characteristics may be the P-wave velocity, the amplitude attenuation and the frequency shift. For non-linear methods these may be the shape of the frequency spectrum and the harmonics generated by the internal discontinuities of the material. Non-linear techniques are more sensitive to distributed damages like those initiated by ASR, F-T or DEF than traditional ultrasonic methods. This increased sensitivity enables the detection of micro-cracks of a size undetectable by linear methods. Chen successfully used nonlinear wave modulation spectroscopy (NWMS) to monitor the progress of ASR damage in mortar samples (Chen *et al.*, 2008) while Lesnicki used nonlinear impact resonance acoustic spectroscopy (NIRAS) for tracking the progressive deterioration of concrete specimen due to ASR (Lesnicki *et al.*, 2011).

### 3.3.4. Radiographic Imaging Techniques

In opposition to the previous NDT methods which are commonly called conventional NDT techniques, radiographic methods are rather non-conventional NDT techniques that are mostly used as research tools. They are non-conventional because they

require a specific setting and specific equipment to be performed. Unlike conventional methods which can be performed on the field, they are usually performed in the laboratory. The principle of radiographic methods is based on attenuation of radiations from an artificial source going through a material. The type of radiation used are multitudinous, ranging from particles (Neutrons, electrons) to electromagnetic waves (X-rays,  $\gamma$ -rays), with specific selection depending upon the requirement of the application. Radiographic imaging techniques include the radiography and tomography. A thorough description of these imaging techniques is presented in Chapter 4.

## Chapter 4 : X-ray and Neutron Tomography for Characterization of Concrete Damage

### *4.1. Introduction*

Tomography along with radiography are two of the most commonly used radiographic imaging technique, which means that they use the interaction of a radiation and a sample to create an image of the sample, allowing visualization of the internal structure of the sample. The most commonly used radiations are X-rays, gamma rays and neutrons. Radiographic imaging methods have long been used to study concrete in order to determine certain physical properties, its structure or to characterize physical or chemical damages. We provide herein a background on the use of x-ray and neutron tomography in the study of concrete.

### *4.2. Background on X-ray and Neutron Tomography for Characterization Of Concrete Damages*

#### 4.2.1. Introduction

As Radiation-based NDT Imaging techniques, tomography requires a comprehensive understanding of various aspects including beam generation, radiation detection, image reconstruction, image processing, 3D visualization and image analysis. Tomography has been used on concrete and cement-based materials for various applications. This section will focus on previous application of neutron and X-ray tomography on concrete.

#### 4.2.2. Historical Background

##### a) X-ray Tomography

Wilhelm Röntgen discovered X-rays in 1895 by accident and the first X-ray image was that of his wife's hand (August, 1896).

Radon established theoretical foundation of computed tomography (CT) in 1917. Radon showed mathematically that a function could be reconstructed from an infinite set of its projections (Radon, 1986). In the late 1960s and early 1970s, Cormack and Hounsfield worked based on Röntgen's discoveries and the work of Radon, developing a method of producing axial images of "slices" of the human body. Hounsfield and colleagues built the first medical CT machine (Hounsfield, 1973). Cormack and Hounsfield shared the 1979 Nobel Prize in Medicine. In 1970, hospitals started performing X-ray tomography. In 1980s, dedicated Synchrotron light sources that generate intense X-ray beam were built. Since Computed tomography primary application was in the medical field, its use in material research did not start until later.

One of the first documented used of computed tomography as a nondestructive testing method for concrete was achieved by Morgan in 1979 (Morgan *et al.*, 1980). The researcher used a cesium-137 isotopic source to provide 662 KeV photon beams, with plastic scintillator strips to detect and count each transmitted photon. The tomograms (cross sectional density maps) that were obtained showed aggregates and voids down to 1mm in diameter, and fractures less than 1mm wide. The location and density of reinforcement bars, the density and background mortar and the density of the aggregate were accurately reconstructed.

In 1994, Bentz performed X-ray tomography of an ASCTM C109 mortar sample exposed to sulfate attack. The X-ray tomography was done at the National Synchrotron Light Source (NSLS) of Brookhaven National Laboratory using Exxon's microtomography scanner to obtain 3-D images at a resolution of a few micrometers per voxel. The images clearly showed sand grains, cement paste, air voids, cracks and needle-like crystals of ettringite growing in the air voids (Bentz *et al.*, 1994). This research set the tone for his subsequent works on the microstructure, transport properties and degradation processes in mortars and concrete using X-ray tomography (Bentz *et al.*, 2000).

High-resolution X-ray computed tomography (also referred to as microtomography) was used by Stock to study the sulfate attack of cylinders of Type I cement paste cast with various water–cement ratios (Stock *et al.*, 2002). 3-D rendering of the images obtained allowed the authors to access the qualitative damage level as a function of sulfate exposure time for various ratios studied.

Landis use high resolution X-ray tomography to measure internal damage and crack growth in small mortar cylinders in compression (Landis *et al.*, 1999). He was able to visualize crack growth both in length and in thickness and make quantitative measurements of internal microstructural features. Further research, using the same technique allowed the author to study effects of crack tortuosity, branching and microcracking and obtain a detailed picture of internal crack progression (Landis *et al.*, 2007).

Bentz used X-ray microcomputed tomography to study water movement in concrete during curing (Bentz *et al.*, 2006). The technique allowed him to investigate migration of water on an entire specimen and isolate water movement from individual pores in the aggregate

to the surrounding cement paste during the hydration process. Quantitative analysis of water movement based on image processing was also achieved.

Lu used X-ray tomographic imaging technique to characterize the pore structure and permeability in 4 different Portland cement concretes (Lu *et al.*, 2006). Through this research, the “disconnected pore distance” was identified as a physical parameter that might correlate with chloride transport.

Most recently, Meinel used X-ray computed tomography as a tool to quantify the degradation process in concrete resulting from corrosion of reinforcing steel due to carbonation and to chloride ingress (Meinel *et al.*, 2014). By visualizing it at a high resolution (5 microns), the authors identified the interfacial transition zone (ITZ) as an important factor for the ageing stability of concrete.

#### *b) Neutron Tomography*

Neutron was first discovered by Chadwick in 1932 (Chadwick, 1932a; b). The first reactor was built by Fermi for neutron production in 1942. In 1947, the first neutron images were obtained by Kallmann (Kallmann, 1947). Neutron imaging at research reactor was performed by Thewlis in 1956 (Thewlis, 1956).

Even though the use of Neutron tomography to study concrete is more recent, there is a growing literature in the subject matter especially in the study of transport properties and drying of concrete based on the fact that neutron beam is highly attenuated by substances containing hydrogen like water.

Trtik *et al.* used neutron tomography to monitor the emptying of a superabsorbent polymer in a low water to cement paste (Trtik *et al.*, 2010). They analyzed the histograms of

successive neutron tomographies to measure the release of water by the superabsorbent polymer and its absorption by the paste. Most recently, Dauti et al. (Dauti *et al.*, 2017) presented their preliminary findings on the causes of concrete spalling. Their method uses fast neutron tomography of heated concrete samples. The use of fast neutron allowed the study of the dehydration process of concrete leading to spalling. They demonstrated that the moisture distribution is influenced by the aggregates type, size and distribution. They were then able to propose a model for the underlying processes.

Lucero et al. used neutron tomography to quantify water transport and degree of saturation in an air entrained cement-based mortar, in an effort to understand the process by which air entrainment helps reduce the potential for freeze thaw of concrete (Lucero, C.L. *et al.*, 2015). The researchers developed a model based on Beer's Law to predict the degree of saturation of mortar without using a reference image in the dry state as it is commonly done in neutron imaging. By expanding Beer's Law and having knowledge of mortar mixture proportions and degree of hydration, the percent of water in the pores could be estimated.

Wyrzykowski performed tomography scans of mortar samples at the thermal neutron beamline at Scherer institute to study the effect of shrinkage reducing admixture on plastic shrinkage of mortars made with lightweight aggregates (Wyrzykowski *et al.*, 2015). Taking advantage of recent developments in algebraic reconstruction techniques and non-sequential decomposition of projection angles, which allow for tomographic scans of dynamic water transport in early-age cementitious materials, the researchers made CT scans at short temporal resolution of the drying process.

As seen above, X-ray and neutron tomography have been separately used intensively as a research tool to study hydration processes in concrete and degradation mechanisms. While

X-ray helps researchers analyze the strain-stress mechanism and the strain distribution within concrete, neutron is mostly used to understand the underlying chemical processes leading generation of internal stresses in concrete. The simultaneous use of X-ray and neutron tomography can therefore provide a more holistic approach in the understanding of degradation of concrete, its manifestation and the processes leading to this degradation.

#### 4.3. General Principle of Radiographic Imaging

The universal principle for radiographic imaging techniques is that: as the radiation passes through the specimen, it is attenuated by an amount that depends both on the thickness of the specimen along the path taken by the radiation, and on the materials present along that path.

The transmission,  $T$  is the ratio of the transmitted beam intensity,  $I(E)$ , to the incident beam intensity  $I_0(E)$  :

$$T = I(E)/I_0(E) \quad \text{Eq. 5}$$

For a narrow path, the transmission behavior of the radiation can be described according to the Beer's law (De Beer *et al.*, 2004):

$$\text{For a homogeneous material } I(E) = I_0(E)e^{(-\mu(E)d)} \quad \text{Eq. 6}$$

$$\text{For a heterogeneous material } I(E) = I_0(E)e^{\int_1 (-\mu(E)(x)d(x))} \quad \text{Eq. 7}$$

Where  $I(E)$  is the intensity of the transmitted radiation beam,  $I_0(E)$  the intensity of the incident beam,  $\mu(E)$  the attenuation coefficient of the material under investigation for the specific radiation type,  $d$  the length of the radiation path through the object, i.e. the thickness of the sample.

In this equation, the parameters  $I(E)$ ,  $I_0(E)$  and  $\mu(E)$  are radiation energy dependent, meaning that a material will attenuate different radiations by different magnitude. It also means that an element has different attenuation properties at different energy levels for the same radiation type.

#### 4.3.1. X-ray Attenuation VS Neutron Attenuation

X-ray and neutron are the 2 most common radiations used in radiographic imaging techniques and are therefore the main subject of our research. When a radiation interacts with matter, 3 types of responses can be observed: the radiation can simply continue without interaction with the matter (transmission), it can be absorbed by the matter or it can be scattered into a different direction. The portion of the radiation which is absorbed or scattered constitute the attenuation for that radiation.

X-ray radiation interaction with material depend on the density of the sample, i.e. the electron cloud density (De Beer *et al.*, 2004). The X-ray attenuation is a function mainly of the local electron density which increases monotonically with the atomic number of the element. X-ray attenuation in a material is due to four interactions:

- The Photoelectric effect: In this interaction mode, the incident photon transfers all its energy to atoms of the matter and cease to exist while atoms emit electrons and hence becomes ionized.
- The Thomson Scattering also known as Rayleigh or Coherent or Classical scattering: The photon interacts with the whole atom so that the photon is scattered with no change in internal energy to the electron and changes direction.

- The Compton Scattering: In this case, the photon interacts with a free electron. The electron gains energy and is ejected from its orbital position. The X-ray photon loses energy due to the interaction but continues to travel through the material along an altered path. The scattered radiation has a longer wavelength than the incident radiation.
- Photodisintegration (PD) is the process by which the X-ray photon is captured by the nucleus of the atom with the ejection of a particle from the nucleus when all the energy of the X-ray is given to the nucleus. Because of the enormously high energies involved, this process may be neglected for the energies of x-rays used in radiography.
- Pair production: In this interaction mode, the incident photon disappears, and two particles are created: an electron and a positron. The pair production can occur when the photon energy is greater than 1.02 MeV, but really only becomes significant at energies around 10 MeV.

The total cross section for X-rays for atom  $i$ ,  $\sigma_{i,x}^{X-ray}$ , is then given by the equation:

$$\sigma_{i,x}^{X-ray} = \sigma_i^{Ts} + \sigma_i^{PA} + \sigma_i^{CS} + \sigma_i^{PP} + \sigma_i^{PD} \quad \text{Eq. 8}$$

Where  $\sigma_i^{Ts}$ ,  $\sigma_i^{PA}$ ,  $\sigma_i^{CS}$ ,  $\sigma_i^{PP}$   $\sigma_i^{PD}$  are X-ray atomic cross sections for Thompson scattering, photoelectric absorption, Compton scattering, pair production and photodisintegration respectively (Wei-Shan *et al.*, 2017). Elements with low density attenuate less x-rays than elements with higher density. Table 4-1 shows X-ray attenuation coefficient of elements in the periodic table at 125 KeV energy level.

The interaction of neutron rays with materials is different to that of X-rays. Neutrons are not affected by the density of the material, but instead they interact with the atom nucleus. Neutron attenuation depends upon parameters such as: ((Wei-Shan et al., 2017)

- Absorption or radiative capture ( $\sigma_i^{RC}$ ): The incident neutron is capture by the nucleus of the atom with emission of a gamma and an isotope.
- Elastic scattering ( $\sigma_i^{ES}$ ): The incident neutron transfers some of its energy to the nucleus of the atom and bounce in a different direction.
- Inelastic scattering ( $\sigma_i^{iES}$ ): The incident neutron is absorbed by the nucleus and emission of lower energy neutron and gamma.
- The fission ( $\sigma_i^F$ ). Upon interaction of the neutron and the atom nucleus the nucleus splits and more nucleons are released.

The total neutron cross section for an atom  $i$ ,  $\sigma_{i,x}^{Neutron}$  can be written as:

$$\sigma_{i,x}^{Neutron} = \sigma_i^{ES} + \sigma_i^{iES} + \sigma_i^{RC} + \sigma_i^F + \dots \quad \text{Eq. 9}$$

In which  $\sigma_i^{ES}$ ,  $\sigma_i^{iES}$ ,  $\sigma_i^{RC}$  and  $\sigma_i^F$  are the elastic scattering, inelastic scattering, radiative capture and fission neutron cross sections respectively. Table 4-2 shows neutron cross section of element in the periodic table.

Hydrogen is one of the most common elements with the highest neutron cross-section (3.44 cm<sup>-1</sup>) and consequently, neutron imaging methods are particularly useful for characterizing hydrogenous materials. Therefore, the neutron attenuation in concrete is dominated by hydrogen atom concentration. Since the expansive phases in concrete all contain hydrogen, this suggests that neutrons could be useful to identifying the individual phases.

Consequently, hydrous phases such as C-S-H gel, calcium hydroxide, ASR gel, ice and ettringite present in concrete can be individually identified with neutron radiations.

#### 4.3.2. Principle of Radiography

In radiography, a source of radiation emits penetrating radiation (X-ray, Neutron or gamma) towards a sample. The incident radiation is attenuated (scattered and/or absorbed) by the material and a sensitive detector, with a high quantum efficiency for the detection of the specific type of radiation registers the difference in attenuated radiation that has passed through the sample (De Beer *et al.*, 2004). This produces a 2-dimension grey-scale image (also called shadowgraph or radiograph) which may be considered as a measure of the spatially varying integrated attenuation properties of the specimen and holds information about the sample thickness (including the presence of cracks and voids) and the chemical composition. If accurate details of the morphology or the chemistry of the sample are known, it is then possible to extract quantitative data.

#### 4.3.3. Principle of Tomography

Tomography is based on the principle of radiography. In tomography, an object placed on a stage is rotated 180 degrees, while radiographs are taken at defined angular positions. A complete 3-Dimension image composition of the object is then computationally reconstructed (for example using the filtered back projection algorithm) with the radiographs. The filtered back projection is a one of the fastest and most efficient and widely used method technique use to reconstruct 3-D images from projections. The sections below give an in-depth understanding and background on the principle of tomography.

#### 4.4. Dual modality Imaging: Neutron and X-ray Tomography

##### 4.4.1. Complementarity of X-ray and Neutron Tomography

As we have seen previously, Neutron and X-ray radiations interact with materials in a completely different way: While X-ray mainly interacts with the electron cloud of an atom, the Neutron rays interact to the nucleus of elements constituting the material as shown in figure (Figure of interaction with matter). Neutron attenuation depends upon the absorption and scattering cross-sections of the nucleus which can vary significantly from one element to the next as it can be seen in Table (Periodic table with neutron). As can be seen in table (periodic table with x-ray), as the atomic number increases, the X-ray cross section increases since the size of the electron cloud increases. However, there is no particular trend for neutron total macroscopic cross section.

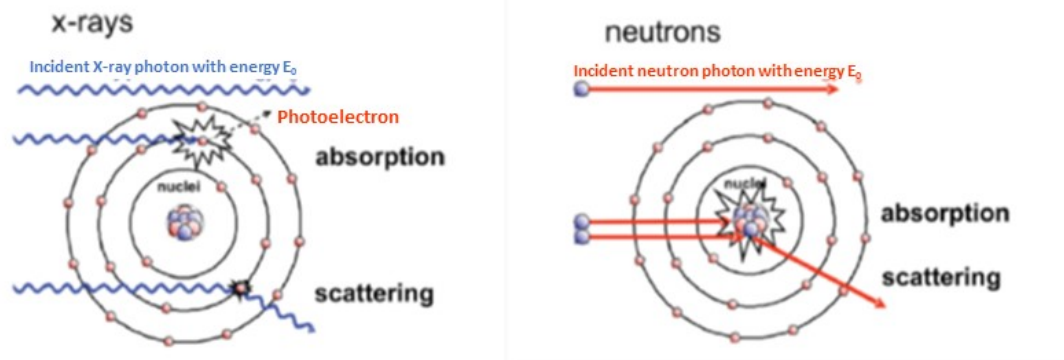


Figure 4-1: Interaction of Matter with X-Ray and Neutron (Strobl et al. 2009 cited by Kim (Kim, 2013))

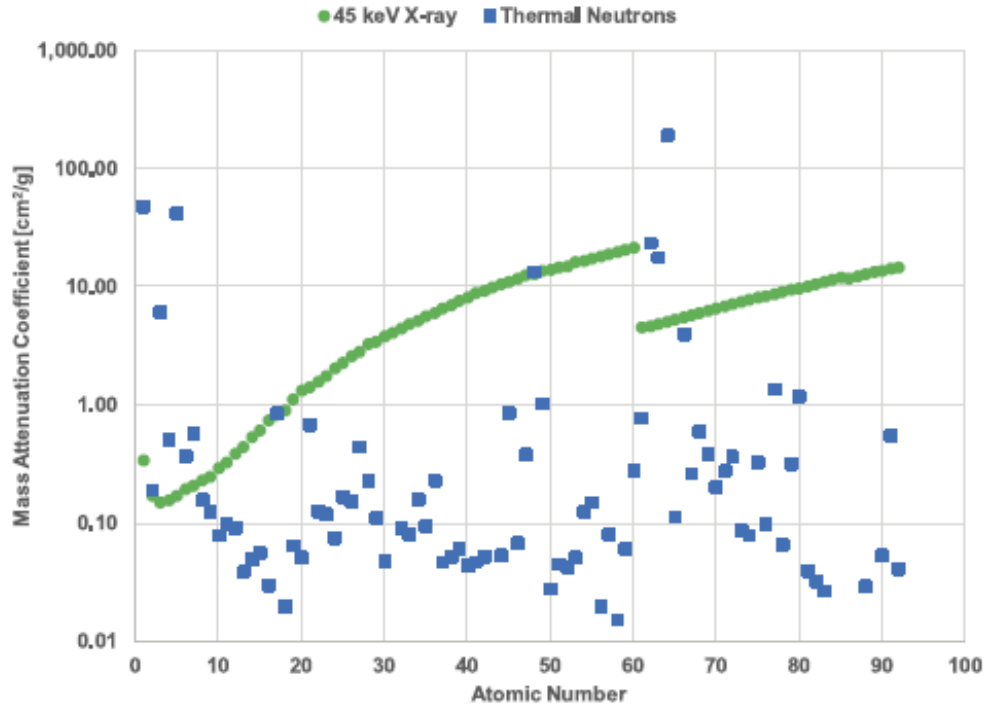


Figure 4-2: Comparison of 45 KeV X-ray and 25 meV thermal neutron Mass Attenuation Coefficients as a Function of Atomic Number, Where the neutron Cross Section Assumes Natural Isotopic Abundances. (Source: LaManna (Lamanna *et al.*, 2017))

Table 4-1: Periodic Table with X-ray Attenuation Coefficient of Elements for 125 KeV Energy (Grunauer 2005 Cited by De Beer et al. 2005)

Attenuation Coefficient for 125 KV X-ray (cm <sup>-1</sup> )																	
<b>H</b> hydrogen 0.02																	<b>He</b> helium 0.02
<b>Li</b> lithium 0.06	<b>Be</b> beryllium 0.22											<b>B</b> boron 0.28	<b>C</b> carbon 0.27	<b>N</b> nitrogen 0.11	<b>O</b> oxygen 0.16	<b>F</b> fluorine 0.14	<b>Ne</b> neon 0.17
<b>Na</b> sodium 0.13	<b>Mg</b> magnesium 0.24											<b>Al</b> aluminum 0.38	<b>Si</b> silicon 0.33	<b>P</b> phosphorus 0.25	<b>S</b> sulfur 0.30	<b>Cl</b> chlorine 0.23	<b>Ar</b> argon 0.20
<b>K</b> potassium 0.14	<b>Ca</b> calcium 0.26	<b>Sc</b> scandium 0.48	<b>Ti</b> titanium 0.73	<b>V</b> vanadium 1.04	<b>Cr</b> chromium 1.29	<b>Mn</b> manganese 1.32	<b>Fe</b> iron 1.57	<b>Co</b> cobalt 1.78	<b>Ni</b> nickel 1.96	<b>Cu</b> copper 1.97	<b>Zn</b> zinc 1.64	<b>Ga</b> gallium 1.42	<b>Ge</b> germanium 1.33	<b>As</b> arsenic 1.50	<b>Se</b> selenium 1.23	<b>Br</b> bromine 0.90	<b>Kr</b> krypton 0.73
<b>Rb</b> rubidium 0.47	<b>Sr</b> strontium 0.86	<b>Y</b> yttrium 1.61	<b>Zr</b> zirconium 2.47	<b>Nb</b> niobium 3.43	<b>Mo</b> molybdenum 4.29	<b>Tc</b> technetium 5.06	<b>Ru</b> ruthenium 5.71	<b>Rh</b> rhodium 6.06	<b>Pd</b> palladium 6.13	<b>Ag</b> silver 5.67	<b>Cd</b> cadmium 4.84	<b>In</b> indium 4.31	<b>Sn</b> tin 3.98	<b>Sb</b> antimony 4.28	<b>Te</b> tellurium 4.06	<b>I</b> iodine 3.45	<b>Xe</b> xenon 2.53
<b>Cs</b> cesium 1.42	<b>Ba</b> barium 2.73	<b>La</b> lanthanum 5.04	<b>Hf</b> hafnium 19.7	<b>Ta</b> tantalum 25.47	<b>W</b> tungsten 30.49	<b>Re</b> rhenium 34.47	<b>Os</b> osmium 37.92	<b>Ir</b> iridium 39.01	<b>Pt</b> platinum 38.61	<b>Au</b> gold 35.94	<b>Hg</b> mercury 25.88	<b>Tl</b> thallium 23.23	<b>Pb</b> lead 22.81	<b>Bi</b> bismuth 20.26	<b>Po</b> polonium 20.22	<b>At</b> astatine	<b>Rn</b> radon 9.77
<b>Fr</b> francium	<b>Ra</b> radium 11.80	<b>Ac</b>	<b>Rf</b> rutherfordium	<b>Db</b> dubnium	<b>Sg</b> seaborgium	<b>Bh</b> bohrium	<b>Hs</b> hassium	<b>Mt</b> meitnerium	<b>Ds</b> darmstadtium	<b>Rg</b> roentgenium	<b>Cn</b> copernicium	<b>Nh</b> nihonium	<b>Fl</b> flerovium	<b>Mc</b> moscovium	<b>Lv</b> livermorium	<b>Ts</b> tennessine	<b>Og</b> oganeson
lanthanides (rare earth metals)	<b>Ce</b> cerium 5.79	<b>Pr</b> praseodymium 6.23	<b>Nd</b> neodymium 6.46	<b>Pm</b> promethium 7.33	<b>Sm</b> samarium 7.68	<b>Eu</b> europium 5.66	<b>Gd</b> gadolinium 8.69	<b>Tb</b> terbium 9.46	<b>Dy</b> dysprosium 10.17	<b>Ho</b> holmium 10.91	<b>Er</b> erbium 11.70	<b>Tm</b> thulium 12.49	<b>Yb</b> ytterbium 9.32	<b>Lu</b> lutetium 14.07			
	<b>Th</b> thorium 28.95	<b>Pa</b> protactinium 39.65	<b>U</b> uranium 49.06	<b>Np</b> neptunium	<b>Pu</b> plutonium	<b>Am</b> americium	<b>Cm</b> curium	<b>Bk</b> berkelium	<b>Cf</b> californium	<b>Es</b> einsteinium	<b>Fm</b> fermium	<b>Md</b> mendelevium	<b>No</b> nobelium	<b>Lr</b> lawrencium X-Ray			

Table 4-2: Periodic Table with Thermal Neutron Energy Attenuation Coefficient of Elements (grunauer 2005 Cited by De Beer 2015)

Attenuation Coefficient for Thermal Neutron (cm <sup>-1</sup> )																						
<b>H</b> hydrogen 3.44																		<b>He</b> helium 0.02				
<b>Li</b> lithium 3.30	<b>Be</b> beryllium 0.79																<b>B</b> boron 101.6	<b>C</b> carbon 0.58	<b>N</b> nitrogen 0.43	<b>O</b> oxygen 0.17	<b>F</b> fluorine 0.20	<b>Ne</b> neon 0.10
<b>Na</b> sodium 0.09	<b>Mg</b> magnesium 0.15																<b>Al</b> aluminum 0.10	<b>Si</b> silicon 0.11	<b>P</b> phosphorus 0.12	<b>S</b> sulfur 0.06	<b>Cl</b> chlorine 1.33	<b>Ar</b> argon 0.03
<b>K</b> potassium 0.06	<b>Ca</b> calcium 0.08	<b>Sc</b> scandium 2.00	<b>Ti</b> titanium 0.60	<b>V</b> vanadium 0.72	<b>Cr</b> chromium 0.54	<b>Mn</b> manganese 1.21	<b>Fe</b> iron 1.19	<b>Co</b> cobalt 3.92	<b>Ni</b> nickel 2.05	<b>Cu</b> copper 1.07	<b>Zn</b> zinc 0.35	<b>Ga</b> gallium 0.49	<b>Ge</b> germanium 0.47	<b>As</b> arsenic 0.67	<b>Se</b> selenium 0.73	<b>Br</b> bromine 0.24	<b>Kr</b> krypton 0.01					
<b>Rb</b> rubidium 0.08	<b>Sr</b> strontium 0.14	<b>Y</b> yttrium 0.27	<b>Zr</b> zirconium 0.29	<b>Nb</b> niobium 0.40	<b>Mo</b> molybdenum 0.52	<b>Tc</b> technetium 1.76	<b>Ru</b> ruthenium 0.58	<b>Rh</b> rhodium 10.88	<b>Pd</b> palladium 0.78	<b>Ag</b> silver 4.04	<b>Cd</b> cadmium 115.11	<b>In</b> indium 7.58	<b>Sn</b> tin 0.21	<b>Sb</b> antimony 0.30	<b>Te</b> tellurium 0.25	<b>I</b> iodine 0.23	<b>Xe</b> xenon 0.43					
<b>Cs</b> cesium 0.29	<b>Ba</b> barium 0.07	<b>La</b> lanthanum 0.52	<b>Hf</b> hafnium 4.99	<b>Ta</b> tantalum 1.49	<b>W</b> tungsten 1.47	<b>Re</b> rhenium 8.95	<b>Os</b> osmium 2.24	<b>Ir</b> iridium 30.46	<b>Pt</b> platinum 1.46	<b>Au</b> gold 6.23	<b>Hg</b> mercury 16.21	<b>Tl</b> thallium 0.47	<b>Pb</b> lead 0.38	<b>Bi</b> bismuth 0.27	<b>Po</b> polonium	<b>At</b> astatine	<b>Rn</b> radon					
<b>Fr</b> francium	<b>Ra</b> radium 0.34	<b>Ac</b>	<b>Rf</b> rutherfordium	<b>Db</b> dubnium	<b>Sg</b> seaborgium	<b>Bh</b> bohrium	<b>Hs</b> hassium	<b>Mt</b> meitnerium	<b>Ds</b> darmstadtium	<b>Rg</b> roentgenium	<b>Cn</b> copernicium	<b>Nh</b> nihonium	<b>Fl</b> flerovium	<b>Mc</b> moscovium	<b>Lv</b> livermorium	<b>Ts</b> tennessine	<b>Og</b> oganeson					
lanthanides (rare earth metals)	<b>Ce</b> cerium 0.14	<b>Pr</b> praseodymium 0.41	<b>Nd</b> neodymium 1.67	<b>Pm</b> promethium 5.72	<b>Sm</b> samarium 171.47	<b>Eu</b> europium 94.58	<b>Gd</b> gadolinium 1479.04	<b>Tb</b> terbium 0.93	<b>Dy</b> dysprosium 32.42	<b>Ho</b> holmium 2.25	<b>Er</b> erbium 5.48	<b>Tm</b> thulium 3.53	<b>Yb</b> ytterbium 1.40	<b>Lu</b> lutetium 2.75								
	actinides	<b>Th</b> thorium 0.59	<b>Pa</b> protactinium 8.46	<b>U</b> uranium 0.82	<b>Np</b> neptunium 9.80	<b>Pu</b> plutonium 50.20	<b>Am</b> americium 2.96	<b>Cm</b> curium	<b>Bk</b> berkelium	<b>Cf</b> californium	<b>Es</b> einsteinium	<b>Fm</b> fermium	<b>Md</b> mendelevium	<b>No</b> nobelium	<b>Lr</b> lawrencium Neut.							

Table 4-3: Neutron Attenuation Coefficient of Common Phases Found in Concrete

Phase	Formula	Molecular weight g/mol	H fraction	Density g/cm <sup>3</sup>	H density Atoms/cm <sup>3</sup>	Attenuation coefficient cm <sup>-1</sup>
Quartz	SiO <sub>2</sub>	60.09	0	2.65	0	0.284
Limestone	CaCO <sub>3</sub>	100.09	0	2.72	0	0.258
CSH gel <sup>a</sup>	(CaO) <sub>1.7</sub> (SiO <sub>2</sub> )(H <sub>2</sub> O) <sub>1.8</sub>	187.83	0.019	2.61	0.0499	2.731
Calcium hydroxide	Ca(OH) <sub>2</sub>	74.08	0.027	2.23	0.0602	3.193
Ettringite	(CaO) <sub>3</sub> ·Al <sub>2</sub> O <sub>3</sub> (CaSO <sub>4</sub> ) <sub>3</sub> ·(H <sub>2</sub> O) <sub>32</sub>	1254.62	0.051	1.77	0.0903	4.675
ASR gel <sup>b</sup>	Na <sub>2</sub> O·xSiO <sub>2</sub> ·y H <sub>2</sub> O x = 4-22 y = 5-10	214.08 - 1563.78	0.012 - 0.032	1.93 - 2.46	0.0314 - 0.0631	1.833 - 3.355
Water ice	H <sub>2</sub> O	18.00	0.111	0.9	0.1000	5.081

<sup>a</sup>Allen et al. 2007

<sup>b</sup>Broeckmann, 2012

This difference in interaction of X-ray and neutron with matters, thus different cross section, can be useful in tomography because it enables a more accurate estimation of the composition of the sample being investigated (Liu *et al.*, 2009). For example, Neutron has high attenuation coefficient for light atoms such as hydrogen while X-ray hardly provides contrast. Similarly, Neutron can easily penetrate some heavy material (aggregates for example) compare to X-ray. This makes Neutron and X-ray two very complementary modalities for material with hydrous phases like concrete, where we want to observe the distribution of hydrogenous material within the mineral matrix (LaManna *et al.*, 2017). In fact, X ray will provide good sensitivity to the matrix (aggregates) while neutron will provide good sensitivity to hydrous phases like C-S-H gel, calcium hydroxide, potential ASR gel, water and ettringite. Table 4-3 summarizes the calculations of neutron attention coefficients for phases typically found in concrete, including quartz and limestone aggregates. The CSH gel composition is based on Allen et al. (Allen *et al.*, 2007), and the

ASR gel composition on Broeckmans (Castro *et al.*, 2012). Figure 5-7 is a plot of attenuation coefficient of concrete phases for thermal neutron against X-Rays and it shows that there is a great dispersion of points, meaning that the phases are more clearly separated from each other. In this case X-ray and Neutron imaging can be used to complement each other to reveal comprehensive information about the sample investigated. Therefore, to perform “a dual mode tomography with neutron and X-ray offers the potential of improved estimation of the composition of a sample from the complementary interaction of the two probes with the sample.” (Lamanna *et al.*, 2017).

#### 4.4.2. Background on the Use of Dual Modality Tomography: Neutron and X-ray

The approach of combining Neutron and X-ray tomography have demonstrated its potential in different other fields. Vontobel did one of the early experimentation of the approach in 2005 to investigate rock (Vontobel *et al.*, 2005). Since then, It has been used in different fields: in the nuclear industry (De Beer, 2015), in archeology to study historical objects (Mannes *et al.*, 2014; Mannes *et al.*, 2015), in the study of fuel cells (Manke *et al.*, 2001), in material science (John *et al.*, 2010), in earth science, geology (Wei-Shan *et al.*, 2017; Vontobel *et al.*, 2005; Lamanna *et al.*, 2016) and other areas. It is used commonly to complement conventional destructive methods of analysis. The use of neutron tomography combined with x-ray tomography in concrete research is recent and has been used mostly to analyze the hydration mechanism, moisture transport in concrete and cementitious material and the resulting degradation.

Trtik *et al.* (Trtik *et al.*, 2011) and Lura *et al.* (Lura *et al.*, 2014) combined neutron and X-ray tomography imaging techniques to study internal curing in concrete with lightweight

aggregate. Trtik's study focused on evaluating the change in water distribution within concrete while Lura's study evaluated the use of lightweight aggregate from biomass-derived waste (bio-LWA) as a means to mitigate concrete shrinkage. Both studies used a method described as 4D computer tomography in which neutron and X-ray CT are applied repeatedly over time nondestructively on the specimen, which allow for the measurement of water released by the lightweight aggregate and water content of the concrete as a function of time. Subtracting 3D images obtained by subsequent neutron tomographies was used to evaluate the change in water distribution within the concrete sample while segmentation performed on X-ray tomographies was used to determine the boundaries of the LWA in the concrete specimen.

Kim used dual modality imaging (Neutron and X-ray tomography) in order to characterize the flow through porous media (Kim, 2013; Kim *et al.*, 2015). Advanced image registration technique was used to combine the dual modality data in order to achieve quantitative analysis. The grain size distribution, the pore size distribution and the water saturation along the height of the specimens studied were obtained from the image data and the author was able to perform predictive simulations to obtain capillarity pressure.

The current project, which is an attempt to use two modalities (neutron and X-ray) tomography to characterize DEF induced damages in concrete, falls in line with the previous studies herein mentioned. However, it draws its originality from two main particularities:

- The fact that the two tomographies are done simultaneously. In all previous studies mentioned above the two modalities imaging were implemented in a serial configuration where the sample was imaged with one technique

followed by the other. The problems arise when investigating samples that slowly evolve with time or stochastic processes as samples will not be identical for each imaging mode as scans can take around 12 h to 24 h or more to complete (LaManna et al. 2017).

- The second particularity is the fact that the current study goes beyond a mere observation of mechanisms taking place in concrete and attempts to quantify the amount of ettringite forming in concrete over time.

## Chapter 5 : Sample Preparation and Materials

### 5.1. *Introduction*

The materials used and corresponding specifications are outlined. The concrete specimens used in this study were prepared in the Civil Engineering Laboratory of the University of Maryland at College Park (UMD) and at the National Ready-Mix Concrete Association Laboratory (NRMCA) in Greenbelt, Maryland. The literature review and previous research done at UMD (Ceesay, 2007; Mcmorris, 2009) have demonstrated that adding potassium to the concrete mixture can accelerate the formation of DEF and thus the deterioration of concrete.

Two concrete batches were made for this project: the first batch with the normal content of potassium contained in the cement (0.79% of the weight of cement) was used to make two sets of specimens called Set 1 and Set 3. The other batch had potassium carbonate ( $K_2CO_3$ ) added to the mixing water in order to increase its potassium content to 1.72% by weight of cement. That batch was used to make one set of specimens called Set 2. Specimens from Set 1 and Set 2 would later undergo heat treatment. The two concrete batches were proportioned and mixed in the same manner as described below. The specimens to be heat-treated were subjected to a heat cycle.

### 5.2. *Experimental*

Concrete specimens were made and cured according to ASTM C192-16 Standard Practice for Making and Curing Concrete Test Specimens in the Laboratory (ASTM 2016). In order to accelerate Delayed Ettringite Formation, the specimens were subjected to Duggan heat cycle. In addition the samples were cast with end gage steel studs instead (Ceesay *et al.*,

2007; Amde *et al.*, 2003). The aim of using specimens cast with end gages was to facilitate length change measurements.

#### 5.2.1. Sample Preparation

Each of the three sets used in this study was comprise of three sizes of concrete specimens:

- 3in. x 3in. x 11.25in. prisms used for Weight change measurements and expansion measurements. The prisms were each equipped with one steel gage stud at each end to monitor the length change of the specimens periodically, instead of the drilled cores suggested by the Duggan Method.
- 4in. x 8in. concrete cylinders were used for compressive strength-testing. Samples used for scanning electron microscope (SEM) were taken from specimen used for compressive strength-testing after they were broken.
- 2in. x 2in. concrete cylinders were used for Neutron and X-ray computed tomography (NeXT). Polystyrene, Barium titanate and stainless-steel Microsphere standards were embedded in each 2in x 2in cylinder at various heights to serve as gray scale reference for tomography images. The table below provides the location and number of microspheres used.

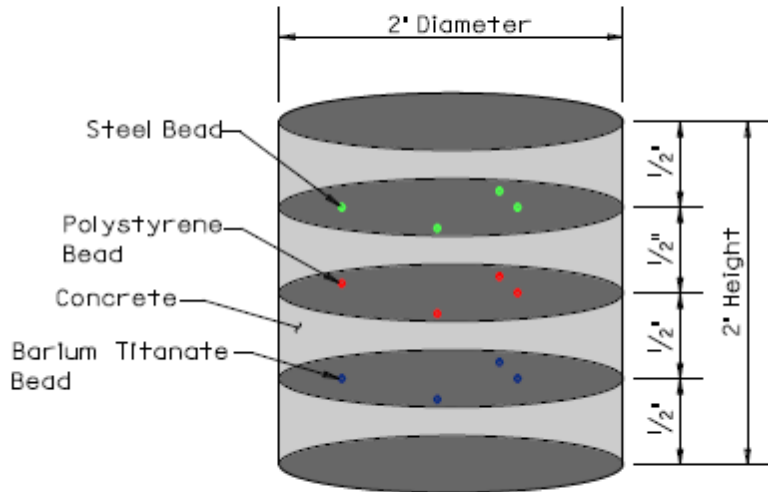


Figure 5-1: Approximate Location of Calibration Standard in a 2in. x 2in. Concrete Cylinders

Table 5-1: Distribution of Microsphere Calibration Standards in 2in. x 2in. Concrete Cylinders

Layer height (in)		Number of microspheres			Material	Diameter (mm)
		Set 1	Set 2	Set 3		
H1	0.5	5	5	5	Polystyrene	1.95
H2	1.0	5	5	6	Barium	0.85
H3	1.5	8	9	9	Stainless	0.88

The samples were prepared in accordance with ASTM C192-16 Standard Practice for Making and Curing Concrete Test Specimen in the laboratory. The concrete mix was proportioned using the Absolute Volume Method. The batch used for Set 2 had potassium carbonate added to the mixing water as to obtain a total potassium content of 1.72% by weight of cement while the concrete batch used for sets 1 and 3 had no added potassium and its potassium content based on potassium content of the cement used estimated at 0.79%. The Water to cement ratio for concrete used in this project was 0.5 for the batch with no added potassium but it was increased to 0.55 for the batch with added potassium

in order to improve workability. Table 5-2 below provides the mass composition of the concrete mix for one (01) cubic yard of concrete and Table 5-3 summarizes the number of specimens fabricated from each concrete batch.

Table 5-2: Concrete Mix Design for 1 Cubic Yard

<b>Constituent</b>	<b>Weight (lb)</b>
<b>Cement</b>	770
<b>Coarse aggregate</b>	1490
<b>Sand</b>	1172
<b>Water</b>	385/423.5 (for batch with added potassium)

Table 5-3: Test Matrix for the Experiment

	Specimen size	Batch 1		Batch 2
		Set 1	Set 3	Set 2
Expansion and Weight	3"x3"x11.25"	5	5	5
Compression Test & SEM-	4"x8"	15	15	15
Tomography	2"x2"	2	2	2
Total		22	22	22

Motor oil was spread inside the molds with a sponge to help the de-molding process. The materials were proportioned in buckets using a mechanical scale and the potassium carbonate was measured on a digital metric scale and dissolved in the water used for the high potassium batch. A rotating mixer with a capacity of 3.0 cubic feet was used to mix the concrete. After the concrete mix was prepared, it was poured into the molds.

- In 4in. x 8in. cylinder molds, the concrete mix was poured in two layers, rodding each layer 25 times and tapping the cylinders against the floor after each layer.

- The 3in. x 3in. x 11.25in. prisms were also tapped against the floor as the mixture was poured.
- In the 2in. x 2in. cylinder molds, concrete was poured in four layers of approximately half inch each, rodding each layer 25 times. After rodding each layer, a certain number of microsphere standard of specific type was placed randomly on top of the layer before pouring the next layer (Figure 5-1).

Once this was complete, the specimens were struck off to obtain a finished smooth surface and either covered with aluminum foil (prisms) or with a lid (cylinders) to prevent drying and shrinkage.

After casting, all concrete specimens were cured in a moist room at 75°F for 24 hours before demolding. The specimens were then subjected to two different treatments:

- Continuous curing in the moist room at 75°F for control specimens (set 3)
- Heat treatment for the two other set: Set 1(No added potassium) and set 2 (with added potassium).

### 5.2.2. Heat Treatment

#### a) Introduction

Heat treatment during curing of concrete has been shown to be one of the main factors leading factor to delayed ettringite formation. The main objective of the heat treatment during this study was to initiate cracks and promote the formation of ettringite in specimens. The literature review provides various cycles commonly used for the heat treatment of concrete specimens in research.

## b) Overview of Different Thermal Cycling Approaches

Numerous heat treatments can be found in the literature review to accelerate formation of secondary ettringite in concrete. All those heat cycles were suggested in an effort to develop a standardized test method to assess the potential for DEF in laboratory concrete samples. They include the Duggan, the Fu and the Kelham cycles as well as some lesser known methods.

### - The Duggan Cycle (1986)

Presented by Duggan in 1986, it is one of the first heat cycles to be extensively used. The method uses concrete cores taken from a structure or from laboratory-cast prisms or cylinders, which are subjected to a series of three successive heating-cooling cycles (Figure 5-2).

- For the first cycle, after curing for 3 days, the cores are placed in a dry-air oven at 180°F for one day, after which they are removed from the oven, allowed to cool for 1 hour, and placed in distilled water for 1 day.
- A second 1-day heating, 1-day soaking cycle is performed.
- A third cycle is performed, but this time the cores are left in the oven at 180°F for 3 days. At the end of the third heating cycle, the cores are removed from the oven and allowed to cool for 1 hour and then measured.

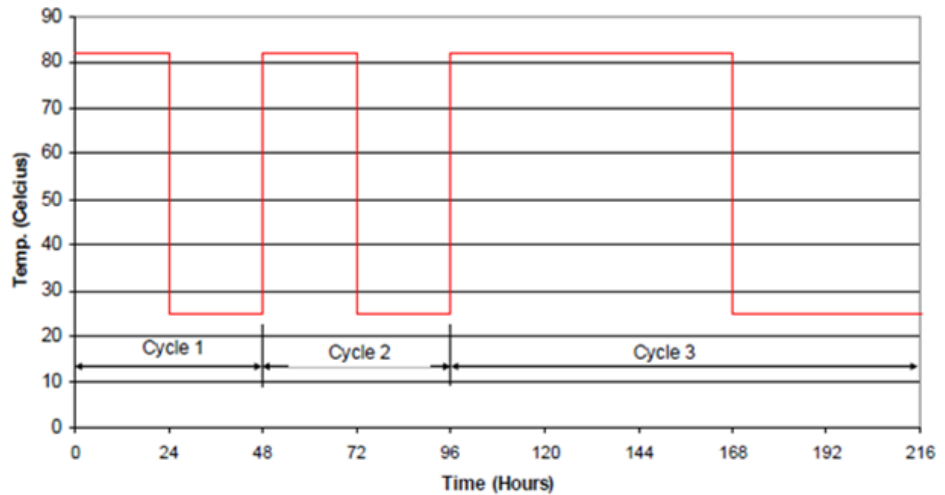


Figure 5-2: Duggan Heat Cycle for Mortar and Concrete Samples

The Duggan heat cycle has been widely criticized within the scientific community. The biggest drawback is that the heating cycles do not represent practical heating regimes (Lawrence, 1995). Other researchers argue that the heating cycle is too severe and may lead to damage even with concrete known to have good performance in practice. The severe heat cycle may cause microcracking of the concrete and ettringite found is just opportunistically formed due to faster penetration of water and increased number of nucleation sites. Another critique suggests that the severe heat cycles induce modifications of the chemical and mechanical properties of concrete (Gillot e Grabowski, 1990). Day (Day, 1992) noted that the results of the Duggan test has not been correlated with field concrete.

- The Fu Cycle (1996)

Fu proposed this method as an improvement to the Duggan method. It is aimed to mimic the heat curing process in precast plants, but it involves and extreme drying event to trigger

cracking into the concrete specimens. It is constituted of two heating-cooling cycles (Figure 5-3).

- The specimens are cured for 1h at 23°C and then subjected to progressive heating until the temperature reaches 95°C in 13 hours, then the specimens are progressively cooled to 23°C in 10 hours.
- For the second cycle, the specimens are suddenly heated to 85°C and maintained at this temperature for 24 hours then rapidly cooled to 23°C and then stored in limewater.

The Fu cycle has faced the same criticism as the Duggan cycle.

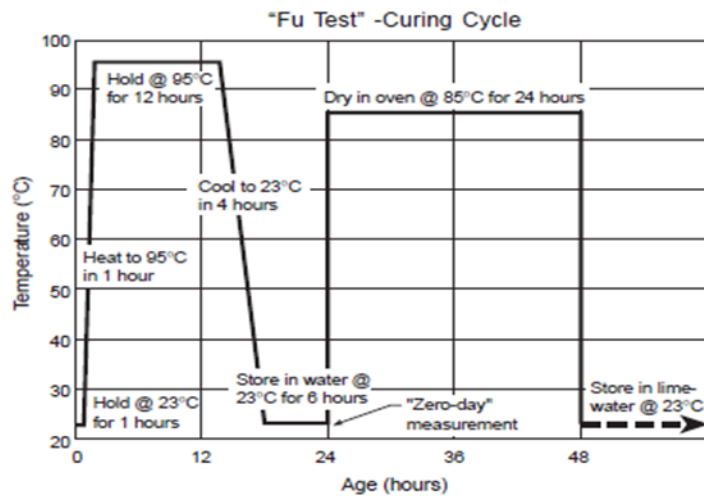


Figure 5-3: Fu Method to Assess DEF (Thomas, Personal Communication, 2000 after Fu 1996)

#### The Kelham Cycle (1995)

Kelham proposed this method as an improvement to both the Duggan and the Fu heat treatments (Day, 1992). It mimics heat curing as practiced in precast plants. It

consists of a single heating-cooling cycle. The specimens are cured for 4 hours at 23°C,

and then progressively heated at a constant rate until the temperature reaches 95°C where they are kept for 12 hours. The specimens are progressively cooled to a temperature of 23°C and then stored in limewater at 23°C (Figure 5-4).

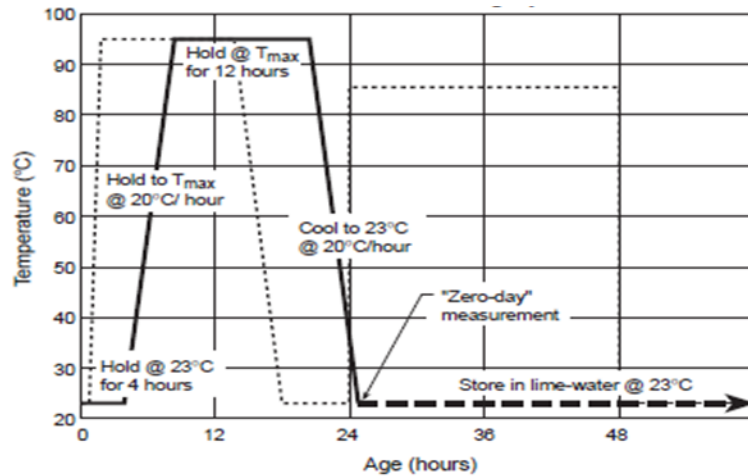


Figure 5-4: Kelham Method to Assess DEF (Thomas, Personal Communication, 2000 after Fu 1996)

- Other Thermal Cycles

Other lesser known methods include the Stark and Bollmann Method (1992) which is more complex and involves multiple freeze thaw cycles with no immersion of specimens and the Lane and Ozyildirim Method (1999) based on the Duggan Cycle but with different heating temperatures.

c) Selection of Heat Treatment to Accelerate Ettringite Formation

In the literature review, it has been observed that there are different test methods. The selection of a suitable test method for this experimental investigation was based on the following requirements:

- The method should be able to produce results within a limited time frame.

- Experimental procedures should be compatible (mimic) with the field condition.
- Clear expansion should occur which can be easily quantified.
- The method should be practicable and adoptable under the available laboratory facilities.

Each of the test methods mentioned in the literature review was considered based on these selection criteria. From the preliminary analysis the Duggan (Duggan e Scott, 1989) and the Fu (Fu e Beaudoin, 1996a) cycles were selected for final evaluation. Based on the test regime it was identified that Duggan cycle has the following advantages over the Fu cycle:

- Short pre-curing time. A short pre-storage period prevents complete consumption of the sulphate and creates the background to trap the available sulphates into the C-S-H phase.
- Quick ramping period. The remaining sulphate, or sulphate from decomposition of the calcium sulphotoaluminate hydrates will be rapidly adsorbed by C-S-H gel forming "phase X" in the cement product when high temperature moist-curing follows.
- Extreme drying cycle. The thermal drying pre-treatment simulates the weathering process that creates microcracks in the cement products after high temperature curing. This treatment is mainly a crack-making process rather than a phase-changing process.

Due to these reasons and practicality, the Duggan cycle was adopted for this experimental investigation.

#### d) Heat Treatment of Concrete Specimens

After demolding, the concrete specimens were stored in the moist room at NRMCA at a temperature of 75°F and 100% RH. All specimens for Set 1 (Normal potassium content) and Set 2 (high potassium content) were subjected to the Duggan heat cycle approximately 3 days after casting. The Duggan Cycle was carried out in the following manner: The specimens were placed in an oven at 82 °C (~180°F) for the first 24 hours. In the second day, the specimens were taken out of the oven and allowed to cool down for one hour and a half before storing them in water for another 24 hours. This process was repeated on the third and fourth day. On the fifth day, the specimens were placed in the oven at 82 °C (~180°F) for the next 72 hours. Once this heating period was over, the specimens were allowed to cool down for the last 48 hours. The initial measurements of expansion (zero readings) and weight change were taken after the completion of this cycle for all specimens, including those that were not heat treated, along with the first tomography scans.



Figure 5-5: Specimens in Oven During Duggan Heat Treatment

### 5.2.3. Storage

After the heat treatment, all the specimens including those that had not undergone the heat treatment (Set 3) were stored in saturated limewater for the whole duration of the study. The 3in. x 3in. x 11.25in. prisms and the 4in. x 8in. cylinders were stored in large basin at NRMCA. 2in. x 2in. specimens designed for tomography were stored in a small container filled with saturated limewater deposited in a safe cabinet at NIST due to concerns regarding irradiation, while the rest of the specimen were stored at NRMCA.



Figure 5-6: Sample Storage in Saturated Limewater

## 5.3. *Material*

### 5.3.1. Cement

The selection of a cement type for this experiment was based on its susceptibility to Delayed Ettringite Formation. Experimental investigation by Fu and Beaudoin (Fu and Beaudoin, 1996b; a) have revealed that Type III Portland cements are the most susceptible

to DEF due to their high content in sulfate, their fine particle size and their higher heat of hydration compare to other types. These results were further confirmed by subsequent works of Famy (Famy *et al.*, 2001) and by Ramlochan (Ceesay, 2007). ESSROC Cement Corp. provided the cement. An X-Ray Fluorescence (XRF) spectroscopy was performed on a small sample of the cement by CTL Group in Skokie, Illinois and it revealed that the cement already contained 0.79% of potassium (K<sub>2</sub>O) by weight. The complete report of the spectroscopy is included in Table 5-4.

Table 5-4: Composition of Type III Portland Cement from XRF Spectroscopy

<u>Analyte</u>	<u>Weight (%)</u>
SiO <sub>2</sub>	19.93
Al <sub>2</sub> O <sub>3</sub>	5.09
Fe <sub>2</sub> O <sub>3</sub>	3.41
CaO	63.00
MgO	2.19
SO <sub>3</sub>	3.46
Na <sub>2</sub> O	0.18
K <sub>2</sub> O	0.79
TiO	0.26
P <sub>2</sub> O <sub>5</sub>	0.09
Mn <sub>2</sub> O <sub>3</sub>	0.16
SrO	0.10
Cr <sub>2</sub> O <sub>3</sub>	0.03
ZnO	0.08
<u>L.O.I. (950°C)</u>	<u>1.12</u>
Total	99.91
T-AIK (Na <sub>2</sub> O + 0.658K <sub>2</sub> O)	0.71

Calculated Compounds per ASTM C150-12 (No Adjustment for possible limestone or inorganic processing additions)

C <sub>3</sub> S	56
C <sub>2</sub> S	15
C <sub>3</sub> A	8

C<sub>4</sub>AF 10

C<sub>3</sub>S+4.75 x C<sub>3</sub>A 93

### 5.3.2. Fine and Coarse Aggregates

The sand and aggregates used in this study conform to ASTM C33 – 16. The sand was York Building Product manufactured sand from Perryville quarry, Perryville, Maryland. It is classified as non-reactive in the Maryland State Highway Administration classification. Table 5-5 contains the technical information of the sand used in the experiment.

The Coarse aggregate was chosen to have a maximum grain size of 1cm, so that we would have a representative concrete sample in the 2in. x 2in. molds. Therefore, the ASTM #8 coarse aggregate was selected with a maximum size of 3/8 in (~0.9.5mm). The coarse aggregate used was provided by Aggregates Industries, Inc. from their Rockville quarry, Rockville, Maryland. It is classified as non-reactive material in the Maryland State Highway Administration classification. Table 5-6 provides the technical information of the coarse aggregate.

Table 5-5: Technical Information of Fine Aggregates

<b>York Building Products, Perryville Quarry, Maryland Natural Sand</b>	
<b>Technical Information Sheet</b>	
Rock Type:	Silica sand
Color:	White to beige
Average gradation	Dry Analysis
ASTM C136	% Passing
3/8 (in)	100
#4	99.4
#8	86.5
#16	59.6
#30	25.0

#50	8.2
#100	0.7
#200	0.2
Specific Gravity (SG)	2.646
Absorption (%)	0.4
Alkali Reactivity of Aggregates (%) (ASTM C1260)	0.02
Soundness (%)	0.8
Unit Weight, Dry Rodded	-
Los Angeles Abrasion (%)	-

Table 5-6: Technical Information of Coarse Aggregates

<b>Aggregates Industries, Inc. Rockville Quarry, ASTM # 8 Stone Technical Information Sheet</b>		
Rock Type:	Carbonate	Calcitic limestone
Color:	Light to Dark gray	
Average gradation	Dry Analysis	
ASTM C136	% Passing	
1 (in)	100	
3/4 (in)	99.4	
1/2 (in)	86.5	
3/8 (in)	59.6	
#4	25.0	
#8	8.2	
Pan	0.7	
Specific Gravity (SG)	2.727	
Absorption (%)	0.4	
Alkali Reactivity of Aggregates (%) (ASTM C1260)	0.01	
Soundness (%)	0.1	
Unit Weight, Dry Rodded	-	

Los Angeles Abrasion (%)	12
--------------------------	----

The coarse aggregate was analyzed by Prompt Gamma Activation Analysis (PGAA) at the NIST NCNR and the results are given in Table 5-7.

Table 5-7: Mass Element Composition of Coarse Aggregates from Prompt Gamma Activation Analysis

Mass Elemental Composition of Coarse Aggregate obtained by PGAA								
Element	Ca	Ca	Mg	Si	Fe	O	Cl	H
Percentage	25%	10%	16%	2%	2%	45%	2.43 ppm	279.96 ppm

Ppm: parts per million

From the information sheet and the mass elemental composition, we concluded that the coarse aggregate was a dolomitic limestone. The elemental composition was also used to determine the attenuation coefficient of the aggregate to be used for phase segmentation.

### 5.3.3. Potassium Carbonate

Anhydrous granular reagent grade potassium carbonate ( $K_2CO_3$ ) was added to the mixing water in order to increase the potassium content. 1.5% Potassium carbonate by weight of cement was added to mixing water for Batch 2. Therefore, the total potassium content of the mix for this batch was estimated at 1.72%.

#### 5.3.4. Internal Calibration Standards: Microspheres

One of the main challenges in analyzing tomographic images for a multiphase material like concrete is the calibration of the grayscale in order to perform segmentation. In order to achieve this, objects with unique shapes and known attenuation factors were inserted into concrete samples used for tomography. The choice was made to use microsphere beads that were inserted into 2in. x 2in. specimens during casting. These microspheres would serve as calibration standards and also, they will be used for beam hardening correction. The microsphere materials were selected as to have their attenuation coefficients span the range of values to be expected in the concrete phases: water, ettringite, calcium hydroxide, quartz and limestone. Therefore, three materials were selected for the microsphere: Polystyrene, Stainless steel and Barium titanate. They were chosen on the basis of attenuation factor, commercial availability and cost. Table 5-8 summarizes the neutron attenuation coefficients for phases typically found in concrete, including quartz and limestone aggregates as well as those of internal standards used in this study. These have been calculated from their elemental compositions using the NIST Neutron Activation and Scattering Calculator, except for the asterisked values which were obtained by experimental measurement on mortar samples (Lucero, Catherine L. *et al.*, 2015). These microspheres of 1mm diameter were placed at known locations during concrete casting (Figure 5-1).

##### a) Polystyrene Microsphere

Polystyrene microspheres were selected because the value of attenuation coefficient of polystyrene polymer ( $4.12 \text{ cm}^{-1}$ ) is comprised between the value of attenuation coefficient

of water ( $3.808 \text{ cm}^{-1}$ ) and the value of attenuation coefficient of ettringite, therefore it can efficiently be used to segment water from ettringite in pore structures.

b) Stainless Steel Microsphere

Stainless steel has an attenuation coefficient value ( $1.18 \text{ cm}^{-1}$ ) between those of the C-S-H gel ( $2.675 \text{ cm}^{-1}$ ) and coarse aggregates ( $0.258 \text{ cm}^{-1}$ ) and thus was used to distinguish each of those phases during segmentation. In addition, due to its density, it has the highest attenuation coefficient to X-ray and was used for beam hardening correction.

c) Barium Titanate Glass

Barium titanate glass has an attenuation coefficient value ( $2.16 \text{ cm}^{-1}$ ) between those of the C-S-H gel ( $2.675 \text{ cm}^{-1}$ ) and coarse aggregates ( $0.258 \text{ cm}^{-1}$ ) and thus was used to distinguish each of those phases during segmentation.

Table 5-8: Attenuation Factors for Phases Found in Concrete for 25 meV Versus 45 keV X-ray Photons

Phase		Neutron Attenuation coefficient* ( $\text{cm}^{-1}$ )	X-ray Attenuation Coefficient ( $\text{cm}^{-1}$ )
Concrete	Water*	$3.808 \pm 0.036$	0.24
	Fine aggregate*	$0.339 \pm 0.002$	0.95
	Dry cement*	$0.369 \pm 0.005$	---
	C-S-H gel*	$2.675 \pm 0.266$	1.75
	Coarse aggregate	0.258	1.81
	Calcium hydroxide	3.193	1.85
Expansive Phases	Ettringite	4.675	0.92
	ASR gel	1.833 - 3.355	---
	Water ice	5.081	0.24

Internal Standards	Stainless steel	1.18	21.04
	Barium titanate glass	2.16	61.44
	Polystyrene	4.12	0.21

\*Neutron Experimental value based on Lucero et al. (2014)

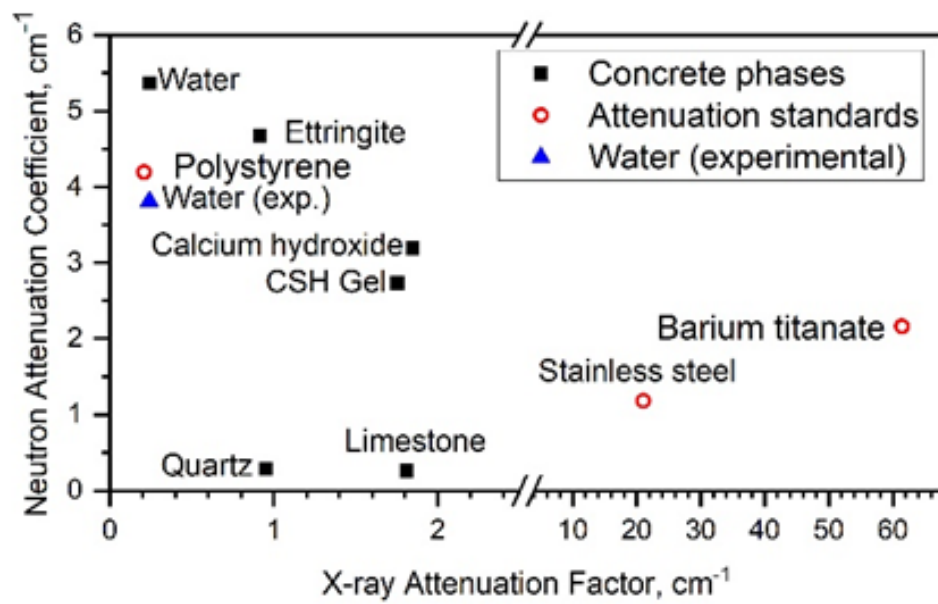


Figure 5-7: Plot of Computed Attenuation Factor for Phases Found in Concrete for 25 meV versus 45 keV X-ray Photons



Figure 5-8: Placement of Polystyrene Microsphere (yellow arrows) During Casting

Figure 5-9: Polystyrene Microsphere Visible (yellow Arrow) in Neutron CT Slice

#### 5.4. Casting and curing of Concrete Specimens

##### 5.4.1. The Molds

Three types of molds were used in this study including standard molds used for conventional macroscopic tests and non-standard molds that we have designed for specimen to be used for tomography.

##### a) For 3in. x 3in. x 11.25in. Prismatic Specimens

For 3in. x 3in. x 11.25in. prisms used both for expansion measurement and weight change measurement, steel molds conforming to ASTM C490 specifications with provisions for stainless steel gage studs and an effective gage length of 10 inches were used.

b) For 4in. x 8in. Cylindrical Specimens

4in. x 8in. PVC cylinder molds conforming to ASTM C470 specifications were used to prepare for the compressive strength-testing specimen.

c) For 2in. x 2in. Cylindrical Specimens

Custom designed 2in. x 2in. PVC cylinders were used for specimen design for tomographic scanning.



Figure 5-10: Overview of 2in. x 2in. Cylinder Molds



Figure 5-11: Steel Prism Molds and 4in. x 8in. PVC Cylinder Molds



Figure 5-12: Steel Gage Studs in Steel Prism Mold and 10in. Rod Spacer

#### 5.4.2. Moist room for Concrete Curing

All specimens were cured as per ASTM C192-16 and ASTM C511-13 in a moist room at NRMCA for 24 hours. The moist room was set to a temperature of 75°F and 100% RH. After the 24 hours, specimens to be heat treated were removed and placed in the oven while the control specimens were left in the moist room until the initial expansion measurements were made. After the initial measurements were made, all the specimens were stored in saturated lime water for the rest of the experiment.

### 5.5. *Computed Tomography Specimens Mounting*

Prior to scanning, CT specimens required additional preparation: they were glued on steel base plates using an epoxy resin and wrapped in Teflon film before they were mounted on the stage.

#### 5.5.1. Stainless Steel Base Plates

Concrete cylinders used for tomography imaging were fastened to stainless steel base plates (Figure 5-13). The base plates had two main purposes:

- They had threaded rods that screw into the CT stage for accurate alignment.
- They also had notches milled on the edges at different distances to provide fiducial marks that were used during image registration for accurate registration of reconstructed 3-D tomograms from scans at different times.

The concrete specimens were glued to the stainless-steel base plates after demolding and heat treatment using an epoxy adhesive. they remained attached to the base until the end of the study. The stainless-steel material was chosen to prevent rusting of the plates during storage in limewater.

#### 5.5.2. Epoxy Adhesive

A two-part marine grade epoxy adhesive was used to glue the concrete cylinders to the stainless-steel base plates (Figure 5-13). This type of adhesive was selected for its heat resistance (with a temperature range between -20°F and 200°F) and its high stability to acid, alkaline and caustics.

#### 5.5.3. Teflon Film

Teflon film which is the brand name for PTFE (polytetrafluoroethylene) was used to seal the concrete samples during scanning (Figure 5-14) in order to prevent changing levels of pore water content due to evaporation. In fact, our preliminary investigation had shown that the sample loses water during scanning due to heat generated by the impact of neutron beam on the sample. The Teflon film was chosen because of its low density ( $2.2\text{g/ cm}^3$ ) which rendered it invisible to the X-ray and its low neutron attenuation coefficient ( $0.295\text{ cm}^{-1}$ ) which renders it invisible to the neutron beam. It's resistance to heat (melting point at  $327^\circ\text{C}$ ) made it a good candidate for our study. A 20-mils Teflon film was used.

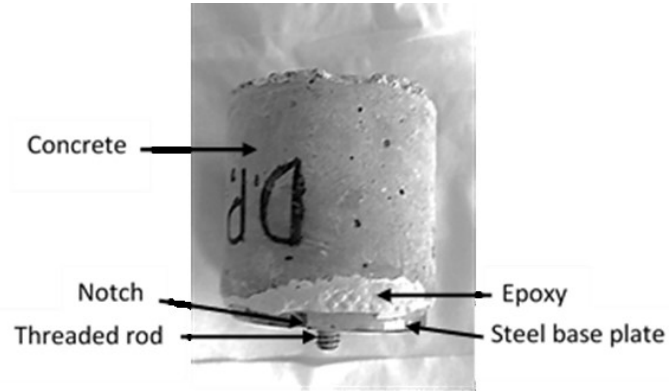


Figure 5-13: 2in. x 2in. Concrete Cylinder on Steel Base Plate



Figure 5-14: 2in. x 2in. Concrete Cylinder Wrapped in Teflon Film Ready for Scanning



Figure 5-15: Location of Notches on Steel Base Plates

## Chapter 6 : Conventional Tests Procedures

### 6.1. Introduction

Conventional tests included those aiming at characterizing the specimens at the macroscopic scale (expansion and weight change measurements, compressive strength test) as well as the microscopic level (Scanning Electron Microscopy with Energy Dispersive X-ray). The frequency of each test was determined to monitor the evolution of DEF in the samples and associated damages over time. Table 6-1 provides a snapshot of the frequency of various tests.

Table 6-1: Tests Frequencies

Test	Expansion Measurement	Weight change	Compressive strength test	SEM and EDAX	NeXT
Frequency	Every 2 days until appearance of surface cracks, 5 days afterward	Same as expansion measurement	9,40,83,120, 337 days	Same as for compressive strength test	9,39,66,102,148, 230 days

### 6.2. Expansion Measurement

Expansion measurements were taken in accordance with ASTM C 157-14 Standard Test Method for Length change of Hardened Mortar and Concrete with a digital comparator accurate to + 0.0001 inches and a reference 10 –inch invar bar. Initial length change measurements were recorded immediately after the completion of the Duggan Heat treatment and before storing the specimen in saturated limewater. Five 3in. x 3in. x 11.25in. prisms from each set were used to measure the length-change at intervals of 2 to 5 days. The measurements were recorded, then the expansion of each prism calculated, and the average expansion of each set calculated. The expansion measurements were made after the specimens were taken out of the water and the excess water was removed with a towel.

An arrow mark was made on one end of each prism indicating the “up” direction and all prisms were always measured with the marked positioned up as required by ASTM C490-16 for accurately obtaining comparator readings. All length-change measurements were done in a 75°F room. Figure 4.6 shows a concrete prism positioned to measure the length change with a digital comparator.



Figure 6-1: Comparator Set Up for Expansion Measurement

The expansion of a concrete specimen was determined using the following formula:

$$\Delta L = \frac{L_x - L_i}{G} \times 100\% \quad \text{Eq. 10}$$

Where,

$\Delta L$  : Length change of the specimen at any age in %

$L_x$  : Comparator reading of specimen at  $x$  age minus comparator reading of reference bar at age  $x$  days, inches

$L_i$  : Initial comparator reading of specimen minus comparator reading of reference bar at that same time, inches

$G$ : Nominal Gage length of 10 inches

### 6.3. Weight Change Measurement

Weight change measurements were done on 3in. x 3in. x 11.25in. prisms after they were measured for expansion. The specimens were blotted surface dry by wiping with an absorbent paper towel until all visible films of water were removed, then measured for expansion and immediately weighed. The same five prisms used for expansion measurement were used for weight change in each set. A digital weighing scale accurate to 0.1 grams was used for the weight change measurement. The measurements were recorded, the weight-change of each prism calculated and then the average weight change of each set calculated. Figure 6-2 shows a concrete prism positioned for weight measurement with a digital scale.



Figure 6-2: Concrete Specimen Positioned for Weight Measurement on a Digital Scale

The weight changes of the specimens were calculated in percentages using the equation below:

$$\Delta W = \frac{W_x - W_i}{W_i} \times 100\% \quad \text{Eq. 11}$$

Where,

$\Delta W$  : Weight change of the specimen at any age in %

$W_x$  : Weight of specimen at age x.

$W_i$ : Initial weight of specimen (at age 0 days)

#### 6.4. Compressive Strength

Compressive strength test was performed in order to access the impact of DEF on the compressive strength of concrete as ettringite is formed in concrete over time. Three 4in.

x 8in concrete cylinders from each set were tested at each stage of the study corresponding to the frequency of tomographic scans (see Table 6-1 for test frequencies). Compression strength tests were performed in accordance with ASTM C39-16 Standard Test Method for Compressive Strength of Cylindrical Concrete Specimens. Three 4in x 8in cylinders from each set were tested at each stage. The compressive strength reported is the average compressive strength. A machine with a 1,000,000 lbs capacity was used. The specimens were removed from the limewater, dried off with a paper towel, and measured before testing them at a load rate of approximately 25,000 lb/min. The first compression tests were performed immediately after the completion of the Duggan Heat treatment and before storing the specimen in saturated limewater.



Figure 6-4: Compression Testing of a Concrete Cylinder



Figure 6-3: Compressive Test Machine Used

6.5. Scanning Electron Microscopy (SEM) and Energy Dispersive X-ray Analysis (EDAX)

6.5.1. Introduction and Background

There are many visual techniques used in the literature to identify material present in cracks, voids and cavities of concrete in order to determine the failure mechanism. They include petrographic analysis, scanning electron microscope which is sometimes coupled with Energy Dispersive Analyzer X-ray (EDAX), the differential scanning calorimeter, and the quantitative x-ray diffraction. Scanning electron microscopy was used in this study to confirm and validate findings made with the neutron and x-ray tomography. SEM-EDAX has been the tool of choice of many researchers when they want to differentiate expansive phases in concrete and cementitious material (Marusin, 1993; 1994; Hime, 1996; Ceary, 2007; Ceesay, 2007).

6.5.2. Principle of SEM – EDAX

A high-energy electron beam is scan across the surface of a specimen. From the interaction between the neutron beam and the surface of the specimen, three main signals are produced: backscattered electrons, secondary electrons and X-rays. Analysis of those three signals allow for characterization of the specimen.

Backscattered electrons are high-energy electrons (>50eV) that have undergone multiple scattering event within the specimen. The backscattered electron image contrast is generated by the different phases' compositions relative to their average atomic number. The electron micrographs obtained by using high-energy backscattered electrons reflect

differences in the atomic numbers and can distinguish among the particles based on the variation in brightness of the topography image of the specimen.

Secondary electrons are low energy electrons that result from inelastic collision of the primary electron beam with electrons of the specimen material. Since they are low in energy, they are mostly absorbed by the specimen and only those produced near the surface escape. The electron micrographs that are obtained by using low energy secondary electrons are capable of showing the morphology of the microstructure in two or three dimensions and the surface topography of the specimen.

X-rays produced by the interaction of the high-energy neutron beam and the specimen are used to perform microanalysis of the specimen. X-rays are captured with an energy dissipative detector. The X-ray signal can be used for spectrum analysis to determine the presence and concentration of chemical elements in the specimen, to display the concentration change along a line or the element spatial distribution and relative concentrations to allow phase identification.

### 6.5.3. Sample Preparation for SEM and EDAX

Sample preparation for SEM is an important step and depends on the intended use. For the study of failure mechanisms, two methods are commonly used:

The fracture surface method is sometimes used for specimens to be examined by secondary electron imaging because of the high degree of resolution and depth of field obtained with this imaging technique. This method has the advantage that it does not require further treatment other than drying and coating the specimen. Thus, whatever is seen on the fractured surface is not altered by other treatments. However, information about the

composition of deposits found on a fracture surface must be considered qualitative; quantification requires the use of supplemental methods such as X-ray diffraction or wet chemistry. Another limit of the method is that fractured surfaces do not represent the material as a whole, but only its weakest surface. This method has been used extensively in the diagnosis for DEF distress mechanism in concrete and mortar (Oberholster *et al.*, 1992; Marusin, 1995) (Ceesay *et al.*, 2007; Amde, 2004; Amde *et al.*, 2005; Amde *et al.*, 2003).

The flat polished surface method is the only one suited for backscattered electron imaging. With this method, the specimen is saw-cut as to produce a surface with the least amount of deformation and polished with successively finer silicon-carbide grit to obtain a smooth surface. This method is the most commonly used method (Shayan, 1995; Stutzman, 2001).

Regardless of the method used, the sample is coated with a thin layer of electrically conductive material to prevent the accumulation of electrical charge on the surface. The usual choices are carbon or gold.

#### 6.5.4. SEM and EDAX Experiment

Scanning Electron Microscopy (SEM) with Energy Dispersive X-ray analysis (EDAX) were done at the FabLab of the NanoCenter of the University of Maryland, College park. We used the Hitachi S-3400 variable Pressure SEM scanner that allows scanning of conductive and non-conductive samples and is fitted with an EDAX analyzer for determining elemental composition of samples.

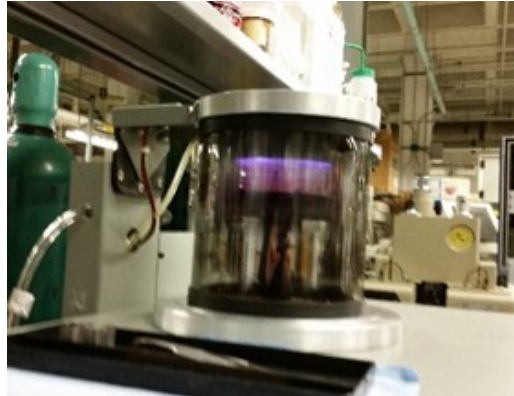
The method of fracture sample was used because it is excellent for showing crystals of DEF in paste or at aggregate particle-paste interfaces. In addition, when used in

combination with EDAX, SEM of fracture samples can allow for quantification of material phases. Pieces of concrete were taken from each of the cylinder after they were broken for compressive strength. Each piece was broken into smaller pieces with a five-pound sledgehammer, and a sample is selected which has a relatively flat side to allow mounting. The sample selection was done in such a way that the flat side had been in contact with an aggregate, this in order to visualize the interfacial transition zone (ITZ). Once the samples were selected, they were dried in an oven at 70°F for 24 hours. After drying, the samples were mounted onto sample holders. In the final step, some of the samples were coated with carbon to make them conductive and prevent accumulation of electric charge on their surface, which will interact with the incoming neutron beam and corrupt the image obtain. Samples that were not coated were scanned in backscatter mode with variable pressure (in order to have a clear visual image of the surface and avoid electron charge buildup on the sample) while samples that were coated were scanned in direct mode at high pressure (High vacuum). The sample and sample holder were placed into a vacuum chamber, in which the pressure was lowered to 0.100 torr (1 torr = 1 millimeter of mercury or 133.32 pascal). At this pressure, the carbon coating was applied. After the coating, the sample was ready to be analyzed.



(a)

(b)



(c)

Figure 6-5: SEM and EDAX Sample Preparation: (a) Drying, (b) Mounting of Sample Holder, (c) Carbon Coating

The sample assembly was set into the SEM with the top surface at approximately 10 mm to the detector to produce the maximum possible signal for the EDAX analysis process. The ITZ was then map analyzed and some spots deemed of interest were also analyzed.

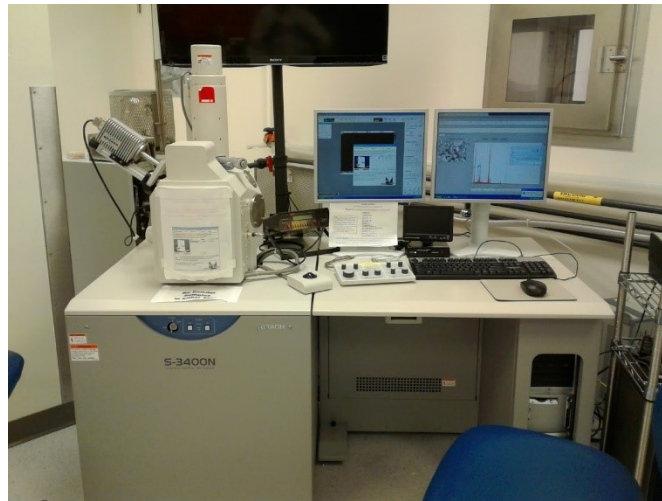


Figure 6-6: Hitachi S-3400 Variable Pressure SEM Scanner

## Chapter 7 : Simultaneous Neutron and X-ray Tomography: Experimental Approach

### 7.1- Introduction

The experimental approach used for simultaneous neutron and X-ray imaging is herein described in this chapter. It involves simultaneously scanning the sample with a neutron and an X-ray beam from different directions, collecting the radiographs that are then processed to obtain 3D representations of the specimen. The flowchart of Figure 7-1 is a synopsis and chronology of the various operations performed.

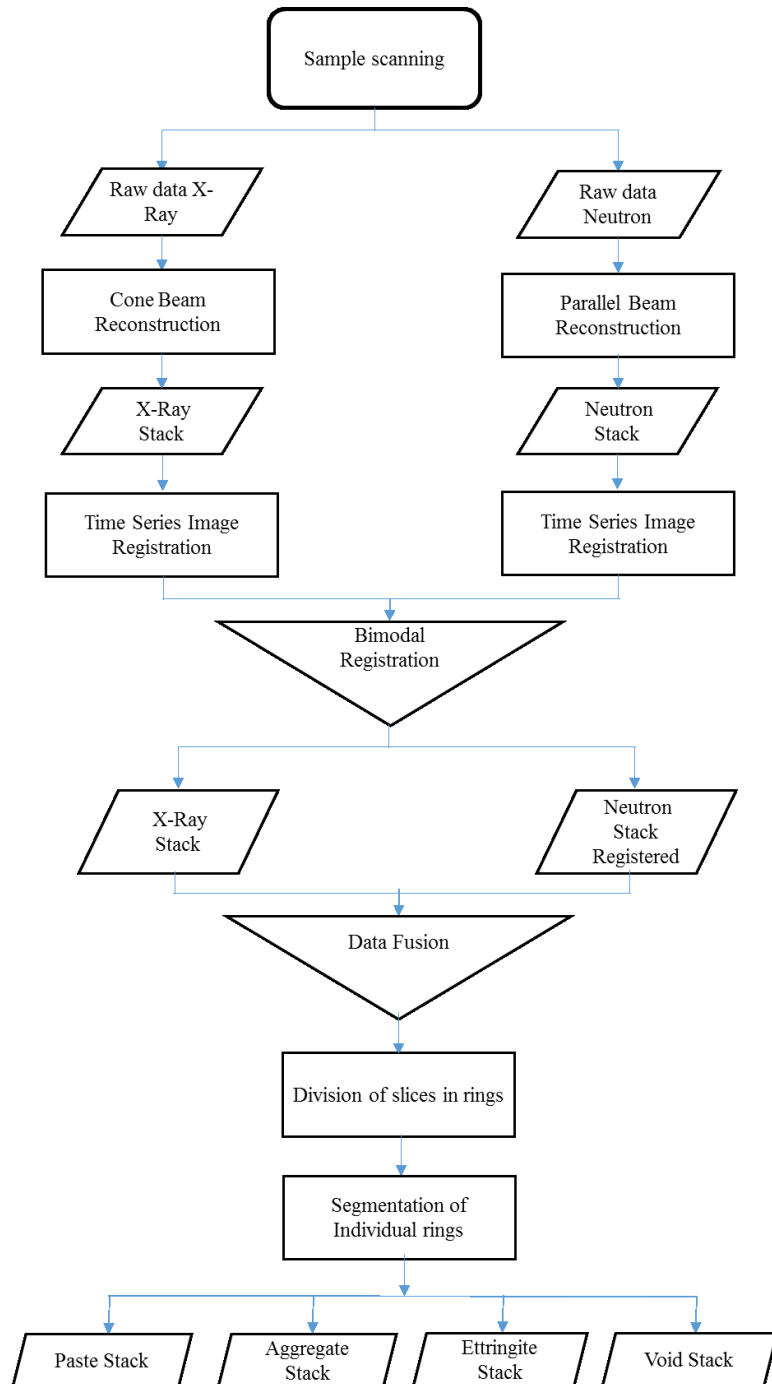


Figure 7-1: Flowchart of Different Steps for Simultaneous Neutron and X-ray Imaging

7.2- Overview of the NeXT Facility at NIST

Imaging was performed at the Neutron Imaging Facility (NIF) of the NIST Center for Neutron Research (NCNR) at the National Institute of Standards and Technology in

Gaithersburg, MD. The NIF is located on the beam tube 2 (BT2) thermal neutron port of the NCNR. (Figure 7-2 and Figure 7-3)

#### 7.2.1. The Neutron Imaging System

A schematic of the engineering model of the NeXT is shown in Figure 7-4. The neutron beam is produced from a 20 MW nuclear fission reactor. Neutrons exiting the reactor pass through a series of ring of progressively diminishing internal diameter and produce a conical beam with almost uniform intensity (Lamanna *et al.*, 2017). The neutron beam can be assimilated to a parallel beam when it reaches the sample to be scanned (Figure 8-7). The main components for neutron imaging consist of the thermal neutron beam and the neutron detector, which combines a neutron-to-light converter screen with a CCD camera. The object to be imaged is placed in front of the beam before the camera. The neutrons passing through the object are attenuated by local variations in materials properties. For computed tomography, multiple images are taken as the object is rotated in the beam and a 3-D image is then reconstructed from the individual images.

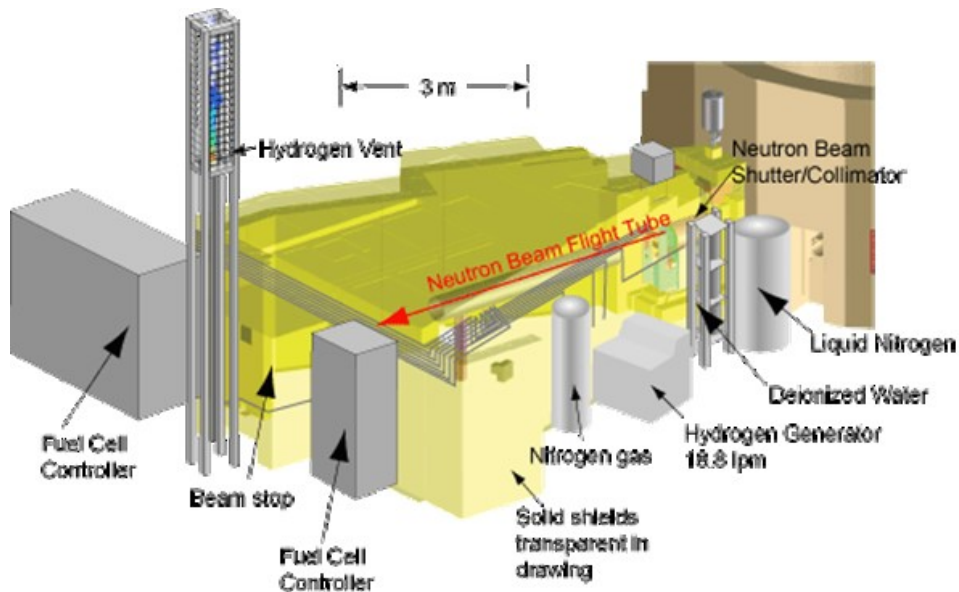


Figure 7-2: Perspective View of the Thermal Neutron Facility at NIST in Gaithersburg

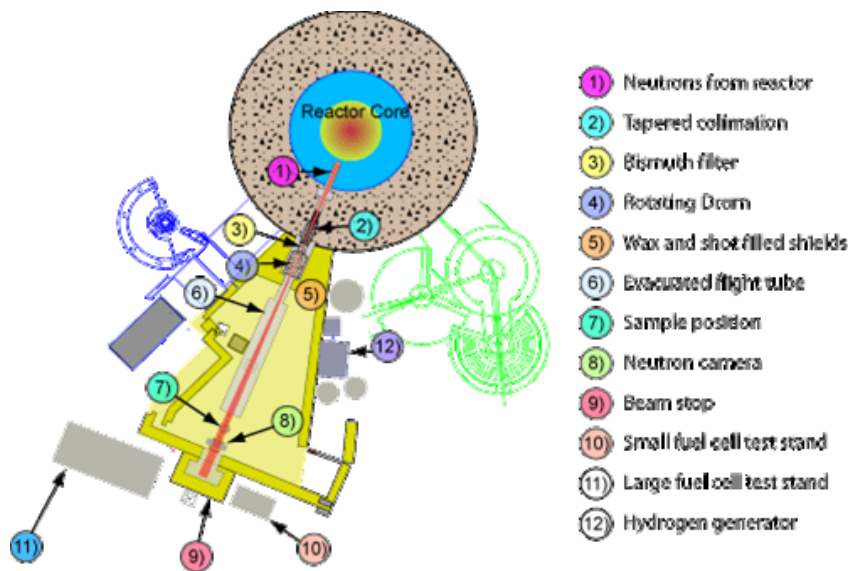


Figure 7-3: Plan View of the Thermal Neutron Facility of NIST in Gaithersburg

### 7.2.2. X-Ray Imaging System

The X-ray imaging system consists mainly of an X-ray source and an X-ray camera. The X-ray generator is an Oxford Instruments Ultra Bright micro focus X-ray generator that produces a cone beam with an angle approximately  $35^\circ$  (Figure 8-8). The generator

operates at voltages from 20 kV to 90 kV and a maximum current of 2 mA. As for the neutron imaging system, multiple images are taken as the object is rotated in the beam and a 3-D image is then reconstructed from the individual images.

The specimen to be scanned is placed on a sample stage located at the intersection of the neutron and the X-ray beams (Figure 7-4). The sample stage is designed as to allow 6-axis motion. A software for data acquisition developed by NIST was used for the simultaneous control of both cameras and the 6-axis sample motion control system to maintain time correlation between imaging modes.

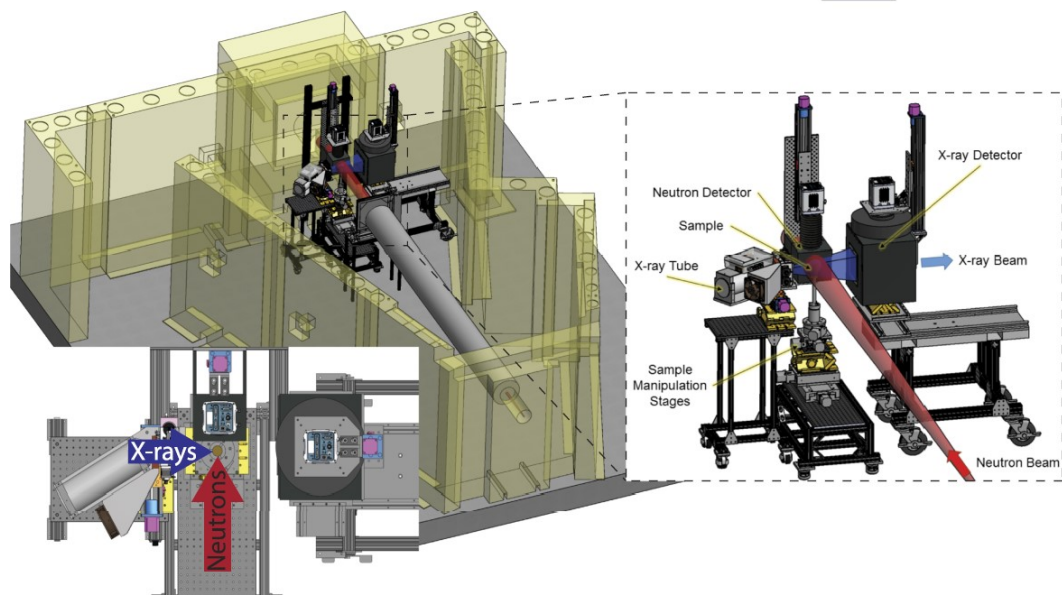


Figure 7-4: Engineering Model Representation of the NeXT System at NIST with the Neutron Beam in Red and the X-ray Beam in Blue (Source: LaManna (Lamanna *et al.*, 2017) )

### 7.3- Sample Scanning

#### a) Operating Parameters

Each 2in. x 2in. cylinder sample was scanned at the frequency shown in Table 6-1. Each time, the equipment had the same settings. The neutron beam had an aperture diameter of 15 mm, a collimation ratio of 400 and a fluence rate of  $1.7 \times 10^7 \text{ cm}^{-2}\text{s}^{-1}$  for a beam diameter of 26 cm. The field of view of the neutron detector was 77 mm by 65 mm for a pixel pitch of 30  $\mu\text{m}$ . The X-ray generator operated at 90 KeV peak energy and the X-ray detector field of view was 131 mm by 111 mm for a pixel pitch of 51.4  $\mu\text{m}$ . Table 7-1 below summarizes the imaging parameters for the Neutron and X-ray systems while Table 8-1 provides information on the tomographic stacks obtained after reconstruction. The data acquisition was managed using the software platform Andor Solis. The stage was set up to scan the core over  $360^\circ$  in  $0.359^\circ$  steps.

Table 7-1: NeXT Operating Parameters

<u>Neutron System</u>	<u>X-ray System</u>
Energy= 25 meV	Energy = 90 KeV Max. 32 KeV Average
Aperture: D=15 mm	Field of View: 131 mm x 111 mm
Collimation ratio: L/D=400	Beam Geometry: Cone
Fluence Rate = $1.7 \times 10^7 \text{ cm}^2\text{s}^{-1}$	Pixel Pitch = 51.4 $\mu\text{m}$
Beam Geometry: Parallel	
Beam Diameter = 26 cm	
Field of View; 77 mm x 65 mm	
Pixel Pitch = 30 $\mu\text{m}$	
<u>Image Capture</u>	
Sample Rotation step = $0.359^\circ$	Range: $360^\circ$
Acquisition time:: ~10 sec/ image	Number of Images per step: 3
Total Acquisition Time: ~8.5 hours	

b) Image Acquisition

The specimen was rotated through  $360^\circ$  in  $0.359^\circ$  steps and at each step, simultaneous neutron and X-ray radiographs were taken. Three images were acquired at each step with an acquisition time of 10 seconds. Consequently, the total time for each core was approximately 8.5 hours. In addition, 30 flat field images (projection images of the field of view without sample acquired with the beam turned on) and 30 dark field images (projection images of the field of view without sample acquired with the beam turned off) were taken. The flat and dark field images would be used to normalize the images, i.e. to

correct for the variations in the pixel-to-pixel sensitivity of the detector and/or by distortions in the optical path.

## Chapter 8 : Computed Tomography Image Preprocessing, Reconstruction and Post processing

### 8.1- Introduction

The raw data collected from scanning the specimens were series of radiographs (Projections of the specimen) taken at different angle steps that needed to be preprocessed in order to eliminate outliers, reduce noises and correct for the distortion induced either by the hardware or misalignment. Upon preprocessing of radiographs, the horizontal slices were reconstructed.

### 8.2- Image Preprocessing

The raw images captured during scanning of the specimens were preprocessed prior to reconstruction of the tomographic images (Figure 8-1 and 8-2). The preprocessing of X-Ray and Neutron images was done using the NIFProg\_VER04 software package designed by NIST. Both X-ray and neutron data were processed in the following steps: combination, deconvolution and barrel distortion correction (for the Neutron images only).

#### 8.2.1. Image Combination

To eliminate outliers, the three (03) images taken at each angular step were combined with a median filter. The thirty flat field images (open beam) and thirty dark field images (closed beam) images were also combined in the same manner with a median filter so that there were 10 flat field and 10 dark field combined images obtained. The use of a median filter in time eliminated the appearance of streaks due to gamma rays and fast neutrons depositing energy.

### 8.2.2. Image Deconvolution

There are at least four (04) reasons for image degradation during image acquisition: noise, scatter, glare, and blur. While noise, scatter and glare are random disturbance of light, blur is a nonrandom spreading of light that occurs by passage through the imaging system optical train. The blur in the images acquired during scanning of the specimen is induced by the limited aperture of the camera and is due to diffraction and aberration in the optical path. The principal objective of deconvolution is to remove this out-of-focus blurring from the images.

After combining the images, they were deconvolved using the Fast Fourier Transform (FFT). The resulting image was the true image convoluted with the point spread function (PSF) plus noise (Hussey *et al.*, 2013). By deconvolving the images, they are transformed back to the spatial domain from the frequency domain. The noise, the scatter and the glare were removed during subsequent processing stages.

### 8.2.3. Correction of Optical Distortion

An optical distortion is generally referred to an optical aberration that deforms and bends physically straight lines and makes them appear curvy in images. Optical distortion occurs as a result of optical design, it is a lens error. When using a lens for a large field of view like it is the case in this study, there is a barrel distortion in the obtained image, which means that lines appear curved inwards. Barrel distortion results in a curved image plane, most pronounced at the edges of the image, it's quadratic in the displacement from the center of the image.

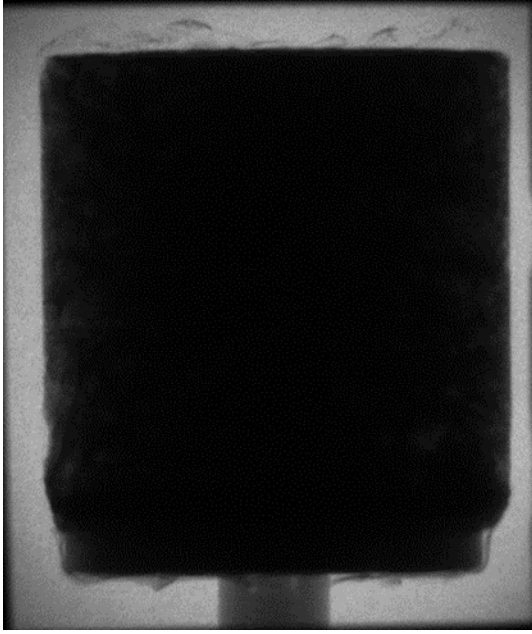


Figure 8-1: X-ray Radiograph of a Concrete Specimen



Figure 8-2: Neutron Radiograph of a Concrete Specimen

### 8.3- Volume Reconstruction

Image reconstruction refers to the mathematical process that generates tomographic images from the projection (radiographs) acquired at all the different angle steps. Through this operation, a 3-D reconstruction of the specimen is obtained. In practice, to reduce the amount of computational resources required, the volume was sectioned into a vertical stack of 2-D slices one pixel thick for further analysis. Thus there were separate stack for X-ray and neutron scans. Image reconstruction was performed with the computed tomography software OCTOPUS<sup>®</sup>. The various steps in the reconstruction process included: Normalization, construction of sinograms filtering and reconstruction of tomographic slices.

- Image Normalization.

It is a process that changes the range of pixel intensity values of the image. The normalization involved also subtraction of the dark field images (Figure 8-3) and flat field (Figure 8-4) correction. Subtraction of the dark field image was aimed to minimize noise. This is an important step for imaging techniques with long exposure time to thermal radiations like thermal neutron or X-ray (Exposure time of ~15hours). One of the components of noise called fixed-pattern noise is the same from shot to shot and subtracting the flat field images helps reduce this component. The goal of flat field correction was to remove artifacts that are caused by the variations in pixel-to-pixel sensitivity of the detector or by distortions in the optical path. All neutron and X-ray data were normalized.

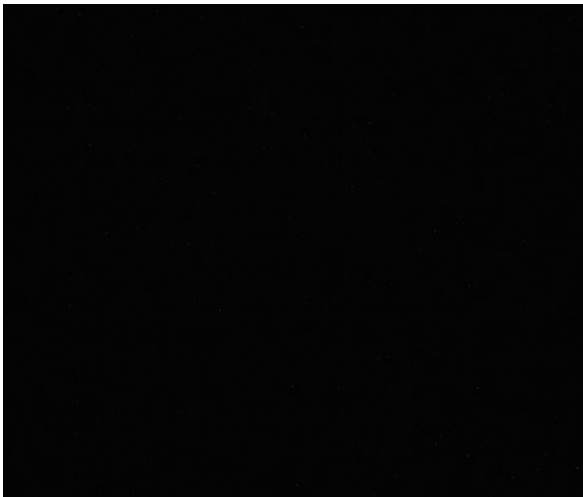


Figure 8-3: Example Neutron Dark-Field Image

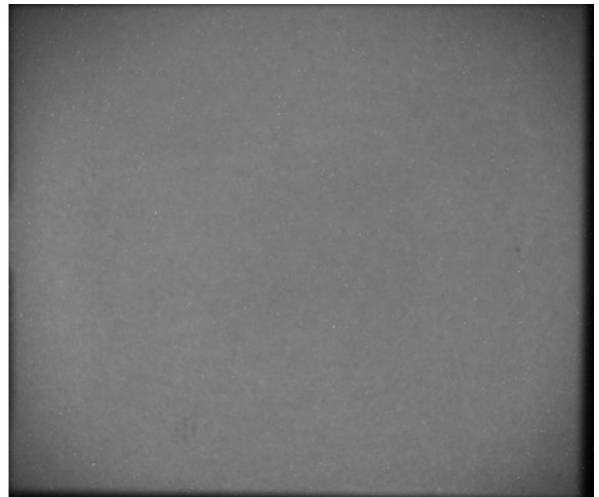


Figure 8-4: Example Neutron Flat-Field Image

- Construction of Sinograms

Construction of sinograms also called radon transform is one of the most important steps of the reconstruction process. Sinograms are 2-D array containing the projections. Each row on a sinogram is a projection along the corresponding angle on the vertical axis. To build a sinogram, all projections are stacked and the points that belong to the same slice

are extracted from each projection and grouped into the sinogram. The process is repeated for each slice. Therefore, there are as many sinograms as there are slices.

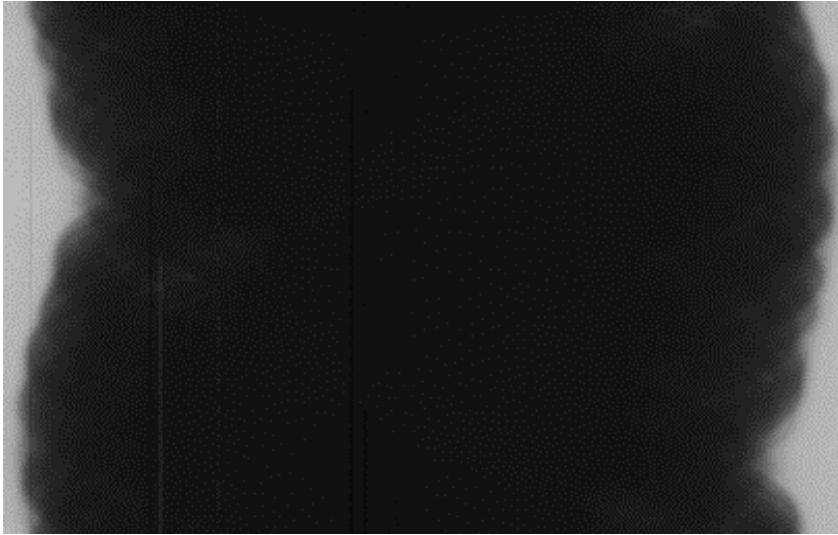


Figure 8-5: Neutron Sinogram for DP1-2-6

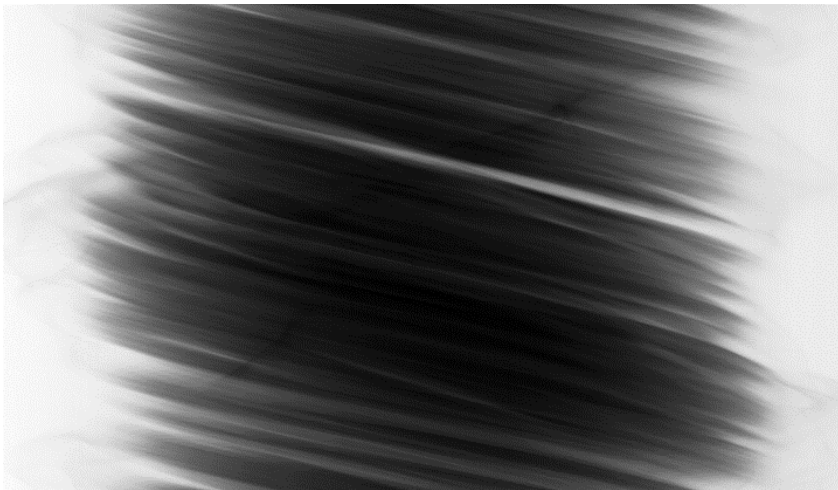


Figure 8-6: X-ray Sinogram for DP1-2-6

- Tomographic Slices Reconstruction

Based on the geometry of the radiation beam used to scan the specimens, two different method of reconstruction were used:

- Parallel Beam Reconstruction for Neutron Data

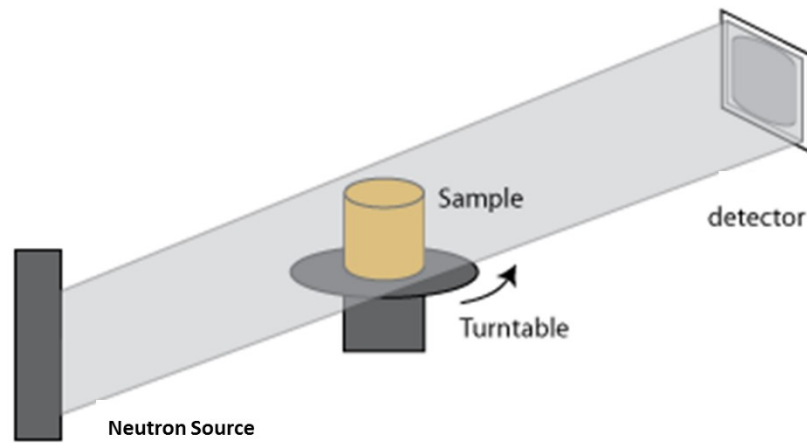


Figure 8-7: Quasi- Parallel Beam Configuration for Neutron Imaging

- Cone Beam Reconstruction for X-ray Data

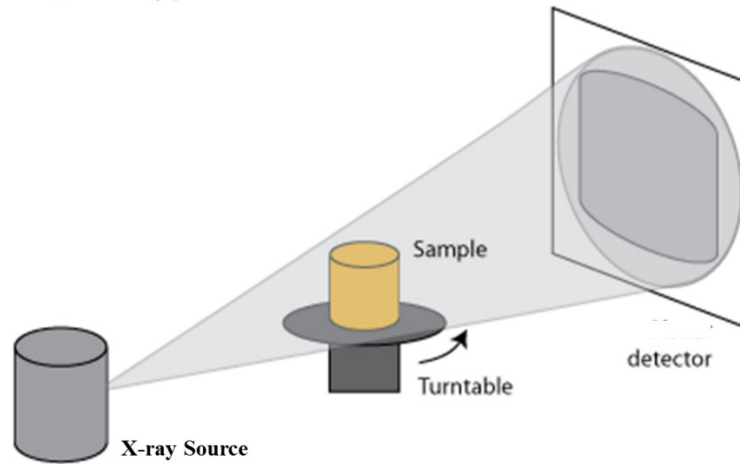


Figure 8-8: Cone Beam Configuration for X-ray Imaging

The result of the reconstruction operation was stacks of 3-D slices. Table 8-1 provides characteristics of the reconstructed images, while Table 8-2 is a summary of the size of stacks for each scan. After image reconstruction, the next step was post processing which involves correction for beam hardening, registration of neutron and X-ray images and then segmentation to identify the different phases present in the material.

Table 8-1: Characteristics of Tomographic Stacks of slices

Imaging Parameters	Neutron	X-Ray
Energy	Thermal neutron (25meV)	90 KeV Maximum (32 Kev Average)
Pixel Size ( $\mu\text{m}$ )	30	30
Voxel depth ( $\mu\text{m}$ )	30	30
Bit Depth	32	32
Average scan file size (GB)	~34.0	~28.0
Reconstruction Method	Parallel	Cone

Table 8-2: Summary of Number of Slices from Reconstruction of Raw Data

	Scan 1		Scan 2		Scan 3		Scan 4		Scan 5		Scan 6	
	Neut.	X-ray	Neut.	X-ray	Neut.	X-ray	Neut	X-ray	Neut	X-ray	Neut	X-ray
DP1			2207	1786	1989	2076	1969	1978	1998	1865	2117	1796
DP2	2147		1996	1797	2210	2108	2178	1924	2178	1881	2123	1941
DP3	1991		2165	1823	2113	1983		1870	2042	1759	2112	1821

The cross in cells indicates that the raw data was damaged and reconstruction not possible.

Neut.: Slices of Neutron images

X-ray: Slices of X-ray images

DPi: Specimen from Set i

#### 8.4- Tomography Image Post-Processing

##### 8.4.1. Image Registration

Image from each of the modality (Neutron and X-ray) taken at different time were misaligned, as well as neutron and X-ray images taken at the same time. Sources of misalignment can be related to the imaging system, to the set up or to the sample being scanned.

Sources of misalignment of images from the two modalities taken at the same time include:

- The vibration of the rotational object holder during scanning

- Misalignment of the two radiation beams: the two beams are not perfectly aligned at 90° angle as expected in theory.
- The geometry of the radiation beams (quasi-parallel beam for neutron versus cone beam for X-ray)
- The fact that the two systems had different resolutions (30µm for neutron VS 51.4 µm for X-ray)
- Errors that may arise during image reconstruction

Beside those mentioned for multimodal combined images, other sources of misalignment pertaining to time series monomodal images included:

- The experimental set up. Since it is not possible to position the specimen exactly the same way between two scans. (Errors in the x,y,z axis can be generated).
- The relative changes and deformations that took place within the specimens between scans like expansion of the specimen.

In order to acutely analyze the images, the misalignment needed to be corrected. The process of correcting the misalignments is image registration. Image registration is a process widely and commonly used in remote sensing, medical imaging and entertainment fields. Its use in the concrete industry started with the use of imaging techniques for concrete analysis.

#### a) Definition

Image registration is a task of geometrically aligning two or more images of the same scene that are taken at different times, from different viewpoints, and/or by different sensors (Zitova e Flusser, 2003). The objective of image registration is to find a spatial

transformation such that dissimilarity metric achieves its minimum between two images taken at different times, from different sensors, or from different viewpoints (Ezzeldeen *et al.*, 2008). Xi et al. (2011) mathematically describe the registration problem: let  $Z_R(x, y, z)$  and  $Z_M(x, y, z)$  be a reference or source image and an image to reference with or target image. The prime objective of the image registration is to determine a geometrical transformation  $T(x, y, z) = (T_1(x, y, z), T_2(x, y, z), T_3(x, y, z))$  such that  $Z_M(x, y, z)$  is as close to  $Z_R(x, y, z)$  as possible. The inputs of registration are the two images to be registered; the output is a geometrical transformation, which is merely a mathematical mapping from points in one image to points in the second. To the extent that corresponding points are mapped together, the registration is successful. Therefore, the registration problem can be defined as the following optimization problem:

$$T_{opt} = \underset{T \in \tau}{\operatorname{argmax}} S(Z_R, Z_M(T)) \quad \text{Eq. 12}$$

Where  $T_{opt}$  denotes the optimal transformation for matching  $Z_R(x, y, z)$  and  $Z_M(x, y, z)$  among all possible transformations in a specific transformation space  $T$  and  $S$  is a selected metric for measuring similarity between the two images.

Misalignment between images may be attributed to different sources: changes in the sensor position, viewpoint and viewing characteristics or the movement and deformation of the object.

#### b) Classification of Registration Methods

There are many image registration methods and they can be classified in many ways and may be condensed into six categories: image dimensionality, registration basis,

geometrical transformation, degree of interaction, optimization procedure, modalities. (Fitzpatrick *et al.*, 2000).

Image dimensionality refers to the number of geometrical dimensions of the Images to register. It can be 2D images, 3D images or 2D/3D registration also called slice to volume registration. In the current study 3D image registration needed to be performed.

The registration basis is the aspect of the two images used to affect the registration. The registration can be based on features: For example, the registration might be based on a given set of point pairs that are known to correspond (point-based method) or a set of corresponding surface pairs (Surface based methods). Registration can also be based on the intensity pattern in the two images (intensity-based methods). In the case of feature base registration methods, correspondences between the features can be obtained from objects that have been attached to the object expressly to facilitate registration. (In this study, Base plates with notches were used to facilitate registration of images (Extrinsic method) in addition to the calibration standards which were also used as basis for the registration (Intrinsic method).

The geometrical transformation used for the registration refers to the nature and the domain of the transformation used in the registration algorithm, meaning the mathematical form of the geometrical mapping used to align points in one image with those in the other.

The degree of interaction is the degree of control exerted by the human operator over the registration algorithm. It ranges from fully automatic algorithm where the interaction consists simply of initialization of certain parameters to manual registration where the user

manually selects distinctive matching control points from the two images to register and then uses them to determine the geometric transformation.

The modality refers to the means by which the images to be registered are acquired. In this case the modalities were X-ray and neutron. When the images are acquired by the same means the registration is called monomodal or intramodal whereas it is called multimodal or intermodal when they are acquired by different means. (The current study uses both multimodal and monomodal time series registration).

In the current study, a hierarchy of these categories of registration methods was made which allowed us to select one category based on various criteria.

#### c) Criteria and Selection of an Image Registration Method

In the current study, image registration was twofold: Registration of images taken from two different sensors (neutron and X-ray tomography) simultaneously, (Dual modality images), and registration of monomodal images taken at various time intervals (time series images). The registration method to be used needed to meet a certain number of criteria:

- The robustness and reliability of the method so that the algorithm can handle noise, occlusion and other problems.
- Accuracy of the transformation computed to meet higher operational requirements.
- The amount of preprocessing and user- interaction required by the method should be minimized.
- The method should be adapted for the dimensionality of images to be registered, both for 2D and 3D images.

- It should allow for registration of multimodal and monomodal data and be specially suited for X-ray and Neutron images.
- The method should allow for multitemporal analysis and should be able to accommodate with small geometric deformations, since small deformation of the specimen are expected over time due to expansion caused by delayed ettringite formation.
- The method should not be computationally too intensive and should not require a lot of computational power. Since Neutron and X ray tomography data set are usually very large (~36 GB) for each specimen data set, the image registration algorithm to be used need not require too much RAM (need not be computationally intensive).

For this purpose, the most appropriate methods seemed to be intensity-based registration methods for the following reasons:

They are more flexible than landmark-based or segmentation-based methods, as they use all of the available information without a previous reduction of data (Lee *et al.*, 2009).

d) Intensity Based Image Registration: The Approach Based on Maximization of Mutual Information

- Different Intensity-based Approach of Image Registration

Intensity based registration methods used pixel or voxel intensity solely to determine the transformation between the source image and the target image. The registration transformation is therefore determined by iteratively optimizing some “similarity measure” calculated from all pixel or voxel values. Fitzpatrick (Fitzpatrick *et al.*, 2000) proposes different similarity measure that can be used to develop intensity- base algorithms:

*Image subtraction:* These approaches use the sum of squares of intensity differences (SSD) to measure the degree of alignment of the images. In this case, SSD will be zero when the images are correctly aligned and will increase with misregistration-registration error.

*The maximization of the correlation coefficient:* Using the correlation coefficient method, the registration problem is to find the transformation that maximizes the correlation coefficient between the mean intensity values of voxels of the two images.

*The minimization of the joint histogram entropy:* The entropy can be defined as a measure of the incertitude or information content, while the joint entropy is a measure of the uncertainty associated with a set of variables. For a pair of discrete random variables  $(X, Y)$  with a joint probability distribution  $p(x, y)$ , the joint entropy is expressed as:

$$H(X, Y) = - \sum_{x \in X} \sum_{y \in Y} p(x, y) \log(p(x, y)) \quad \text{Eq. 13}$$

Or simply

$$H(X, Y) = -E \log(X, Y) \quad \text{Eq. 14}$$

Therefore, as the entropy becomes smaller, the incertitude decreases. For images, the joint entropy of two images is found by determination of the joint histogram of the two images.

The registration problem becomes the determination of the transformation  $T$  that minimizes the joint entropy of the two images.

*The maximization of mutual information.* This method is also based on the entropy but uses the information-theoretic measure mutual information (MI) or relative entropy instead of the joint entropy. The mutual information “MI is a basic concept from information theory,

measuring the statistical dependence between two random variables or the amount of information that one variable contains about the other” (Maes *et al.*, 1997). Therefore, the MI of the image intensity values of corresponding voxel pairs is maximal if the images are geometrically aligned.

#### e) Image Registration by Maximization of Mutual Information

Registration of multimodal images by maximization of mutual information was simultaneously introduced researchers in Belgium (Maes *et al.*, 1997) and USA (Viola e Wells Iii, 1997) in order to overcome limitations of feature base registration methods and other intensity-based methods, for its high accuracy and robustness with regards to illumination, to occlusion of one signal.

Mutual information is an entropy-based metric adapted from information theory which represents the amount of shared information two random variables have about one another in terms of bits. Typically, the entropy definition used is the Shannon entropy given by eq. 13 (Sabuncu, 2006):

$$H = \sum -p_i \log(p_i). \quad \text{Eq. 15}$$

Where:  $p_i$  is the probability distribution.

The method of mutual information can be mathematically expressed as follow: Given two images A the source and B the image to register. B' the registered image of B with A, the mutual information of A and B' is given by:

$$MI(A, B') = H(A) + H(B') - H(A, B') \quad \text{Eq. 16}$$

Where:  $H(A)$ : entropy of A;  $H(B')$ : entropy of B' and  $H(A, B')$ : joint entropy of A and B'.

To register A and B is to find the transformation  $T$  that maximizes  $MI(A, B')$ . When A and B are registered, the amount of information they contain about each other is maximal.

#### f) Approach to Image Registration Used in this Project

To ensure that each pixel in the combined slice was assigned its correct X-ray and neutron attenuation factor values, it was essential that the CT slices be accurately registered with each other. Given the cylindrical symmetry of the samples, the alignment of the X-ray and neutron slices involves two coordinates, the rotational angle around the central axis and the vertical position of the slice. Image registration for this project was performed through successive steps:

- Preprocessing

Preprocessing of the data involved the preparation of the samples before they were scanned and the preliminary alignment of the data before they were subjected to the registration algorithm.

During the sample setting preparation, upon casting and heat treatment, stainless steel bases were fastened to the bottom of concrete cylinders. These bases had threaded rods that screw into the CT stage for accurate alignment. Finally, three notches had been milled into the steel base plates at unequal distances around the circumference to provide fiducial marks for accurate registration among the reconstructed 3D tomograms from different scans (Figure 5-15).

After the cylinders were scanned and the images reconstructed, X-ray images were rotated by 90 degree in order to obtain a rough alignment with neutron images, since the X-ray and neutron beams intersect at an angle of 90 degrees (Figure 7-4). This rough alignment could

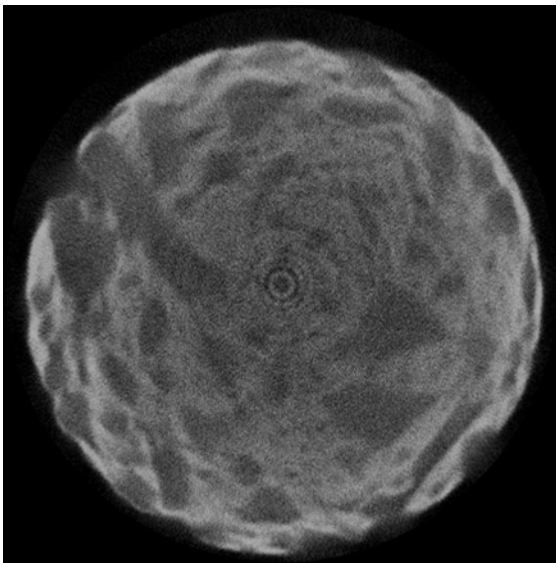
not provide for an accurate registration of X-ray and neutron 3D images because it does not take into account the vertical tilt of the cylinder with respect to the axis of the CT stage.

- Processing

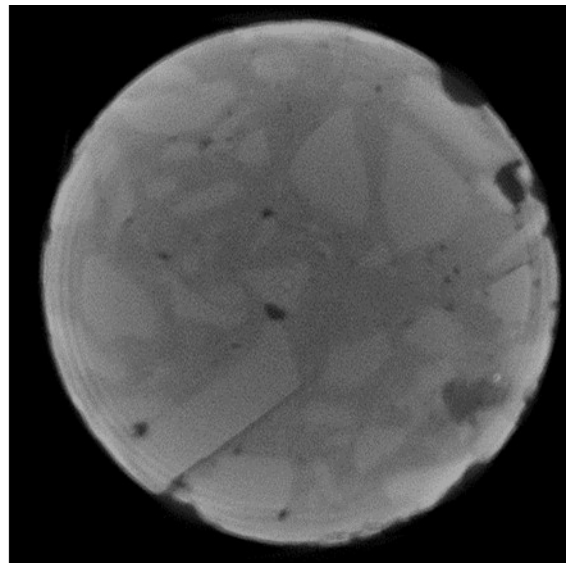
A MATLAB routine for registration was developed that applies a cross-correlation against each other on a pixel by pixel basis. The routine developed in conjunction with researchers at the NCNR allowed for registration of multimodal 3D images and also monomodal time series 3D images.

For monomodal time series image registration, the source image was the images from the first scan and all subsequent scans were registered relatively to source images.

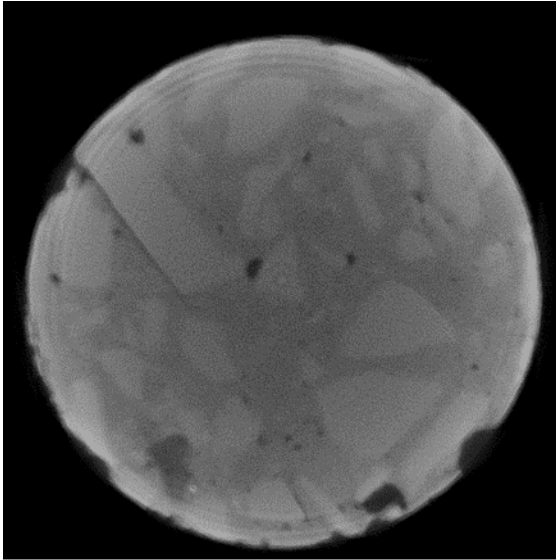
For bimodal image registration, the source images where neutron images and X-ray images were the target. Neutron and X-ray images from the same scan were registered. Figure 8-9 and Figure 8-10 show samples of bimodal registration slices and time series monomodal slices registered.



**(a)**

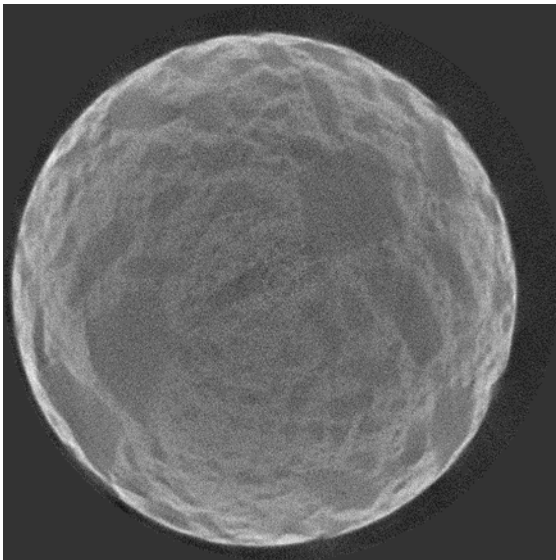


**(b)**

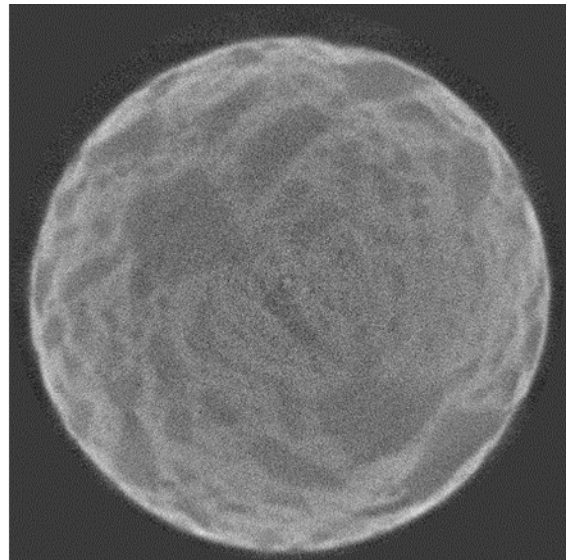


**(c)**

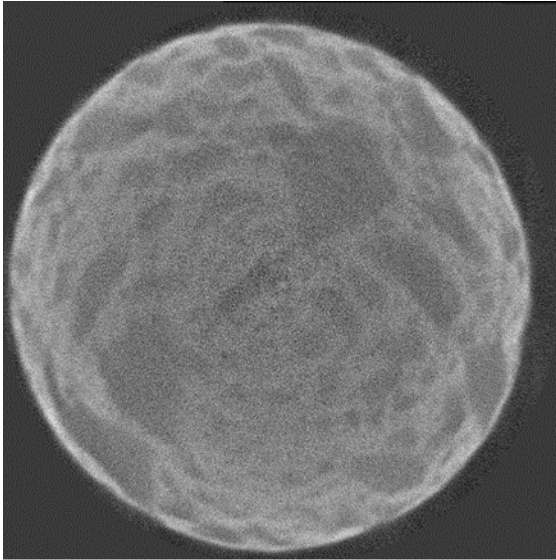
Figure 8-9: Bimodal registration a) Source: Neutron image, b) target X-ray image, c) registered X-ray image



**(a)**



**(b)**



(c)

Figure 8-10: Time series Neutron Image Registration a) Source: Scan DP1-2-5, b) target: Image Scan DP1-2-6, c) Registered Image of Scan DP1-2-6

#### 8.4.2. Beam Hardening

##### a) Introduction and Definition

The beam hardening was originally discovered and studied for the case of X-ray attenuation through matter by Brooks and Di Chiro in 1976 (Hachouf *et al.*, 2012) and has since been known in computed tomography to be one of the major sources of deterministic errors leading to inaccuracy and artifacts in the reconstructed image. As a polychromatic neutron or X-ray beams passes through an attenuating material, lower-energy rays are preferentially absorbed or scattered, raising the mean energy of the beam even as the overall intensity falls (Ketcham e Hanna, 2014). Because of this phenomenon, regions interior to the object are traversed with higher energy rays than regions towards the edges, making the edges more attenuating than the interior. Since the transmitted beam increases with the crossed thickness, the gray level in the projection image of the constitutive material the Beer-lambert law (Eq. 17) is no longer valid and the relationship between the path length and

the logarithm of the intensity in the Beer-Lambert law is no longer linear. The relation can then be expressed with a complicated integral (Eq.18) (Hachouf *et al.*, 2016):

$$I(E) = I_0(E)(e^{(-\int \mu(E)ds})} \text{ (Beer-Lambert Law) Eq. 17}$$

$$I(E) = I_0(E) \int_0^\infty P(E)(e^{(-\int \mu(E)ds})} dE \text{ (Modified Beer-Lambert Law) Eq. 18}$$

Where:  $I(E)$  is the intensity of the transmitted radiation beam,  $I_0(E)$  the intensity of the incident beam,  $\mu(E)$  the attenuation coefficient of the material under investigation for the specific radiation type,  $d$  the length of the radiation path through the object and  $P(E)$  is the probability that the detected neutron is at energy  $E$ . This phenomenon is known as the beam hardening. Beam hardening is more pronounced for heavy matrices like geologic samples, rock and concrete cores.

Consequences of beam hardening on the obtain images are multiple. The most important of which is the fact that on the images, there is a range of attenuation values for each phase rather than a single value for each individual solid phase. The same solid phase seems to have higher attenuation values at the periphery of the concrete core than towards the center of the core. As a consequence, in addition to gradient values mentioned above, some artifacts are induced:

- The cupping effects
- The appearance of streaks between highly attenuating structures.

Beam hardening makes it difficult to accurately perform segmentation and quantitatively separate the different phase, or to identify complex mineral relationships such as exsolution and zonation effects within a sample.

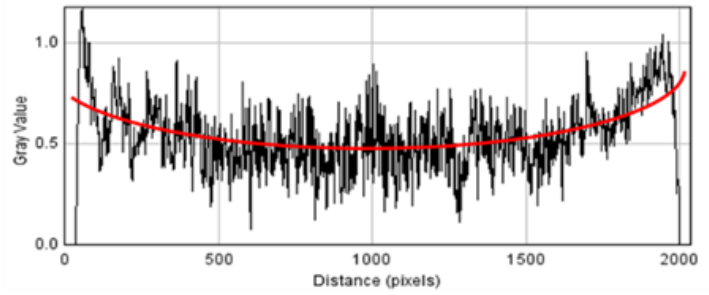
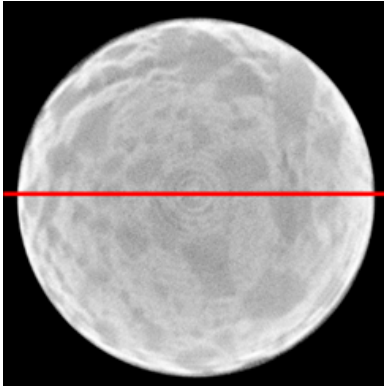


Figure 8-11: Position of a profile line across a neutron CT slice and grayscale values of the profile showing the cupped pattern due to beam hardening

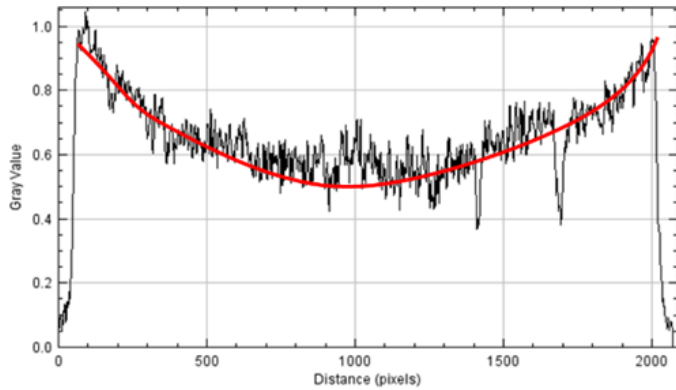
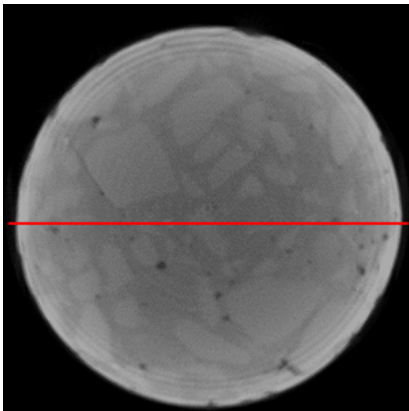


Figure 8-12: Position of a Profile Line Across an X-ray CT Slice and Grayscale Values of the Profile Showing the Cupped Pattern Due to Beam Hardening

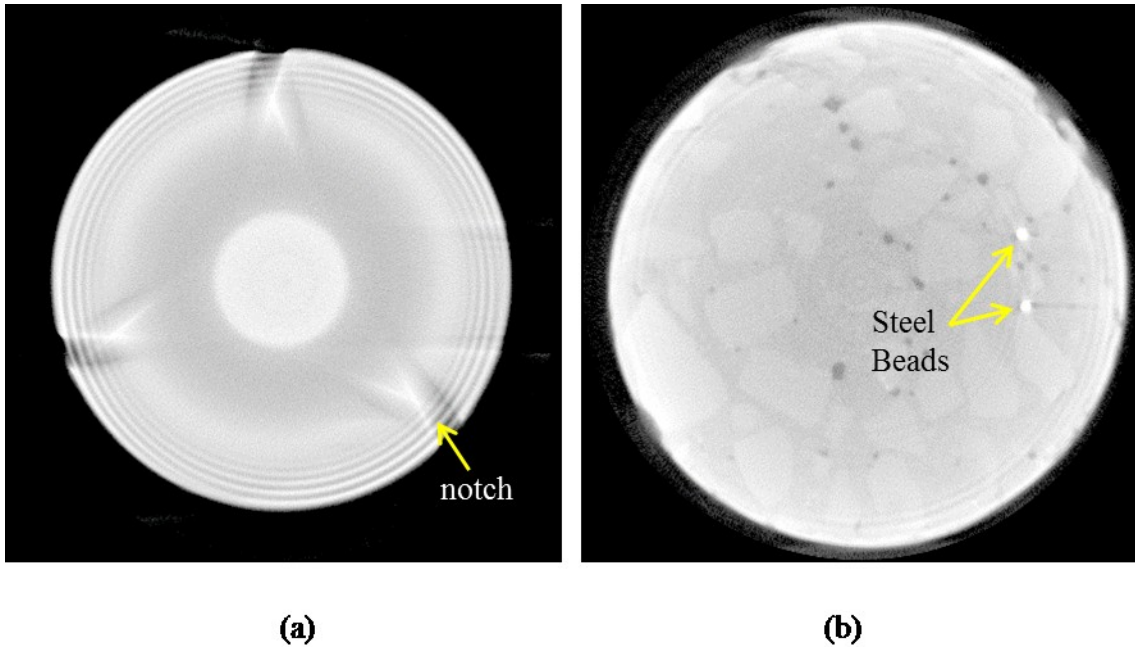


Figure 8-13: X-ray Slice of the Steel Base Plate Showing Streak Artifacts Radiating from the Notches (a) and Slice of the Concrete Cylinder Showing Streak Radiating from the Steel Beads (b)

#### b) Overview of Common Methods of Beam Hardening Correction

Beam hardening can be addressed or at least mitigated at three different stages: during image acquisition, during image reconstruction (pre-processing) or after image reconstruction (Post-reconstruction or post-processing methods). The methods can be classified in three main categories (Brabant *et al.*, 2012).

##### - *Beam hardening Correction during Image Acquisition by Physical Filtration or Pre-filtering*

This technique is mostly used for imaging with an X-ray beam. It aims to address beam hardening during the calibration and /or scanning by pre-hardening the beam using physical pre-filters. This method consists of placing filters usually made of aluminum, copper or brass between the x-ray source and the sample. This way, the low energy rays are already removed before the beam reaches the sample (The beam is pre-hardened) in such a way

that the spectrum is approximated to a monochromatic energy distribution (Krumm *et al.*, 2008). This approach can reduce the artifacts, but in most cases, cannot completely remove it. For it to be effective, the filter needs to be thick enough, the drawback is then that it increases the scanning time. In addition, the technique produces inadequate results in the case of composite material or multi -material objects with highly different attenuation coefficients (Krumm *et al.*, 2008).

- *Beam Hardening Correction by Algorithm*

This method consists of reducing the beam hardening computationally. This can be done before image reconstruction (pre-processing) or after image reconstruction (post-processing).

The most common pre-processing method is the linearization described by Herman et al. in 1979 (Ketcham e Hanna, 2014). The method is simple and straightforward for specimen made of a single material, but more complex for specimen made of multiple phases like concrete. It aims to transform the measured polychromatic attenuation data into a monochromatic attenuation data with the use of a function which is typically an exponential or a polynomial of undetermined degree. For homogeneous man-made materials, polynomial coefficients can be derived by imaging phantoms of various thicknesses. However, when materials are heterogeneous or not well characterized, as is usually the case with geological materials and concrete, such methods might not be available.

Post-processing or post-reconstruction method is an iterative approach; the image is first reconstructed from the raw data, and then segmented into different material or phases. The obtained segments are then forward projected separately to obtain new raw data, with the beam-hardening model incorporated. The forward projection must correctly model the

beam polychromaticity and account for all physical effects, including the energy dependence of the assumed materials in the specimen, the detector response, and others. The major disadvantage of this method is the necessity of previous knowledge of the characteristics of all materials present and the used energy distribution (Krumm *et al.*, 2008).

- *The Dual Energy Method of Beam Hardening Correction*

The dual energy approach takes advantage of the fact that linear attenuation to X-ray can be decomposed into the photoelectric absorption and the Compton scatter components; therefore, the attenuation of a radiation is based not only on the radiation energy but also on the sample chemical composition and density of the material. The method requires two measurements of the specimen at different energy levels. In fact, based on measurements at a single energy level, it is not possible to differentiate materials on basis of their density and chemistry. However, with measurement at two different energy levels or with dual modality, this dual information can be extracted. The drawback for this method is the need of two X-ray or neutron sources or detectors or two scans (Brabant *et al.*, 2012).

c) Complexity of Beam Hardening in a Multiphase Material Like Concrete

The beam hardening problem is more complex with multi-phase materials like concrete than with single phase materials, because each phase has different behavior to the beam hardening (Ketcham e Hanna, 2014). Complexity of the beam hardening effect for neutron CT is illustrated in Figure 8-14 in which a neutron CT slice is partitioned into a series of 19 concentric rings 50 pixels wide. The grayscale histograms calculated for each ring are plotted in Figure 8-15. It can be seen that the peak associated with the aggregate shifts

toward lower pixel intensity, i.e. lower attenuation factor values, with distance into the material. Thus, the segments of a grayscale histogram calculated from the entire image will be smeared out and overlap. Figure 8-16 which is the plot of the aggregate peaks as a function of the ring diameter further illustrates beam hardening as it can be seen that the aggregate peak intensity decreases as we get deeper into the material.

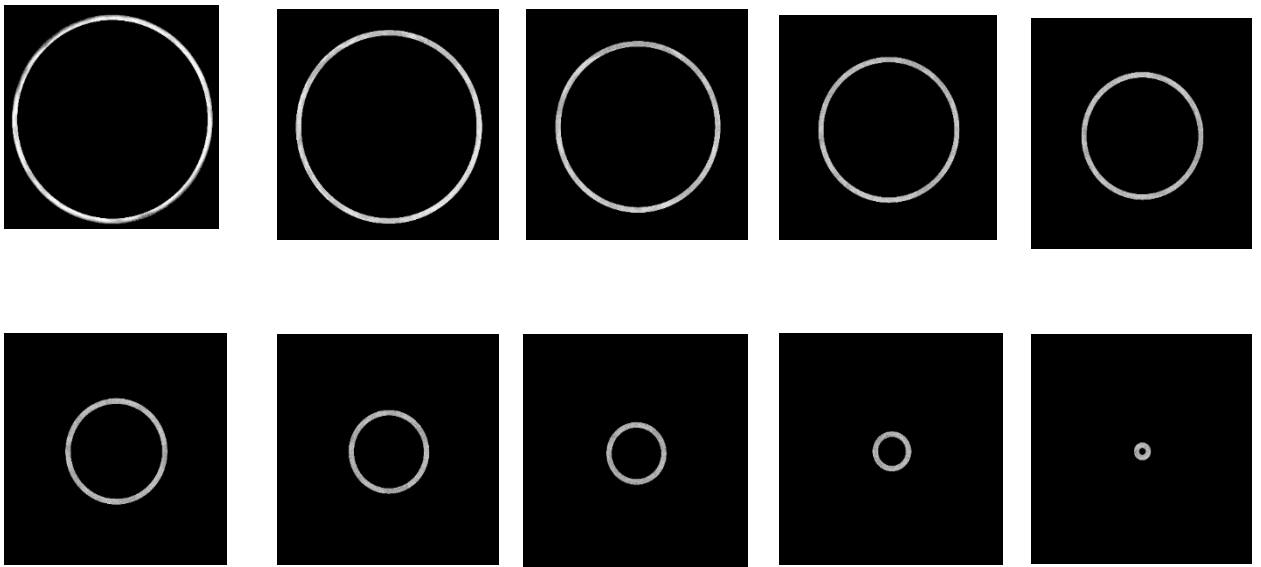


Figure 8-14: Neutron Slice Partitioned Into 50 Pixels Wide Rings

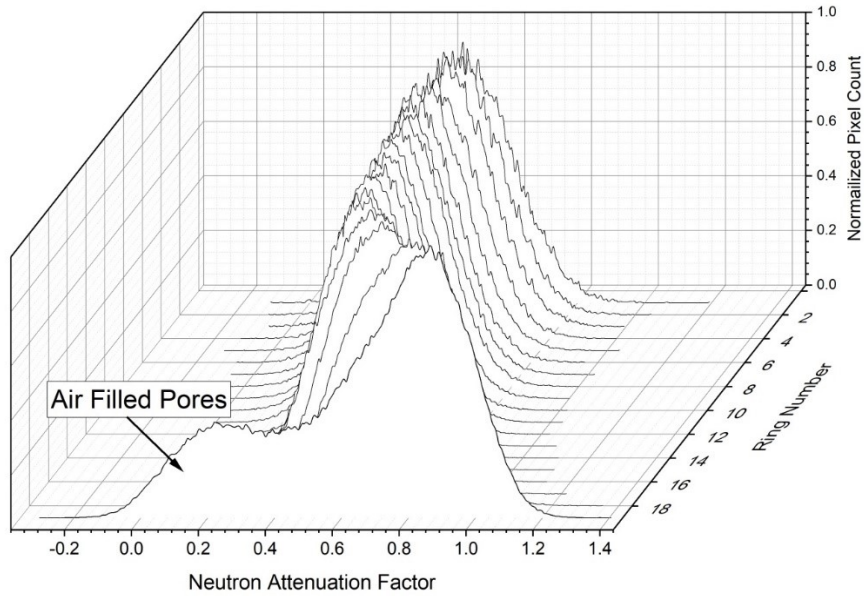


Figure 8-15: Grayscale Histogram for Individual Rings Of A Neutron CT Slice. Ring Width=50 Pixels; Outermost Ring Includes Air -Filled Pores

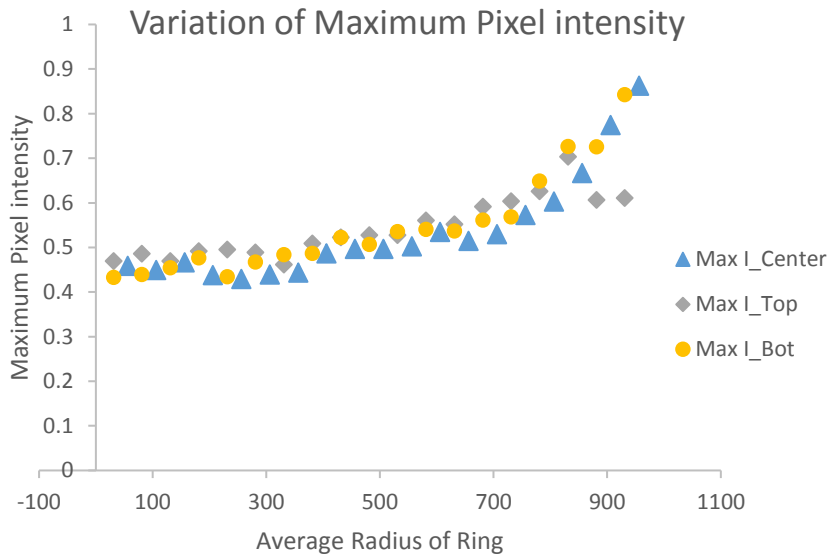


Figure 8-16: Plot of the Aggregate Peak Intensity of Individual Rings. The Variation is Shown for a Slice Taken at the Upper (Top), Middle (Center) and Lower (Bot) Sections of the Specimen

Most approaches mentioned in the previous sections are not effective when dealing with complex samples like geological structures or multiple phase materials like concrete as it is the case in this study. In fact, their application is limited to specific cases. As an example, pre-filtering works well with light material but is ineffective with dense samples; linearization method works well only for single phase materials, post reconstruction methods work only if the segmentation of the material is possible without prior beam hardening correction while the dual energy method deals with material of fairly-known composition. In this study we developed an approach of segmentation without the need to correct images for beam hardening. The method takes advantage of the fact that beam hardening is radial (Jovanovic *et al.*, 2013) and the fact that the specimens used in this study were cylindrical in shape. The method is presented in section 8.4.3.

#### d) Neutron Beam Hardening

The neutron CT grayscale histogram is the frequency distribution of the pixels as a function of their values of the total attenuation factor,  $\Sigma_T$ . This in turn is the sum:

$$\Sigma_T = \Sigma_c + \Sigma_s \quad \text{Eq. 19}$$

Where  $\Sigma_c$  is the macroscopic capture cross-section and  $\Sigma_s$  is the macroscopic scattering cross-section

The macroscopic cross sections are calculated from the microscopic cross-sections,  $\sigma_c$  and  $\sigma_s$ ,

$$\Sigma = \frac{\sigma \rho A_v}{M} \quad \text{Eq. 20}$$

Where  $\rho$  is density,  $M$  is atomic weight and  $A_v$  is Avogadro's number.

The scattering cross-section is independent of energy. However, for the elements found in concrete the capture cross section varies by  $1/v$ , where  $v$  is average neutron velocity in the spectrum (Stacey, 2007). The neutron's velocity is related to its energy by:

$$v = \sqrt{\frac{2E}{m}} = \sqrt{\frac{E}{5.227}} \quad \text{Eq. 21}$$

For  $E$  in MeV and  $v$  in km/s.

The tabulated values for  $\sigma_c$  are given for a specified value,  $v_0$ , of 2,200 m/s, which is the characteristic velocity of a neutron in thermal equilibrium at a temperature of 23°. Thus the attenuation factor has the form:

$$\Sigma_T(v) = \frac{v_0}{v} \Sigma_{c_0} + \Sigma_s \quad \text{Eq. 22}$$

Where  $\Sigma_{c_0} = \Sigma_c(v_0)$

Then the shift in the position of a phase in the grayscale histogram due to a change in the local velocity from  $v_0$  to  $v$  is:

$$\Sigma_T(v_0) - \Sigma_T(v) = \Sigma_{c_0} \left(1 - \frac{v_0}{v}\right) \quad \text{Eq. 23}$$

Since  $\Sigma_{c_0}$  is typically different for each phase, the implication is the shift in position of one phase such as the aggregate is not the same for the other phases.

This same reasoning can be applied to show that for X-ray CT, the shift in position is different for each phase too. This renders correction for beam hardening more difficult and complex because correction needs to be done at the pixel level and for each material phase.

#### e) X-ray Beam Hardening

Hardening of the X-ray beam was also observed (Figure 8-12). The beam hardening effect originates in the use of polychromatic X-ray sources. All computed tomography

reconstruction procedures are based on the assumption that attenuation coefficients with monochromatic X-rays do not change during passage through the bulk material in accordance with Beer's law. This is true only for synchrotron-based X-ray sources, but not for polychromatic X-ray beams (Jovanovic *et al.*, 2013). As a consequence of this, it can be seen that the attenuation factors of Calcium (Ca) and silicon (Si), which are the dominant constituents of the total attenuation factor are very sensitive to X-ray energy over the range to be found in the imaging system used (NeXT), 20-90 keV. For example, their attenuation at 45 keV is 3 to 4 times higher than at 90 keV based on attenuation values calculated using the NIST XCOM database as plotted in Figure 8-17.

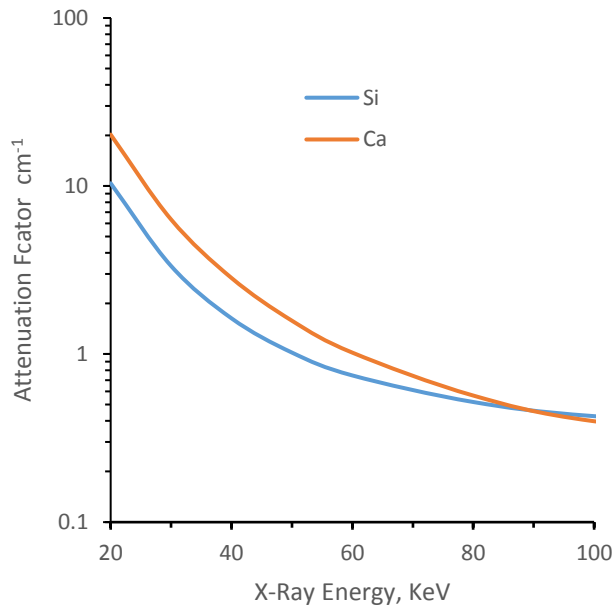


Figure 8-17: Plot of X-Ray Attenuation Factors VS Photon Energy

The other elements present in concrete phases would show similar trends.

### 8.4.3. Overview of Image Segmentation

#### a) Definition

In digital image processing, segmentation is the process of partitioning an image into multiple segments (sets of pixels) with the goal to simplify or change its representation into something that is more meaningful and easier to analyze. More precisely, image segmentation is the process of assigning a label to every pixel in an image such that pixels with the same label share certain characteristics (color, intensity or texture). Image segmentation is typically used to locate objects and boundaries (lines, curves, etc.). In the case of our project Image segmentation consisted of assigning each pixel into one of the several classes of material phases found in concrete.

#### b) Classification of Image Segmentation Methods

Images segmentation methods can be classified into various categories (Kang *et al.*, 2009).

- Region based segmentation methods that segment the image into various regions having similar characteristics. Threshold based segmentation is the simplest segmentation method. This method is based on a clip-level (or a threshold value) to turn a gray-scale image into a binary image. Other methods in this category includes the region growth and the region operating methods
- Edge based segmentation methods. An edge is a set of linked pixels lying on the boundary between different regions, where there are intense discontinuities such as gray change, color distinctness, texture variety and so on. An image can therefore be segmented by detecting those discontinuities. Methods that use this principle include the gray histogram method and the gradient-based method.

- The segmentation base on clustering. Clustering is the classification of things in classes, which are collections of similar elements. These techniques segment the image into clusters having pixels with similar characteristics. The most common algorithm used in the clustering-based methods is the K-means algorithm.
- Histogram-based methods. It is one of the simplest and most often used segmentation techniques compared to other image segmentation techniques. In this technique, a histogram is computed from all of the pixels in the image, and the peaks and valleys in the histogram are used to locate the clusters in the image.
- Other methods include the watershed-based method; the partial differential equation (PDE) based method and the artificial neural network (ANN) method. Figure 8-18 below is a schematic of the various methods.

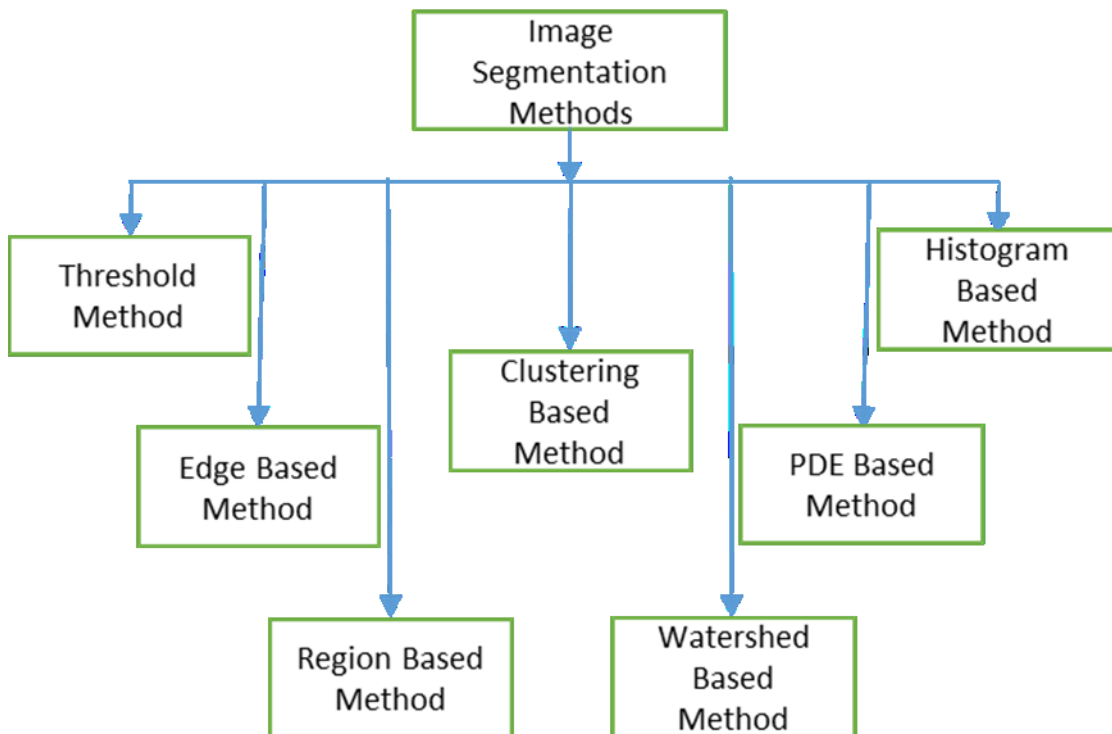


Figure 8-18: Synopsis of Image Segmentation Methods

#### 8.4.4. An Approach of Simultaneous Image Segmentation and Beam Hardening Correction through Slice Partitioning

As mentioned in the previous sections, accurate segmentation requires that beam hardening artifacts be corrected. The lack of an effective method of beam hardening correction for multiphase and heterogeneous material like concrete increases the complexity of the problem. A method was developed for image segmentation which combines image fusion and beam hardening correction through slices partitioning. The fusion of Neutron and X-ray images allows for construction of 2-D histogram used for pixel assignment. The method is therefore a histogram-based method. It relies on the findings of Jovanovic (Jovanovic *et al.*, 2013) stating that beam hardening artifacts in the reconstructed image is a radial function and is also specific to each material, i.e. it depends for each material only on distance from the center of the cylinder. The method therefore takes advantage of the fact that we used cylindrical samples in the study.

Image fusion is the process of combining multiple input images into a fused image, which is expected to be more informative for human or machine perception as compared to any of the input images. It can be performed at different levels: signal, pixel, feature or decision (Suthakar *et al.*, 2014). In this study, the fusion takes place at the pixel level by the assignment of the pixel into one of the several classes of material phases found in concrete.

Slices are partitioned in rings across which the beam energy is assumed constant as described in section 8.4.2.c. The slices were partitioned in rings 50 pixel thick. So there were 20 rings for each slice. For a neutron slice for example, the 1D grayscale histogram for each ring is calculated and Figure 8-15 shows that the peak which is associated with the aggregate shifts toward lower pixel intensity, i.e. lower attenuation factor values, with

distance into the material. The shift in the position of a phase in the grayscale histogram due to a change in the local velocity from  $v_0$  to  $v$  caused by hardening of the beam is given by Eq. 22:

$$\Sigma_T(v_0) - \Sigma_T(v) = \Sigma_{c_0} \left(1 - \frac{v_0}{v}\right) \quad \text{Eq. 24}$$

Since  $\Sigma_{c_0}$  is typically different for each phase, the implication is the shift in position of one phase such as the aggregate is not the same for the other phases. In order to correct for this effect, the boundaries for segmentation of the grayscale should be adjusted for each ring using the  $v$  calculated from the shift in the aggregate peak. However, these values of  $v$  do not need to be calculated for every slice in the stack. Instead the values obtained from a few representative slices can be applied to the rest. The implication is that the beam hardening correction and image segmentation cannot be carried out in separate steps.

#### a) 2-D Histogram

In image processing, a 2D or bivariate histogram is a plot that shows the relationship of pixel intensities at the exact position between two images, in this case a neutron slice and the corresponding X-ray slice. 2D histograms are more suited for segmentation in this case than 1D because they can allow for greater separation between material peaks. The greater separation of peaks is necessary to properly identify and distinguish ettringite from water as they have similar neutron attenuation coefficients but different X-ray mass attenuation coefficients. For each series of Neutron and the corresponding X-ray data, the slices were partitioned, and corresponding rings of corresponding neutron and X-ray slices fused and the 2D histogram plotted. Each point in the plot is the number of pixels in the image with the specific values of the neutron and X-ray attenuation factors given by its coordinates.

Figure 8-19 shows examples of individual 1D pixel intensities histograms of a neutron (a) and its corresponding X-ray volume (b) while Figure 8-20 is a plot of the 2D pixel intensity histogram corresponding to the pair.

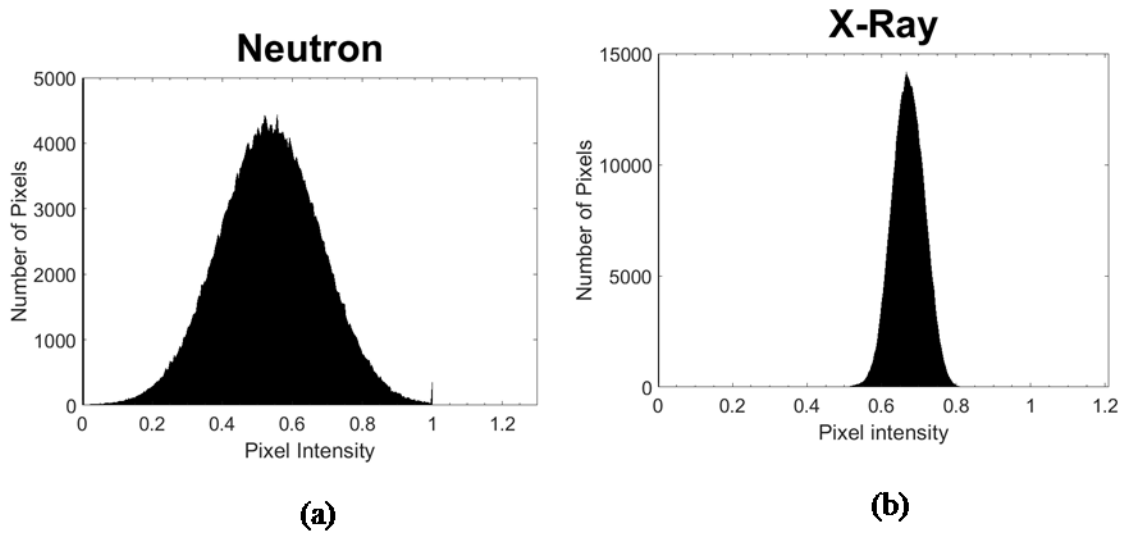


Figure 8-19: Example 1D Histograms of Pixel Intensity of Neutron (a) and X-ray (b) volumes

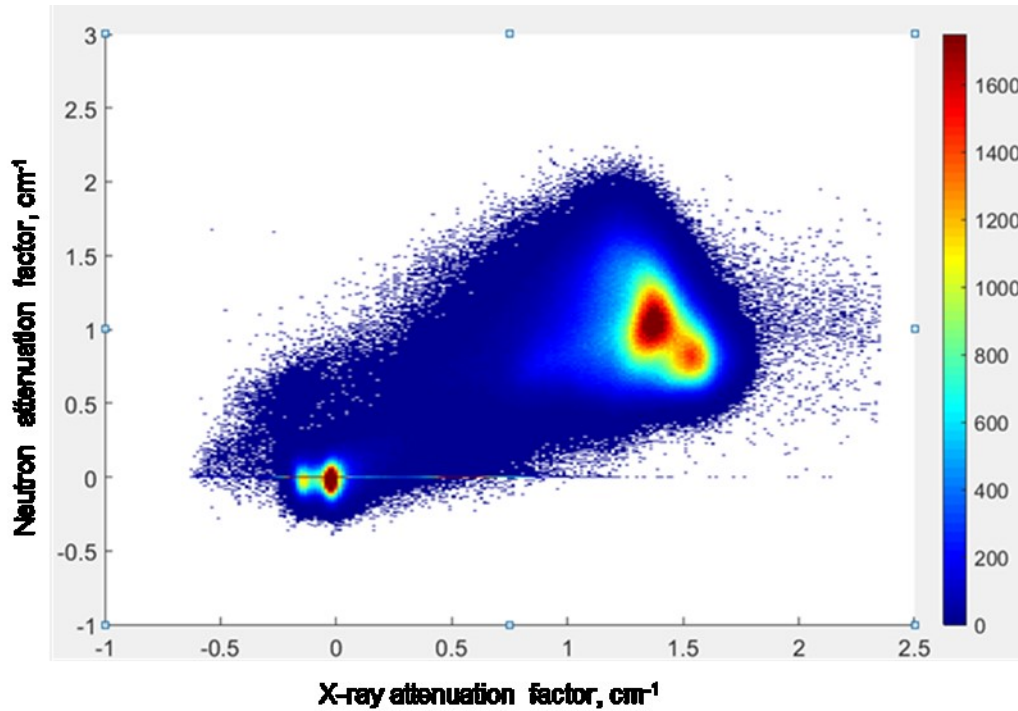


Figure 8-20: 2D Binary Histogram of Pixel Intensity Summed over a Neutron and the Corresponding X-ray Volume

b) Pixel Classification

Once the 2D histogram for a given ring diameter was obtained, the peaks and valleys on the histogram corresponded each to a specific phase. Pixel classification was done based on the plot of Figure 5-7. Segmentation regions were drawn as polygons around the coordinates of points identified in Figure 5-7 and used to classify the pixels into the concrete phases (Figure 8-21). Each ring was segmented independently, and the process was repeated on all the 20 rings. After segmentation of all the rings, they were reassembled into segmented slices (Figure 8-22).

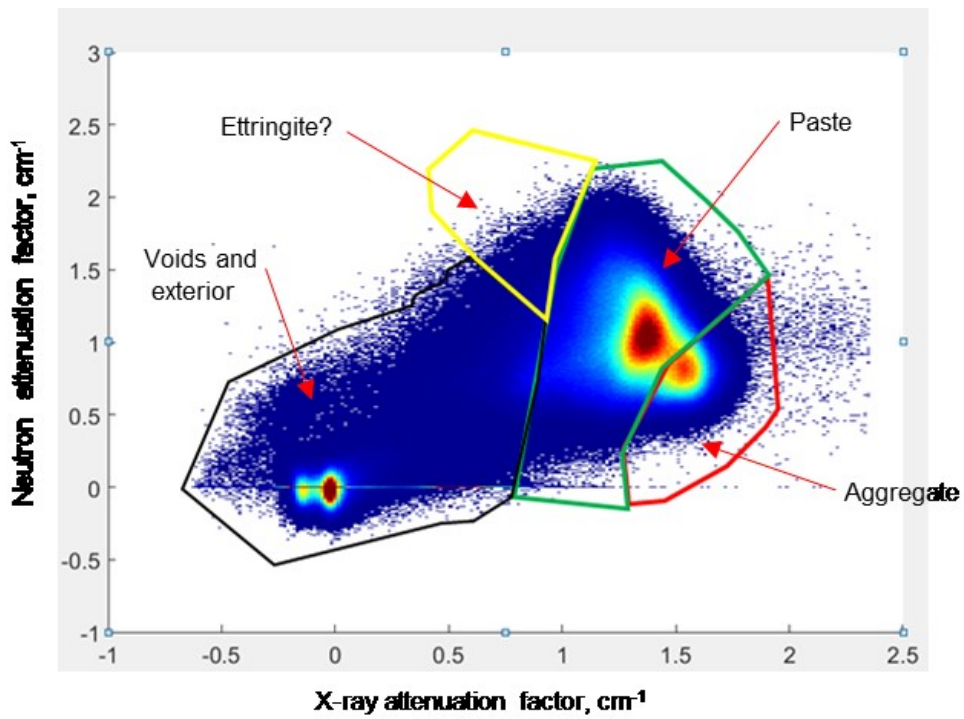


Figure 8-21: 2D Binary Histogram of Pixel Intensities over a Volume with Polygons Delimitations of Expected Locations of Phases

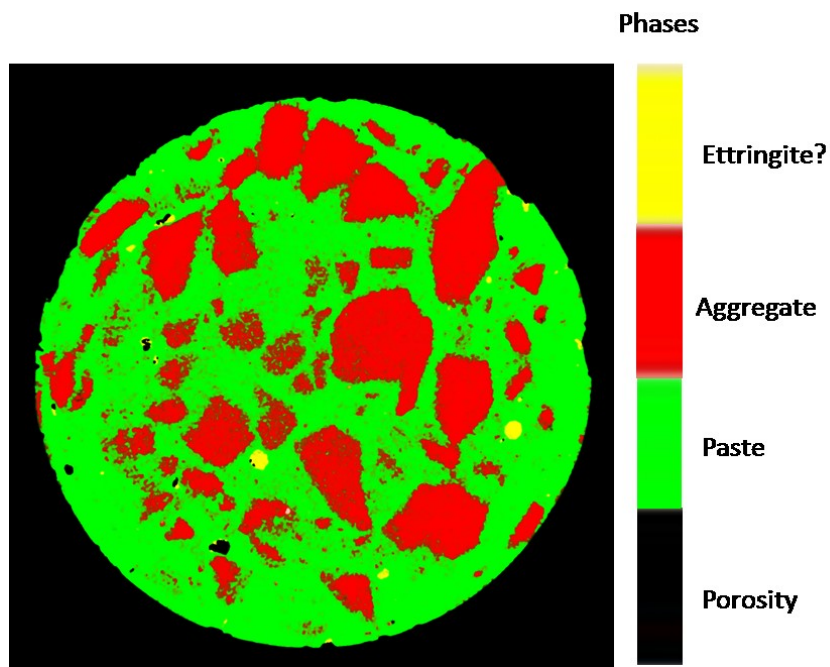


Figure 8-22: Registered and Fused X-ray and Neutron CT Slice Segmented

## Chapter 9 : Tests Results

### *9.1- Concrete Expansion Results*

From each concrete set, five (05) 3in. x 3in. x 11.25in. cylinders were measured for expansion and the average of the five values recorded. Upon demolding, control specimens were stored in the moist room in saturated condition, while the others were subjected to the Duggan heat cycle and cooled for two days. Then all the specimens were measured and stored in saturated limewater for the rest of the experiment

The initial length measurements were taken after heat treatment and just before storage in saturated limewater. Subsequent measurements were then made at regular intervals of two days until appearance of hairline cracks on the surface, then every 5 days afterward.

Overall, specimens with high potassium displayed highest expansion followed by those with normal potassium and heat-treated (Figure 9-1). Based on the threshold of expansion of 0.01% at 20 days set by Duggan (Scott and Duggan, 1986), the concrete can be classified as non-expansive with expansions of 0.023%, 0.023% and -0.005% respectively for the set with normal potassium heat treated, the set with high potassium and the control set. Based on this, aggregates used in the concrete for the research was classified as non-reactive. Hairline cracks started to appear on specimens with high potassium around age 337 days. The difference in expansion of heat-treated specimens between specimens with high potassium and those with normal level of potassium can be attributed to the addition of potassium. Control specimen had little to no expansion throughout the experimental study in contrast to heat-treated specimens. This suggests that heat treatment plays an important role as it induces the initial microcracking needed to promote expansion of the specimens, as those cracks serve as transport media for water required for the reaction leading to

ettringite in pores and also, they serve as nucleation sites for ettringite particles. The total expansion recorded were 0.8% for heat-treated specimens with normal potassium, 1.64% for heat-treated specimen with high potassium and 0.018% for control specimens.

The rate of expansion for both heat-treated specimens followed the same trend with a period of rapid increase until a peak is reached (0.006% at 144 days for specimens with normal potassium and 0.01% at 149 days for specimens with high potassium) then the rate decreases progressively. (Figure 9-2 to Figure 9-4).

The difference in expansive behavior observed with the three sets of specimens is consistent with findings from previous research conducted at University of Maryland in recent years by Ceesay (Ceesay, 2007) and Ramadan (Ramadan, 2000) and suggest that the expansion is associated with the formation of ettringite.

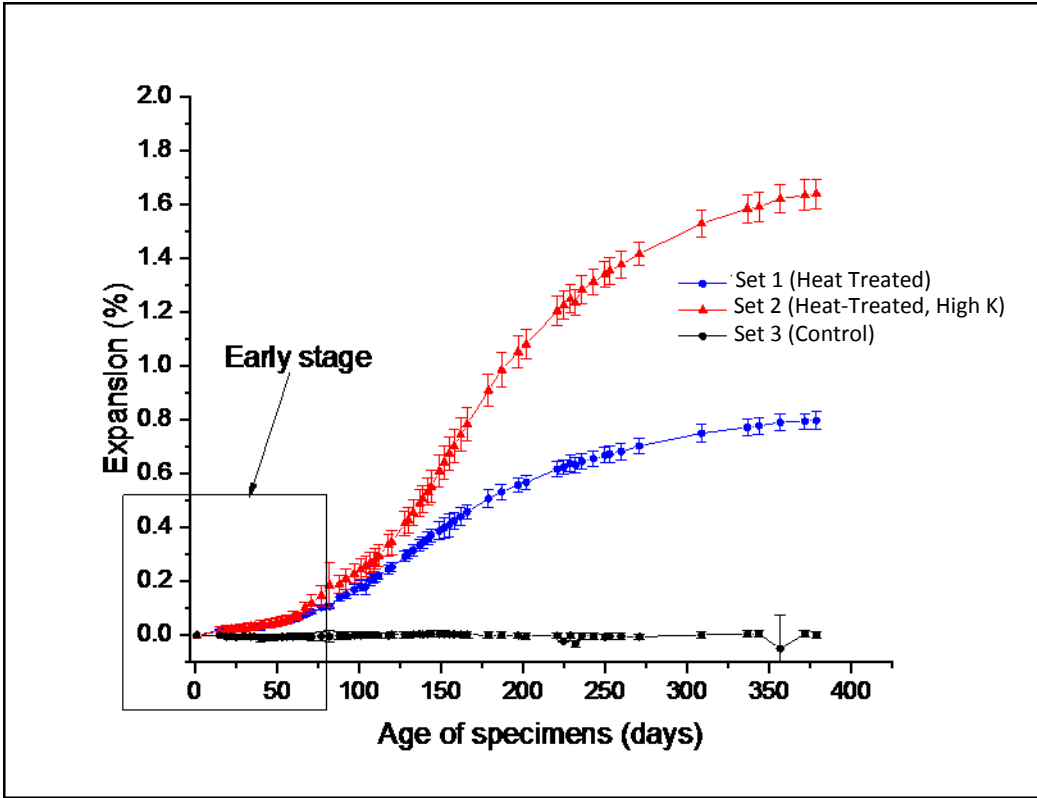


Figure 9-1: Plot of Expansion of Concrete Specimens

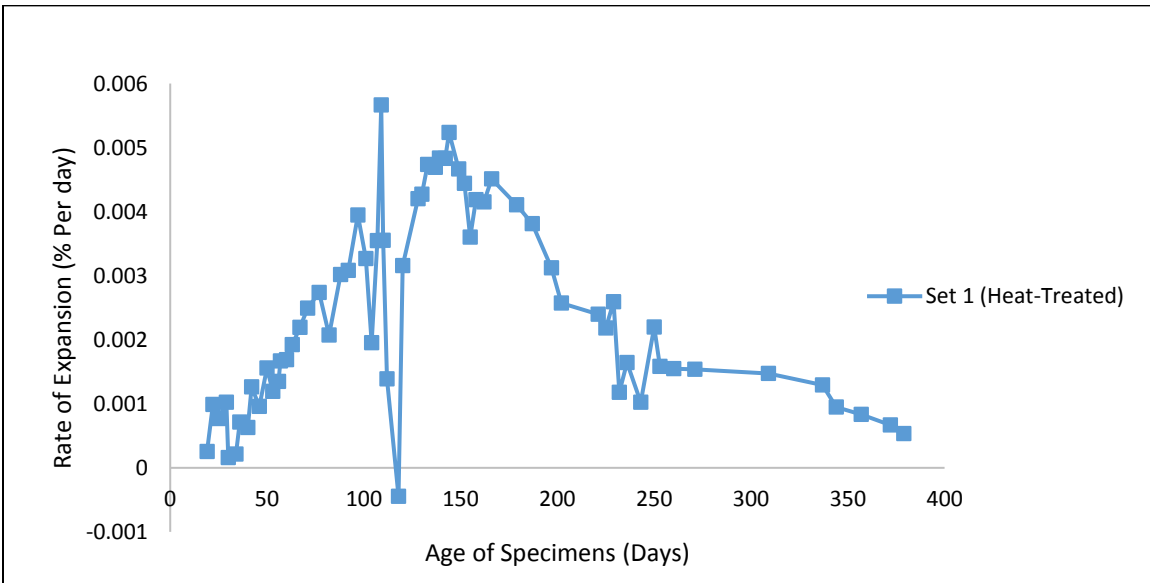


Figure 9-2: Rate of Expansion of Heat-Treated Specimens with Normal Potassium



Figure 9-3: Rate of Expansion of Heat-Treated Specimens with High Potassium

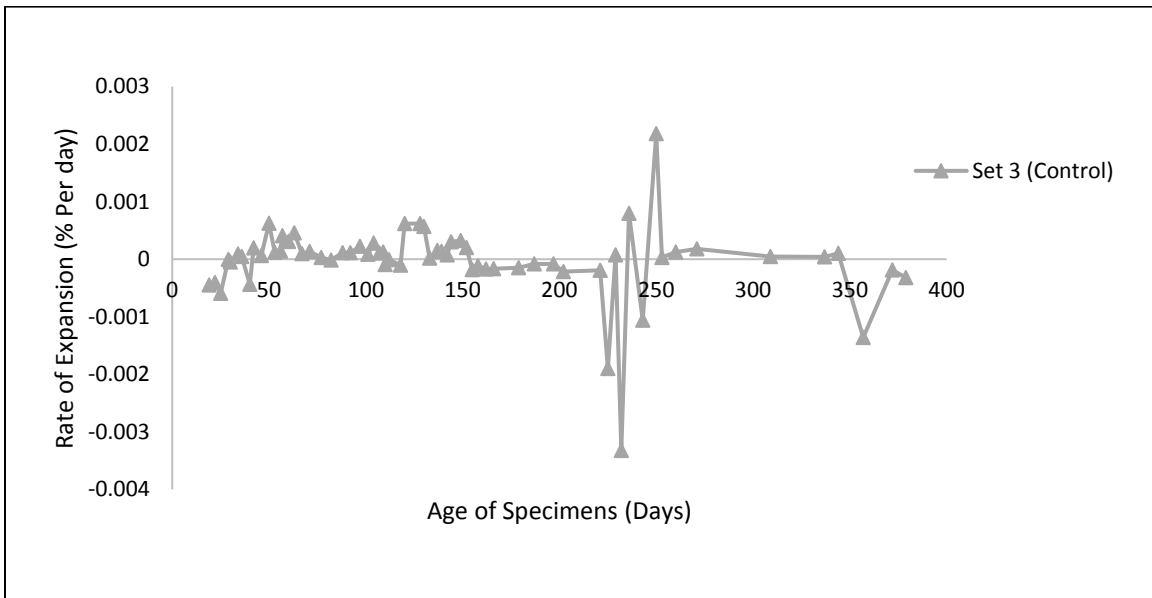


Figure 9-4: Rate of Expansion of Control Specimens



Figure 9-5: Appearance of Hairline Crack at the Surface of Heat-Treated Concrete Specimen with High Potassium at Age 357 days

#### 9.2- Weight Change Measurement

The weight of specimen was measured every time just after their length was measured for expansion in order to ensure consistency of the measuring techniques. Weight changes for all the specimens followed the same pattern as length change. Weight change of concrete specimens is shown in Figure 9-6 where each point is the average result of the 5 specimens of the corresponding set. Overall, specimens with high potassium displayed the greatest weight gain followed by those with normal potassium heat-treated. At 21 days the weight gain were 0.11%, 0.012% and 0.023% respectively for heat-treated specimen, heat-treated with high potassium and control. All specimens showed a rapid weight gain from the beginning of the experiment to around 60 days. The rapid weight gain observed in the early days of the experiment can be attributed to the water filling the pores and cracks. Then the gain slowed down and picked up again at around 120 days for heat treated specimens while the slow down continued for control specimens. This permanent weight gain in heat-treated specimens can be associated with formation of a phase that require water uptake like ASR or ettringite as observed by Ceesay (Ceesay, 2007). The maximum weight changes at the

end of the experiment were 1.33% for heat treated specimen with normal potassium, 1.92% for heat-treated specimens with high potassium and 0.45% for control at age 337 days. Weight change measurements were stopped at the same time with length measurement, i.e. once the heat-treated specimen with high potassium started displaying hairline cracks (Figure 9-5).

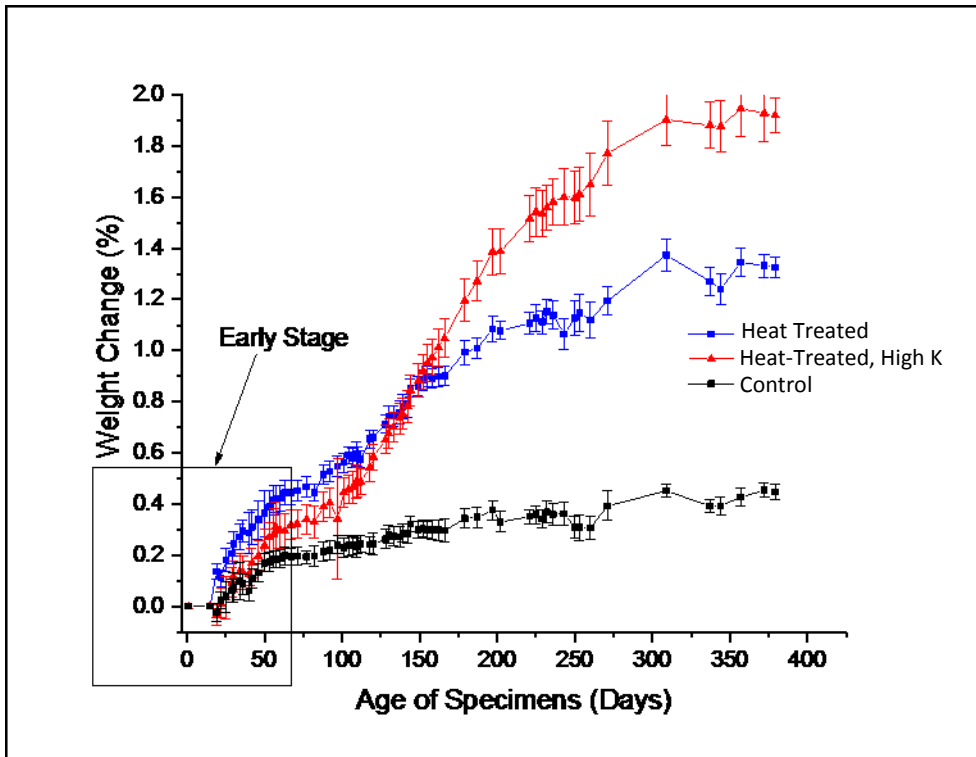


Figure 9-6: Plot of Weight Change VS Age of Concrete Specimens

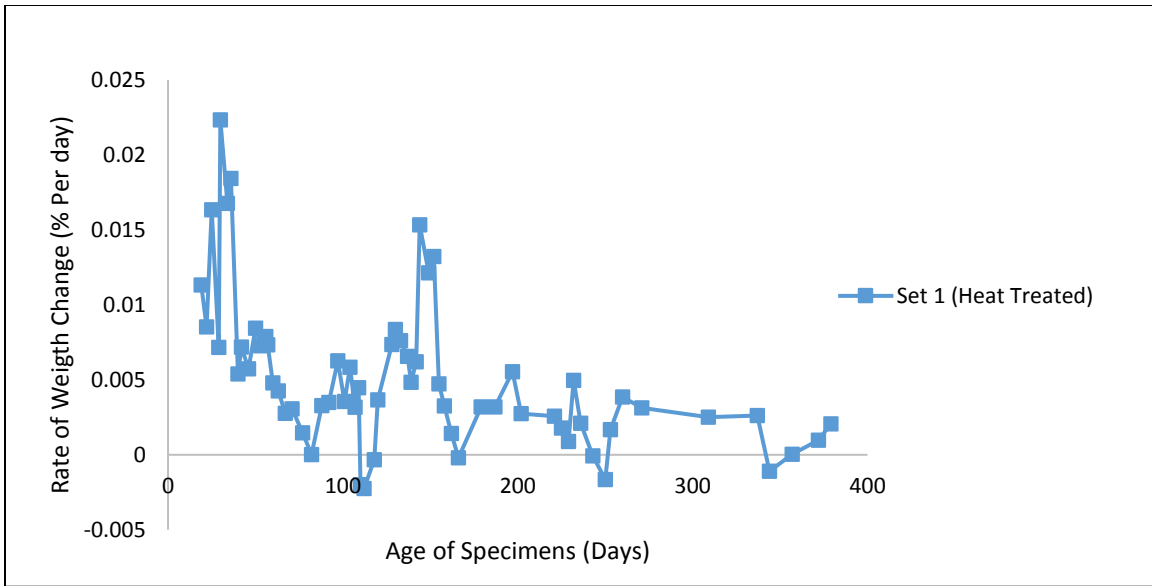


Figure 9-7: Rate of Weight Change for Heat-Treated Specimens with Normal Potassium

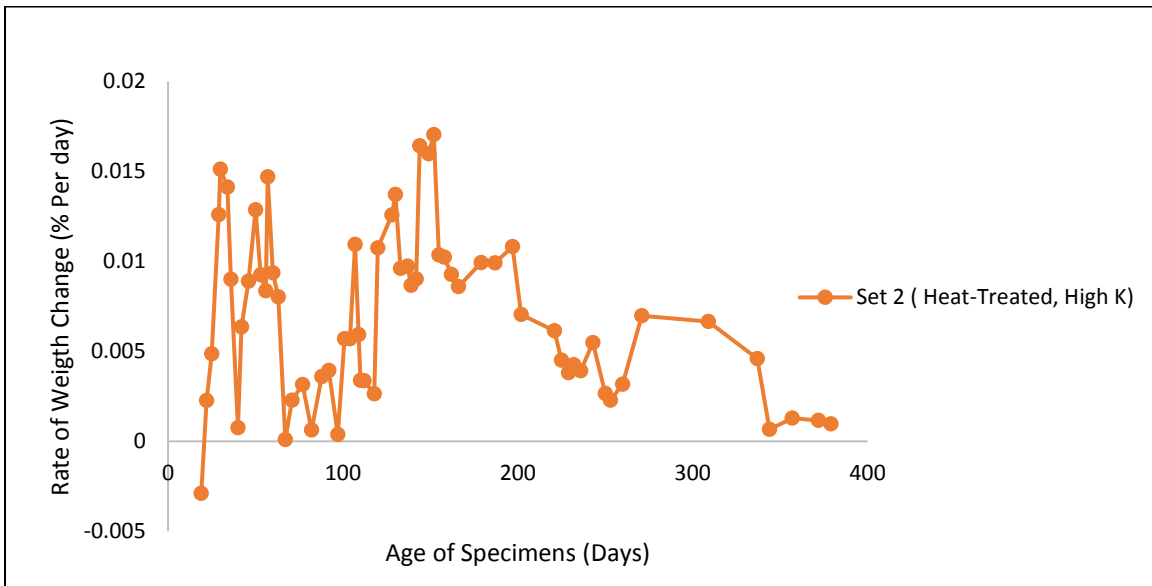


Figure 9-8: Rate of Weight change of Heat-Treated Specimens with High Potassium

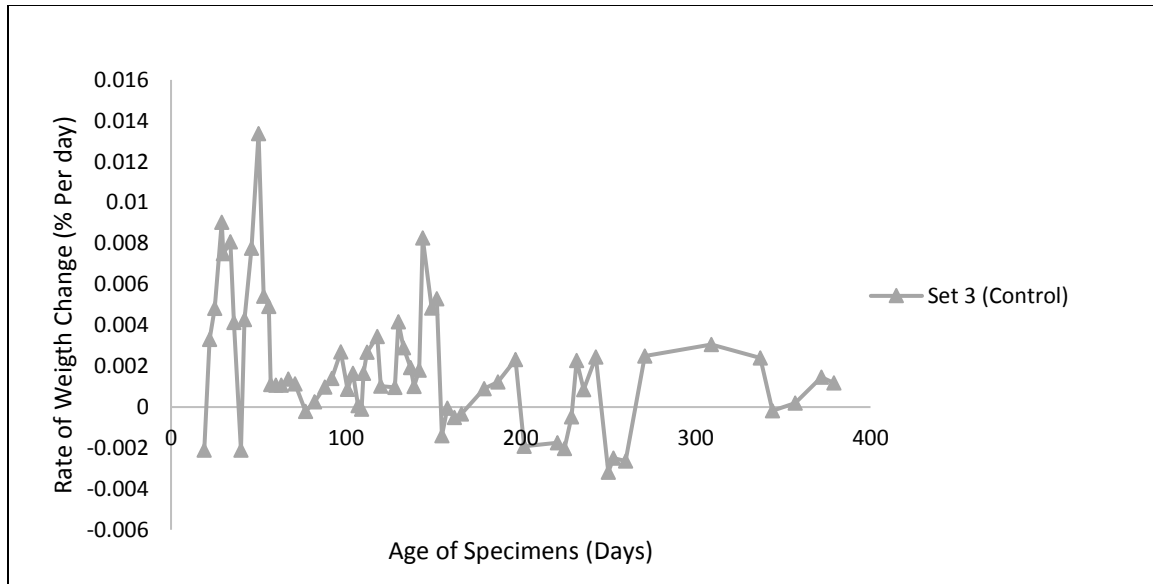


Figure 9-9: Rate of Weight Change for Control Specimens

### 9.3- Compressive Strength Results

The first compressive strength test was carried out at the end of the heat cycle and prior to the immersion of all the specimens in lime water for storage. The average compressive strength prior to immersion in saturated lime water were 3915 psi, 2860 psi and 6644 Psi respectively for specimen with normal level of potassium heat-treated, high potassium heat-treated and control. Figure 9-10 is a plot of the average compressive strength of the concrete specimens. Throughout the experiment, control specimens exhibited the highest average compressive strength. The low strength observed for heat-treated samples at early age can be explained by the fact that heat cycle and addition of potassium had already a deleterious effect on the concrete. The Peak occurs at 83 days for heat-treated sets (4321 Psi for normal potassium and 2835 Psi for high potassium) while the peak occurs for the control specimens at 120 days (7955 Psi). Even though the decline observed after the peak for all heat-treated specimens was predictable, the decline for control specimen was not expected. It can be explained by the fact that storage in saturated lime water is also a

condition that promotes development of late ettringite in concrete as has been shown in numerous studies (Ceesay, 2007). The decline in the compressive strength of heat-treated specimens was more pronounced with up to 50% for high potassium specimens and 28% for the ones with normal level of potassium, while it was only 16% for the control specimens.

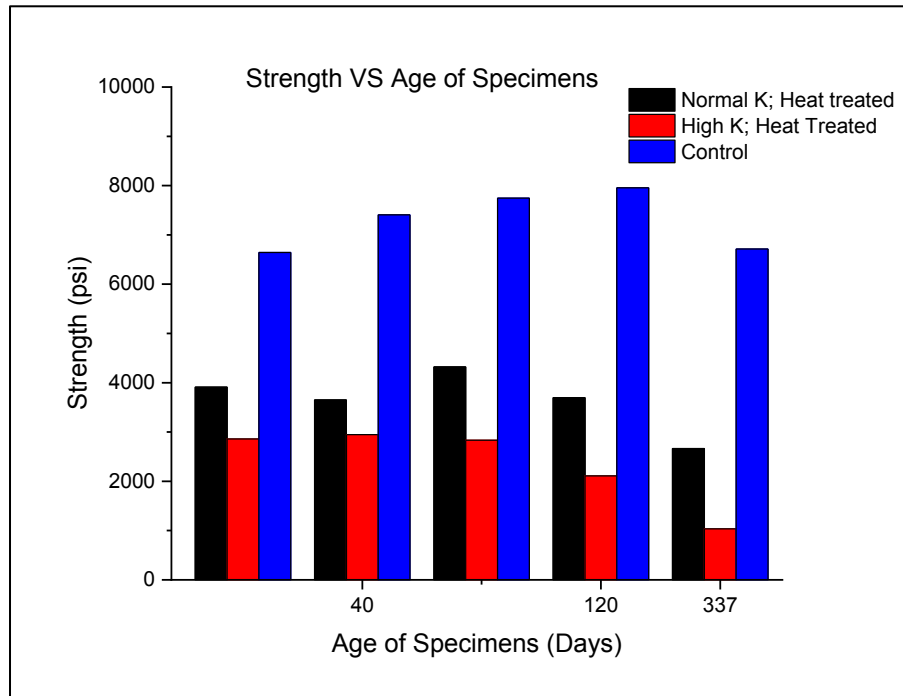


Figure 9-10: Plot of Compressive Strength of Concrete Specimens

Table 9-1: Average Compressive Strength of Concrete Specimens

Average Compressive Strength (Psi)						
age (Days)	Set 1 (Heat)		Set 2 (Heat+K)		Set 3 (Control)	
	STR	Std	STR	Std	STR	Std
0	3912	152	2860	360	6644	227
40	3651	310	2946	62	7408	113
83	4321	98	2835	300	7746	90
120	3695	429	2111	154	7955	29
337	2665	303	1036	398	6714	887

STR: Compressive Strength  
Std: Standard Deviation

#### 9.4- Scanning Electron Microscopy with Energy Dispersive X-ray Analysis

Scanning Electron Microscopy (SEM) with Energy Dispersive X-ray Analysis (EDAX) was used in the study in order to determine the chemical composition of the expansive phase at the aggregate/Paste interface in concrete specimens at various ages. The presence of ettringite and the morphology (the shape and size) of ettringite crystals were our main focus. On the EDAX, each of the common expansive phases found in concrete has a specific footprint. Ettringite, which is of interest in this study, has a very distinct output with three distinct stair step peaks of Aluminum (Al), Sulphur (S) and Calcium (Ca). Figure 9-11 shows a typical EDAX output identifying ettringite. The criterion for ettringite is based on the ratio of Ca, S and Al and a rule of thumb is 6:4:2.

Quantitative results of the chemical composition from EDAX of concrete samples were used to build ternary diagrams with ratios of Al, S and Ca normalized to 100% stoichiometric ettringite. The ratios in monosulfate ( $3\text{CaO}\cdot\text{Al}_2\text{O}_3\cdot\text{CaSO}_4\cdot 12\text{H}_2\text{O}$ ) was also plotted and used for comparison.

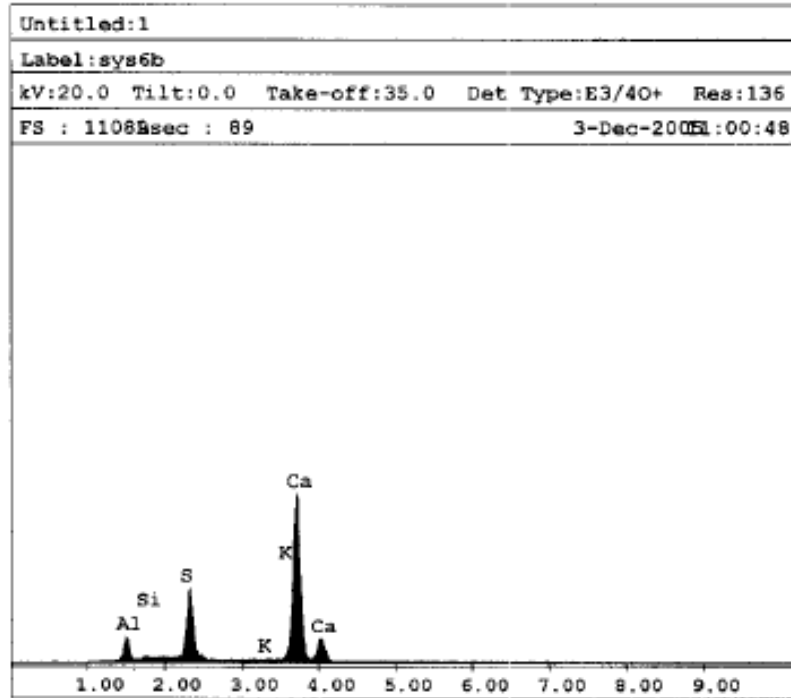


Figure 9-11: Typical Output of EDAX of Ettringite with the Characteristic Step Model of Al, S and Ca (Source: Ceary, 2007)

#### 9.5.1. Heat-treated Specimens with Normal Level of Potassium.

SEM of the aggregate/ paste interface at 40 days showed early stages of ettringite with the formation of clusters of sphere-shape ettringite crystals and patches of calcium hydroxide layering the interior of air voids and cavities as shown in Figure 9-12. EDAX of the sphere provided the following chemical composition by weight of Al= 1.72%, Si= 3.28%, S=2.39% and Ca=26.01 %.

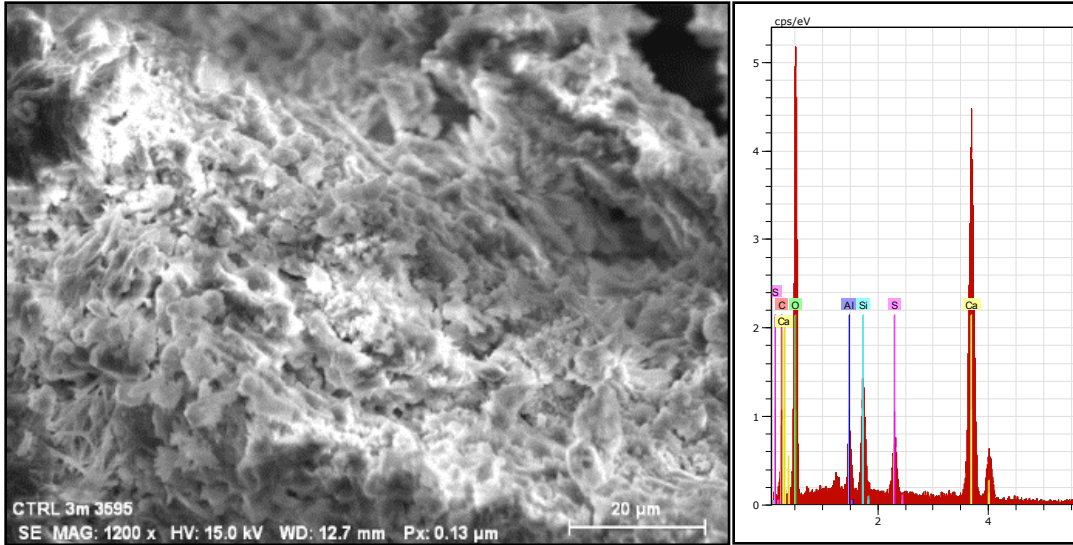


Figure 9-12: SEM Image and EDAX Plot of Heat-Treated Specimens with Normal Level of Potassium at 40 days, Showing Sphere-Shape Ettringite Particles Layering the Interior of an Air Void at The Aggregate/Paste Interface

At age 83 days, SEM of the interior of a void at the interface of paste and aggregate shows clusters of needle-like particles tipped with spherical ettringite balls (Figure 9-13). Chemical analysis through EDS of those particles provides the following composition by weight: Al = 4.06%, Si = 2.06%, S = 7.41% and Ca = 27.50%, which is characteristic of ettringite. This suggests that ettringite goes through a morphological transformation from crystal balls to needle like crystals.

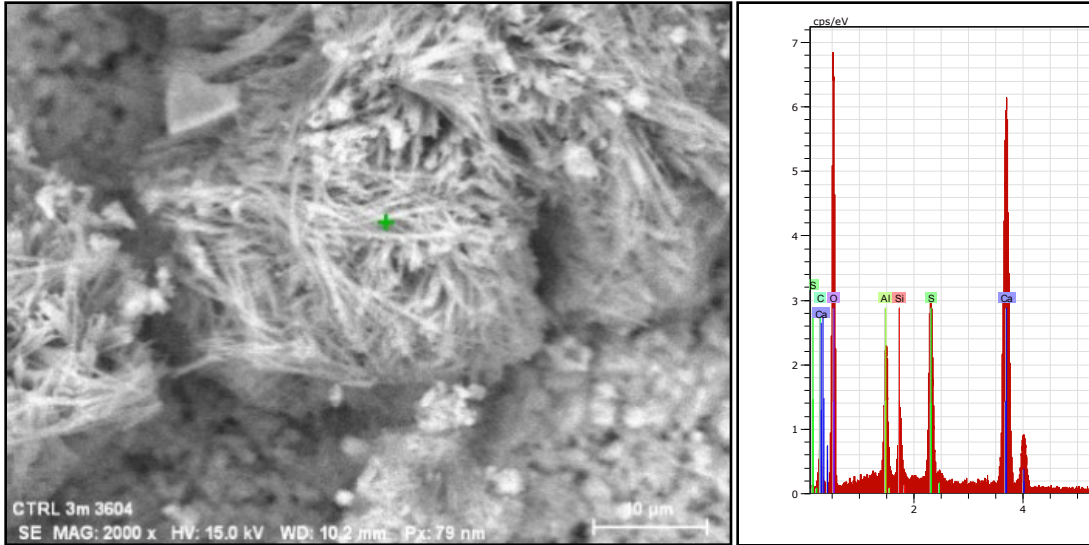


Figure 9-13: SEM and EDAX of Heat-Treated Specimens with Normal Potassium at 83 days Showing Clusters of Needle-Like Ettringite Particles in a Void at the Aggregate /Paste Interface

At 120 days, voids at the interface of the aggregate and paste are partially filled with needle-like ettringite particles with carbonate spherical balls at their tips. Elemental composition analysis of the needle provides the following composition: Al = 2.90%, Si = 4.95%, S = 3.28% and Ca = 32.21%, while analysis of the balls shows: Al = 1.61%, Si = 2.83%, S = 1.69% and Ca = 27.63. At this age, the filling of the void is more pronounced than at age 40 days.

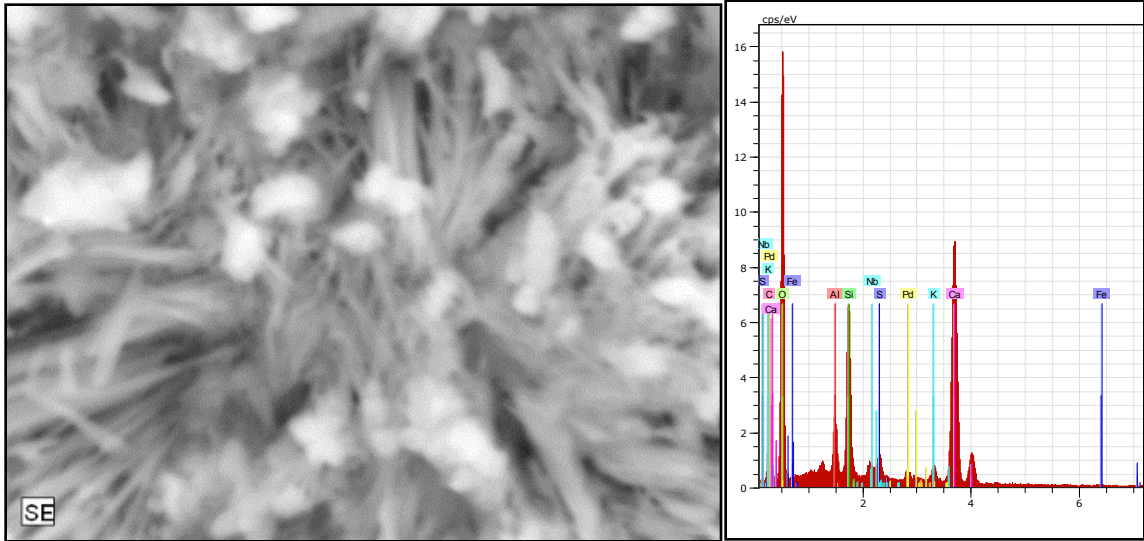


Figure 9-14: SEM and EDAX of Heat-Treated Specimens with Normal Level of Potassium at 120 Days Showing Needle-Like Ettringite Particles and Calcium Carbonate Balls in a Void at The Aggregate/Paste Interface

At age 337 days; SEM of voids located at the interface of aggregate and paste are filled with particles having the same morphology as those found at age 120 days. Analyzing these needles with EDAX provided the following composition: Al = 2.74%, Si = 1.46%, S = 3.82 % and Ca = 25.07%.

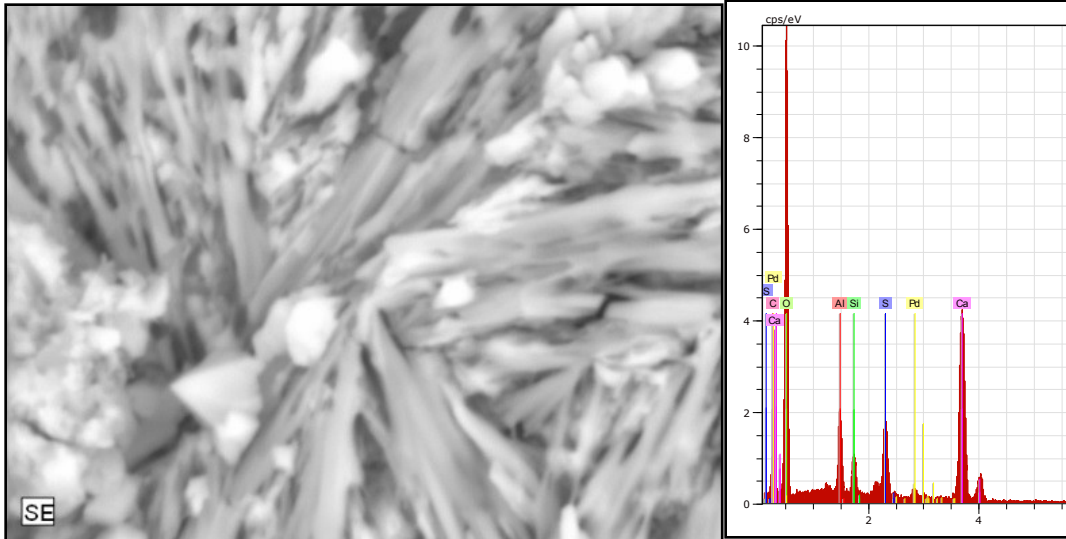


Figure 9-15: SEM and EDAX of Heat-Treated Specimen with Normal Potassium at 337 Days Showing ettringite Needles and Carbonate Calcium Balls

The ternary plot of Figure 9-16 shows how the composition of the particles found in the void evolves from the first scan (Set 1-2) to the last one (Set1-5) and how it compares to pure ettringite, monosulfate and calcium aluminum. Based on this, it can be seen that the stoichiometric composition of the expansive phase found tends to migrate towards pure ettringite and monosulfate.

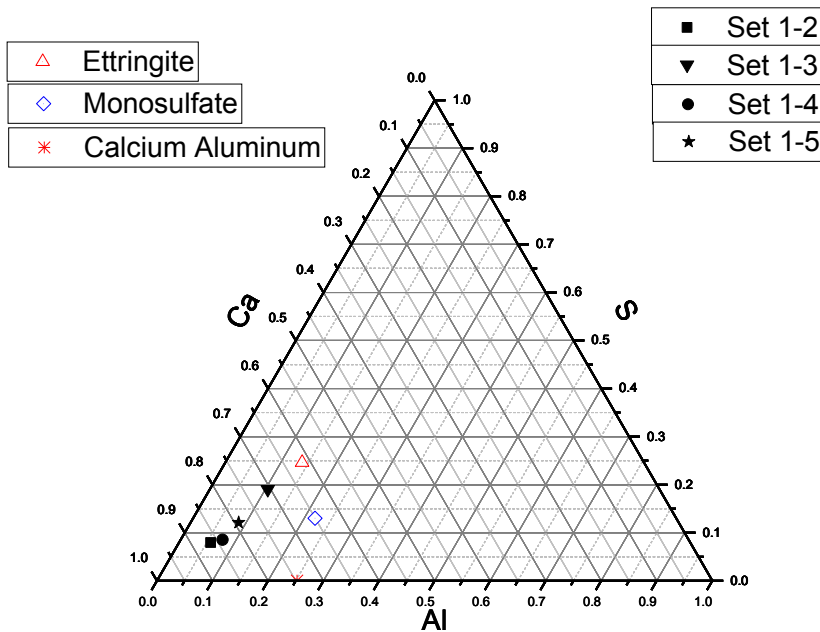


Figure 9-16: Ternary Plot of Al-Ca-S for Particles in Void at the Aggregate/Paste Interface of Heat-Treated Specimens with Normal Potassium

### 9.5.2. Heat-Treated Specimens with High Potassium

At early age (40 days) SEM of voids at the interface of the paste and the aggregate indicate a material deposit forming clusters of ettringite lamellae and some calcium hydroxide particles. EDAX analysis of one of those clusters provides the following elemental composition by weight: Al = 2.64%, S = 5.0% and Ca = 23.56 % which is characteristic of ettringite.

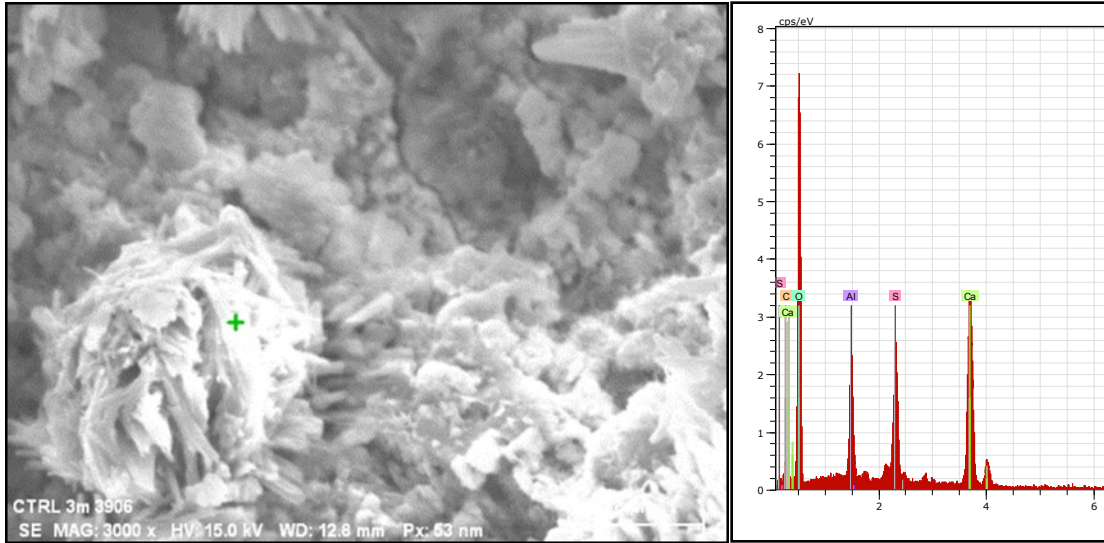


Figure 9-17: SEM and EDAX of Heat-Treated Specimen with High Potassium at 40 Days showing Clusters of Ettringite lamellae in a void at the Aggregate/Paste Interface

At 83 days, observation of the interior of an air void at the interface of the aggregate and paste shows sphere-shape clusters of ettringite needles in voids (Figure 9-18). Calcium carbonate was also observed in the pores and it is suggested that it is the product of decomposition of calcium hydroxide due to exposition to air of the samples. EDAX of the lamellae provides the following elemental composition by weight: Al = 1.97%, Si = 5.12%, S = 3.60% and Ca = 32.62% which is typical for ettringite.

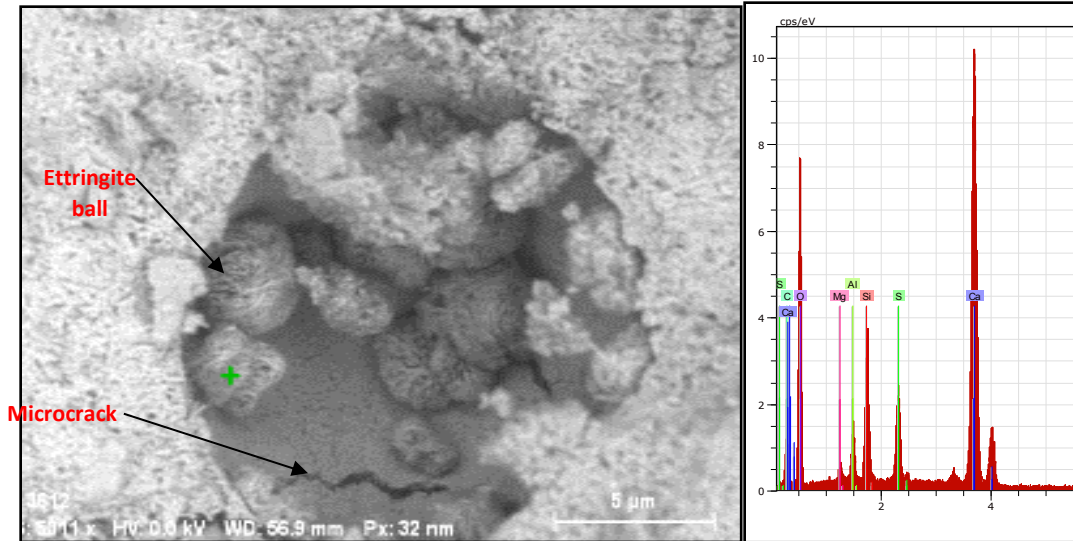


Figure 9-18: SEM and EDAX of Heat-Treated Specimens with High Potassium at 83 days Showing Sphere-Shape clusters of Ettringite Needle in void at the Aggregate/Paste Interface. A Microcrack is Also Visible.

Analysis of a specimen at 120 days showed that voids are densely filled with needle-like crystals of ettringite. EDAX of a needle provides the following elemental composition by weight: Al = 2.35%, Si = 1.25%, S = 3.28% and Ca = 21.50%.

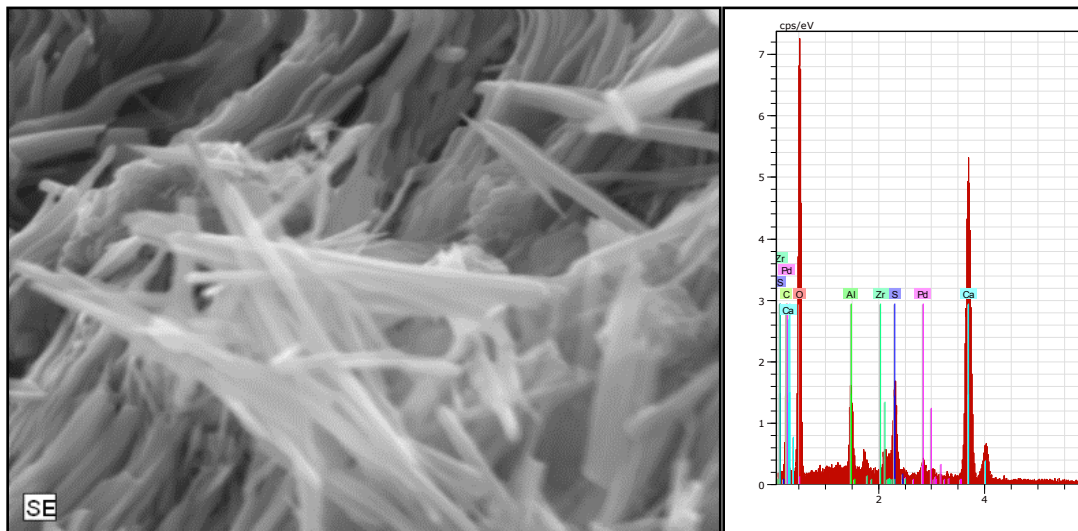


Figure 9-19: SEM and EDAX of a Heat-Treated Specimen with High Potassium at 120 Days showing needle-like Ettringite crystals in a Void at the Aggregate/Paste interface

At age 337 days, dense ettringite needles along with plate shape particles of monosulfate can be observe in voids at the interface of paste and aggregate (Figure9-20). The elemental composition of the needle through EDS shows: Al = 3.62%, Si = 1.41%, S = 5.34% and Ca = 25.63% while analysis of a plate shape particle provides the following mass composition: Al = 2.01%, S = 2.84% and Ca = 26.03%.

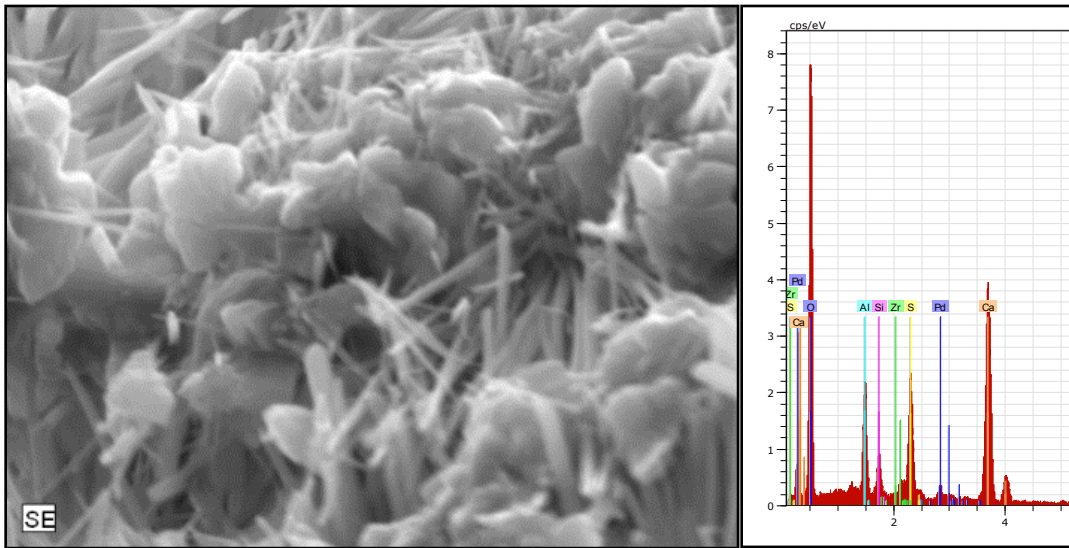


Figure 9-20: SEM and EDAX of Heat-treated Specimens with High Potassium at 337 Days Showing Dense needle Crystal of Ettringite and Plate Shape Crystals of Monosulfate in Void at the Aggregate/Paste Interface

The ternary plot of Figure 9-21 represents evolution of the composition of the particles found in the void from the first scan (Set 2-2) to the last one (Set 2-5) and how it compares to pure ettringite, monosulfate and calcium aluminum. The stoichiometric composition of the expansive phase found is concentrated around pure ettringite and monosulfate. It is also seen that the composition tends to move towards that of pure ettringite as time passes.

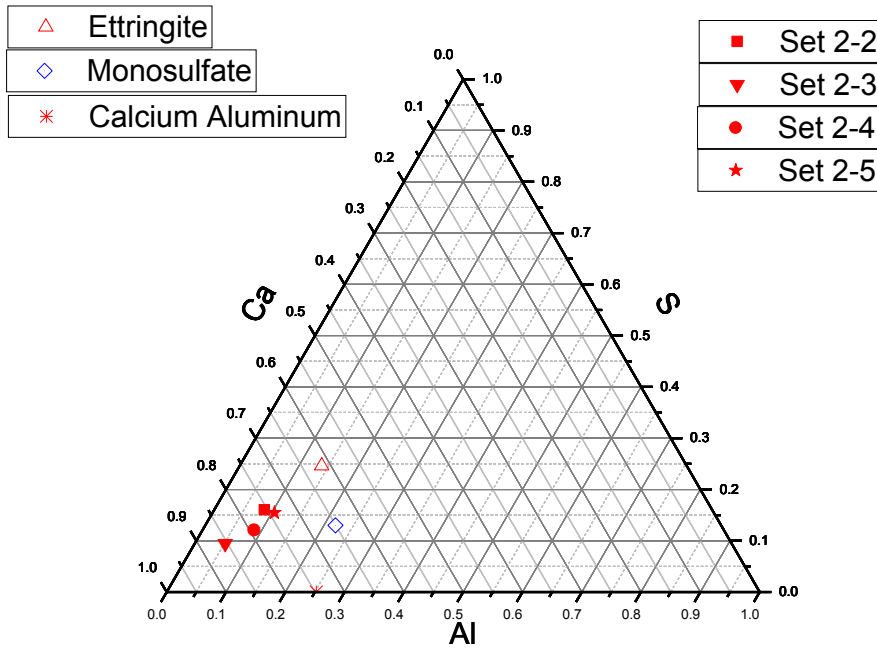


Figure 9-21: Ternary Plot of Al-Ca-S for Particles in Void at the Aggregate/Paste Interface of Heat-Treated Specimens with High Potassium

### 9.5.3. Control Specimens

At 40 days, voids located in the interfacial transition zone contain grain like particles of calcium hydroxide Figure 9-22. Analysis of a grain by EAX provides the following elemental composition by weight 34.29% of calcium (Ca) with total absence of aluminum (Al) and Sulphur (S).

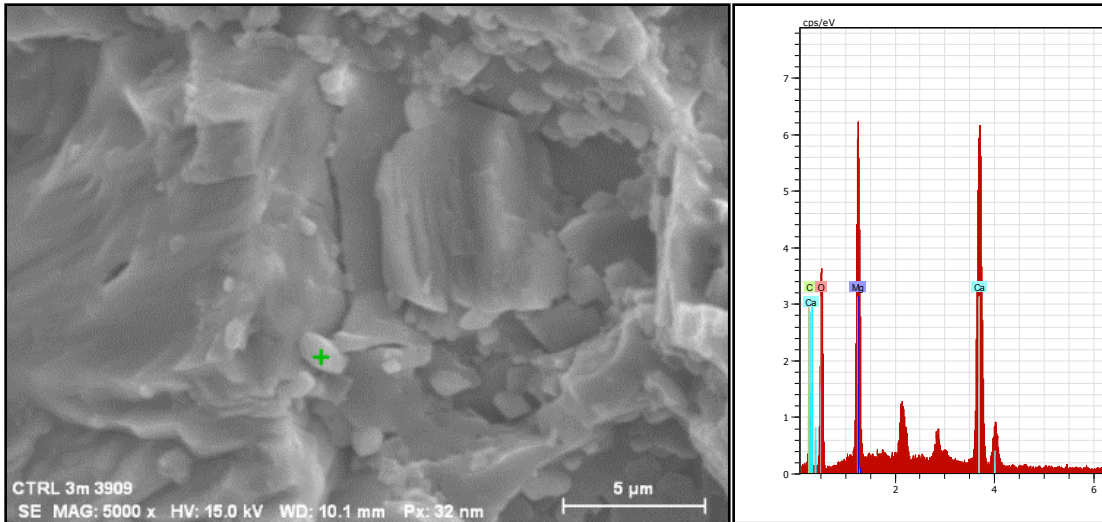


Figure 9-22: SEM and EDAX of Control Specimens at 40 Days showing grain Particles of Calcium Hydroxide in Void at the Aggregate/Paste Interface

83 days after casting, SEM did not show ettringite in void at the interface of aggregate and paste, which is proven by the absence of Sulphur in the EDAX analysis results. Crystals of calcium carbonate were found (Figure 9-23). The calcium carbonate is formed by carbonation of calcium hydroxide due to exposure of the samples to air after the concrete specimens were broken. The high peak silicon (Si) in the EDAX revealed the early presence of calcium silicate hydrate C-S-H, which will later be converted to ettringite as water became predominantly available. The elemental composition by weight of crystals found in the sample was as follows: Al = 0.59%, Si = 3.51 % and Ca = 32.01%.

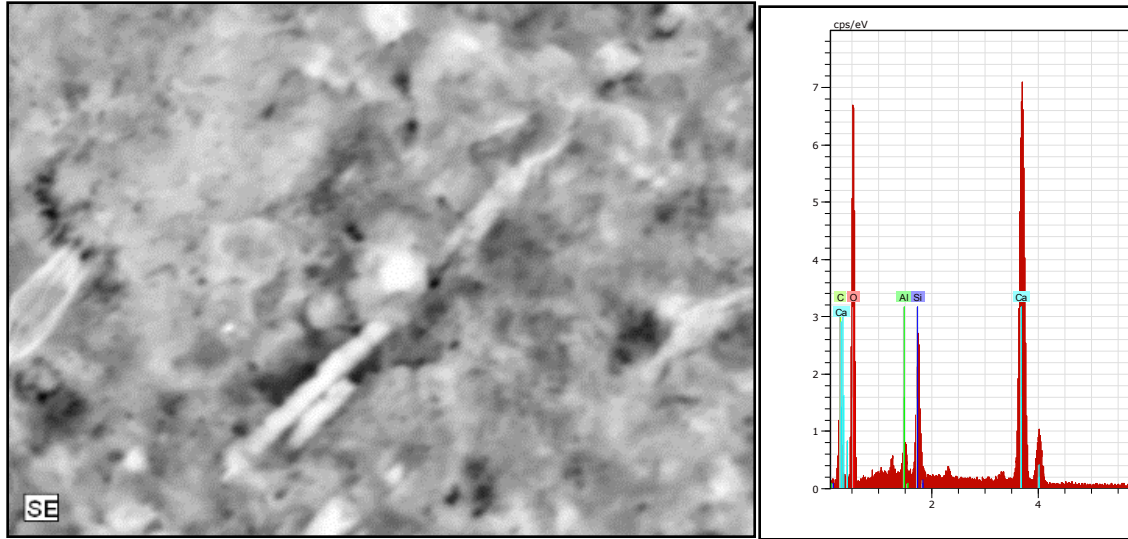


Figure 9-23: SEM-EDAX of Control Specimen at age 83 Days Showing Spars Crystals of Calcium Carbonate in Void at the Aggregate/Paste interface

SEM observation of samples taken from specimen at 120 days showed the presence of thin crystal needles of ettringite along with crystals of calcium carbonate (Figure 9-24) formed by carbonation of calcium hydroxide due to exposure of samples to air. The ettringite crystal morphology observed could not be confirmed by EDAX elemental composition. The composition by weight provided was: Al =2.83%, S =0.80%, Si = 6.83 % and Ca = 33.89%.

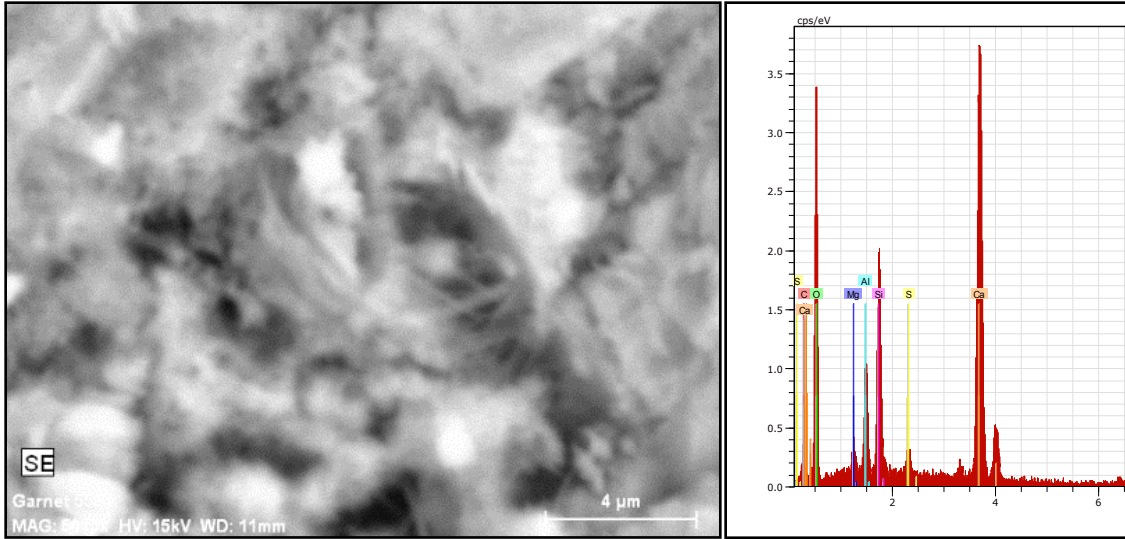


Figure 9-24: SEM-EDAX of Control Specimen at 120 days Displaying Thin Needle-like Ettringite Crystals and Calcium Carbonate Particles in Voids at the Aggregate/Paste Interface

The SEM samples at 337 days contained long crystals needles of ettringite filling 5 to 10% of the void at the interface of aggregate and paste. It also reveals the presence of Calcium carbonate in blob shape (Figure 9-25). EDAX confirmed ettringite and provided chemical composition of Al = 2.37%, Si = 1.48%, S = 4.12% and Ca = 29.87% which is typical for ettringite. Crystals of calcium carbonate were probably the product of carbonation of calcium hydroxide.

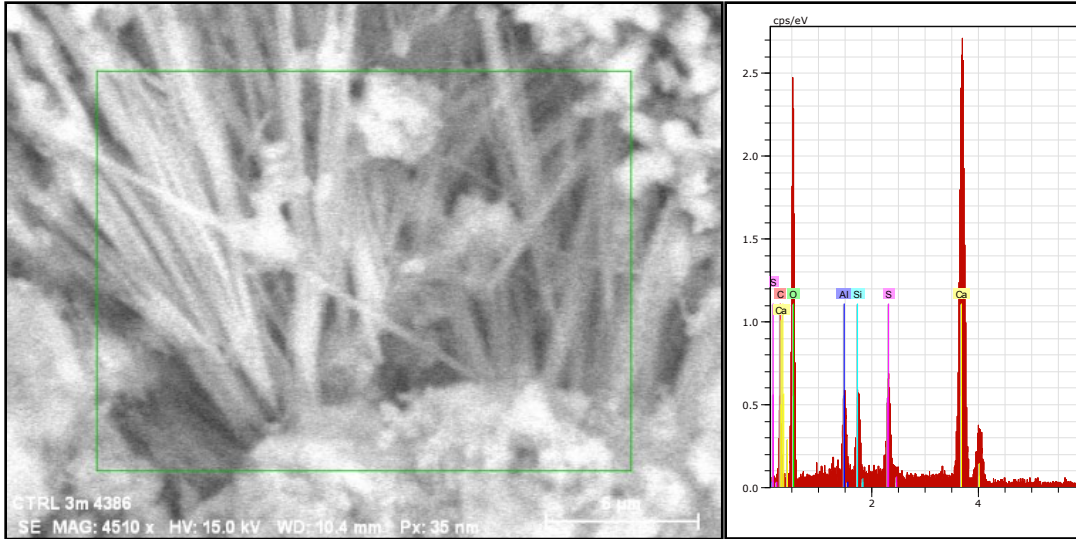


Figure 9-25: SEM-EDAX of Control Specimens at 337 Days Showing Needle Like Ettringite Crystals and Blobs Crystals of Calcium Carbonate in Voids at the Aggregate/Paste Interface

The ternary diagram of atomic ratio of Ca, Al and S of Figure 9-26 shows that the composition of material filling the voids seems to diverge from ettringite and monosulfate for the control specimens. The material was richer in Ca but poorer in Al and S.

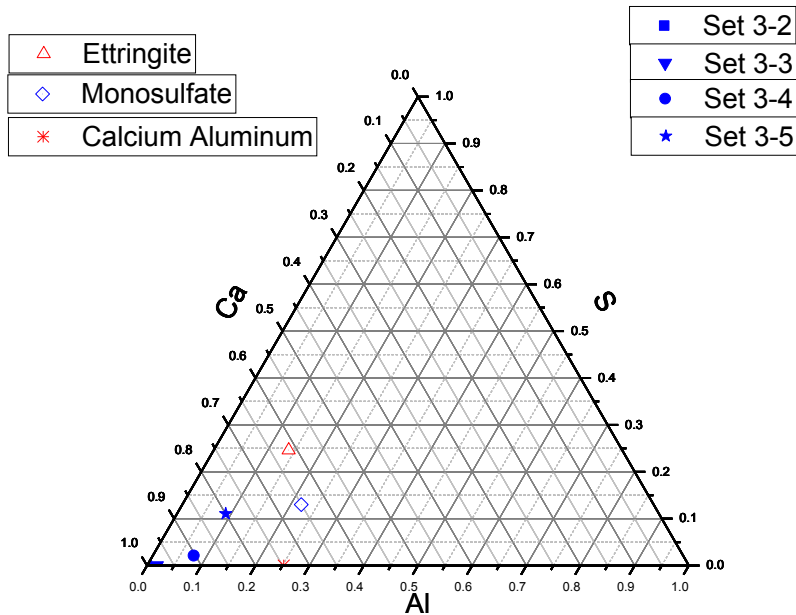


Figure 9-26: Ternary plot of Al-Ca-S for Particles in Void at the Aggregate/Paste Interface of Control Specimens

### 9.5- Summary on Conventional Measurement and SEM

From conventional testing methods and SEM-EDAX a certain number of observations were made: heat-treated concrete specimens with high potassium showed the highest overall expansion and weight gain, while the control specimens showed little to no expansion or weight change. Heat-treated specimens experienced drastic decline of their compressive strength over time, which was more pronounced for those with high potassium. Ettringite along with calcium carbonate were found in voids located at the aggregate/ paste interface in heat treated specimens at early age but at a later age for control specimens. The morphology of ettringite found evolved throughout the experiment from sphere-shape ettringite crystals to clusters of thin ettringite needles to lamellar particles and thick individual needle-like crystals directed in the same direction at the end. Table 9-2 summarizes the results of SEM and EDAX tests. Ternary plots of atomic ratios of Ca,

Al and S show a wide variability and differ sometimes significantly from pure stoichiometric ettringite. Many reasons can be incriminated:

- Experimental errors which are due partly to the lack of a plane surface for the SEM since the fracture sample method was used, less than ideal orientation of the sample surface with regard to the incident electron beam. (the ideal incident angle is around 30°).
- The Deviation from the pure stoichiometric composition of the ettringite can also be partly attributed to the isomorphous substitution of elements that sometimes occur, such as  $\text{SiO}_4^{4-}$  for  $\text{SO}_4^{4-}$  in the ettringite lattice (Thaulow *et al.*, 1996).
- Sampling errors can also be one of the reasons because there was just a limited number of samples selected and selection was not random.

Table 9-2: Summary of SEM/EDAX Results Showing Morphology of Ettringite and Other Phases Found in Voids of Specimens at Various Age

		Heat Treated	Heat Treated + K	Control
SEM/EDAX Analysis	40 Days	Spherical balls of ettringite crystals	Cluster of lamellae shape ettringite crystals	No ettringite, Calcium Hydroxide
	83 Days	Cluster of Needle-like Ettringite crystals	Cluster of Needle-like Ettringite crystals	No Ettringite, Calcium Carbonate
	120 Days	Ettringite needles + Calcium Carbonate particle	Ettringite needles	Thin ettringite needles
	337 Days	Ettringite needles + Calcium Carbonate particle	Ettringite needles and plates	Ettringite Needles and calcium Carbonate

#### 9.6- Computed Tomography Results

Analysis of computed tomography data was mostly qualitative and was based on observation of monomodal data, observation of neutron versus X-ray volumes on a slice

by slice basis and observation of segmented fused volume. Observation was aimed at identification of voids, microcracks patterns and potential ettringite particles.

#### 9.6.1. Single Modal Observation of Cracks Growth and Propagation

X-ray reconstructed images were more suited for observation of cracks since they would appear as dark lines. Images of specimens from both sets of heat-treated specimens showed multiple visible microcracks appearing as early as at the third scan, i.e. at age 66 days. Some of those cracks seemed to show growth over time (Figure 9-27) while new cracks appeared (Figure 9-27 and 9-28).

It was also observed that many of these cracks are developed around aggregates.

Observation of images from control specimens shows a few cracks towards the end of the experiment (Age 230 days). (Figure 9-29).

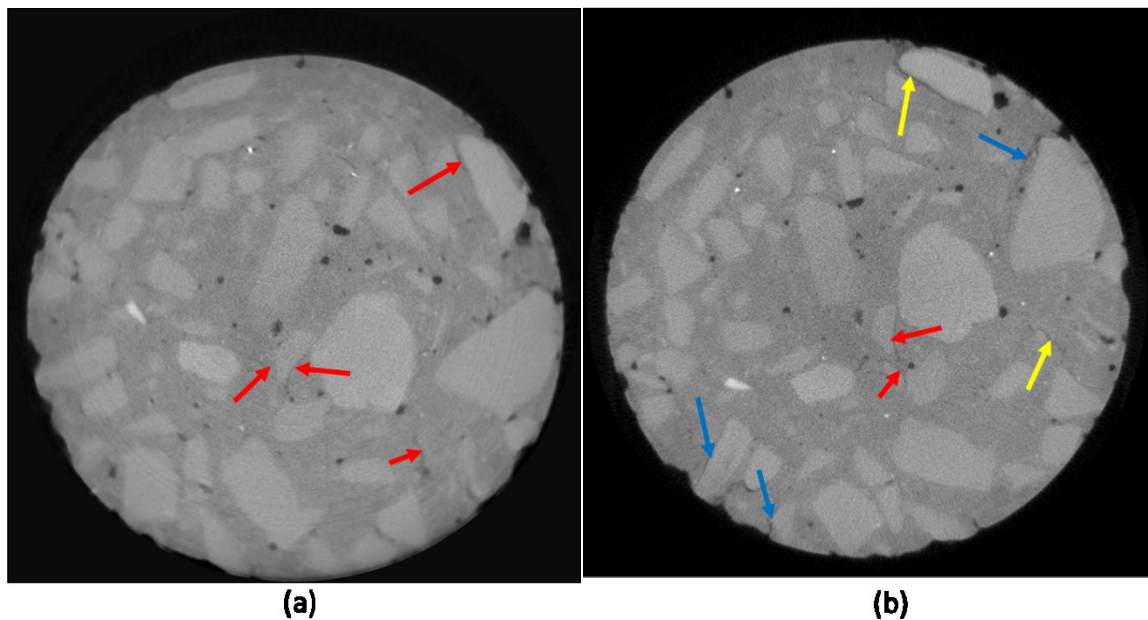


Figure 9-27: X-ray slice of heat-treated specimen with normal potassium at age 102 days (a) and at age 230 days. Red arrows show initial cracks, yellow arrows indicate existing cracks growth and blue arrows indicate new cracks.

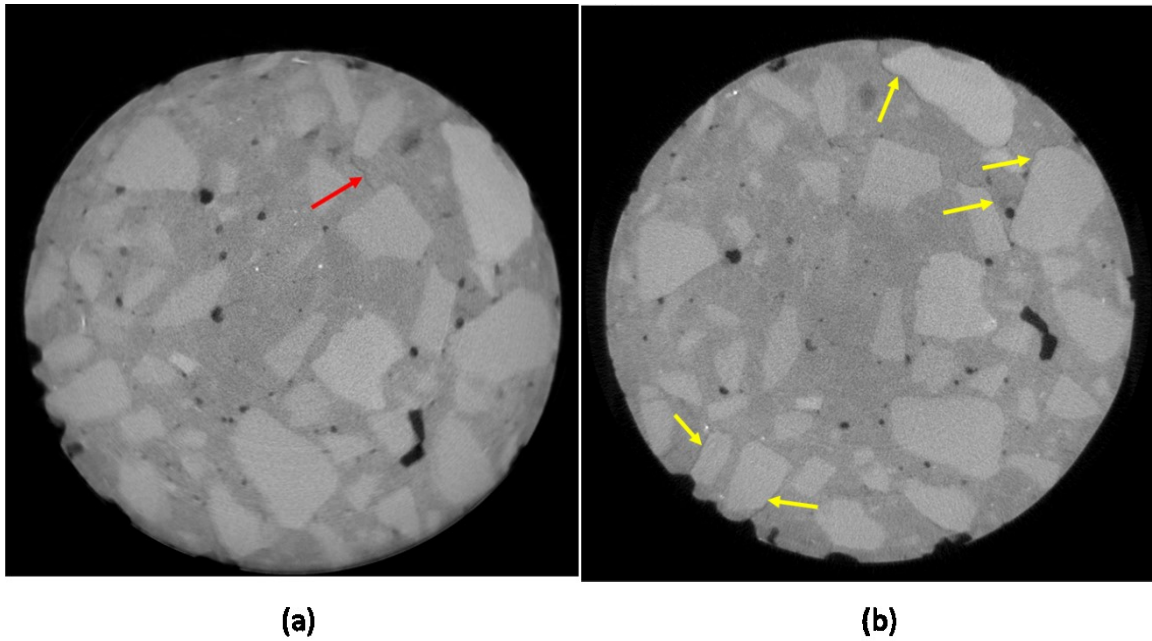


Figure 9-28: X-ray slice of heat-treated specimen with high potassium at age 102 days (a) and at age 230 days. Red arrows show initial cracks, yellow arrows indicate new cracks.

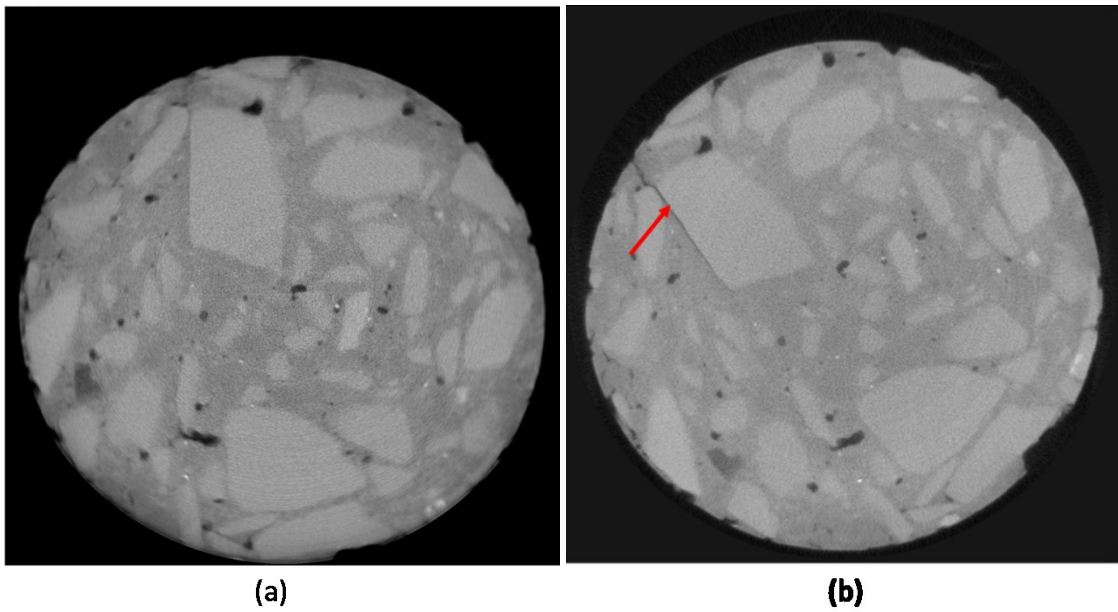


Figure 9-29: X-Ray Slice of Control Specimen at Age 102 Days (A) and at Age 230 Days. Red Arrows Show Late Stage Crack Appearance.

### 9.6.2. Dual-Modal Observation

Neutron volumes at various ages were compared to corresponding X-ray volumes in order to identify potential similarities and differences. The phases that were of particular interest in the analysis were voids, microcracks, water and possible ettringite. Since both modalities used in the study are complementary each of these phases would have different appearance for each modality.

- Cracks filled with air, water or ettringite would appear darker on X-ray slices since those phases have very low X-ray attenuation factors.
- Water and ettringite would appear brighter on neutron slices.

Dual- modal contrast of neutrons and X-rays is presented in Figure 9-30, corresponding to the cross-sectional comparison presented in Table 5-8. Pores and cracks show good enough contrast in the X-ray slices to be distinguished easily, however the material (if any) filling those pores cannot be identified from the X-ray tomography slices. In addition, there is not enough contrast between the paste and aggregates in the X-ray slices even though the edges of aggregates are very distinctive. On the other hand, there is good contrast between the paste and aggregates in the neutron slices but not enough contrast between the pores and the paste. By comparing the two images, it appears that some of the areas identified on the X-ray as voids or cracks appear brighter on neutron images, which is characteristic of ettringite or water, meaning that those pores and voids are filled with water or potential ettringite. Such areas were found mostly on heat-treated specimens starting at age 66 days.

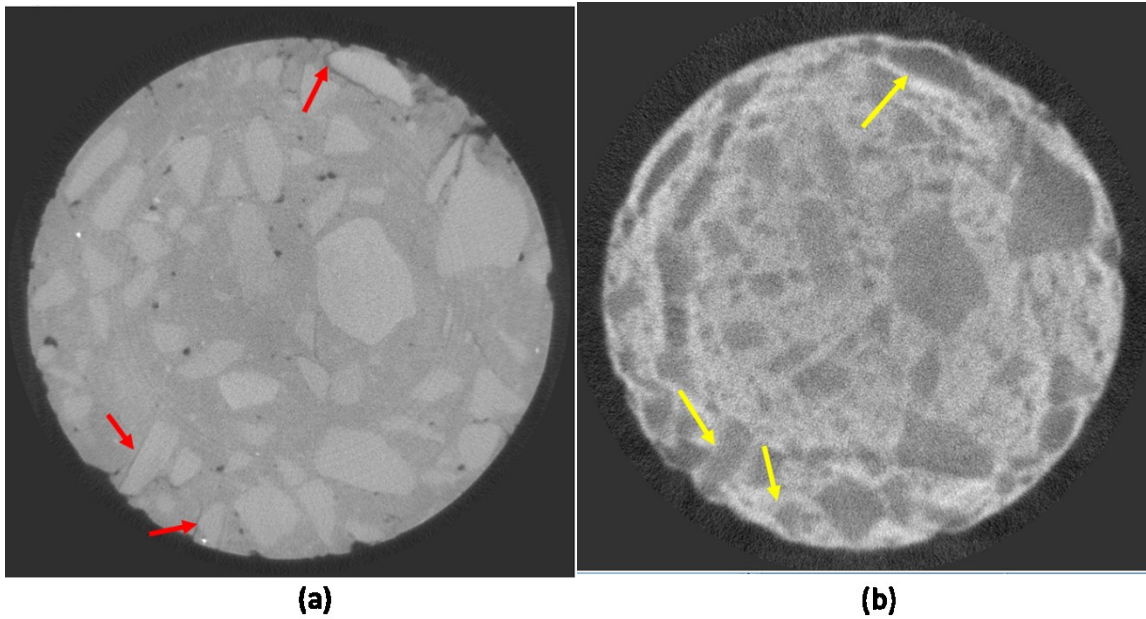


Figure 9-30: X-ray (a) and Corresponding Neutron Slice (b) of Heat-Treated Specimens at Age 230 Days. Arrow in Red Indicate Cracks on X-ray slices that Appear Bright in Neutron Slice (Yellow Arrows) Meaning Water or Ettringite Filling.

### 9.6.3. Segmentation

Segmentation of different volumes allowed for identification of various concrete phases including the potential presence of ettringite. It was also possible to obtain stacks representing each of the phases separately. Each of the stacks could then be rendered into a 3D image (Figure 9-33 to Figure 9-35). The segmented images showed:

- Segmentation did not allow visualizing microcracks due to the resolution and the uncertainties associated with the segmentation, only large cracks were visible at late stage on all three sets of specimens.
- Potential ettringite was observed in pores of heat-treated specimens starting at 102 days of age (Figure 9-31 and Figure 9-32).
- Ettringite was also observed in pores of control specimens at late stage; however, the degree of pore filling seems to be less than that of heat-treated specimens.

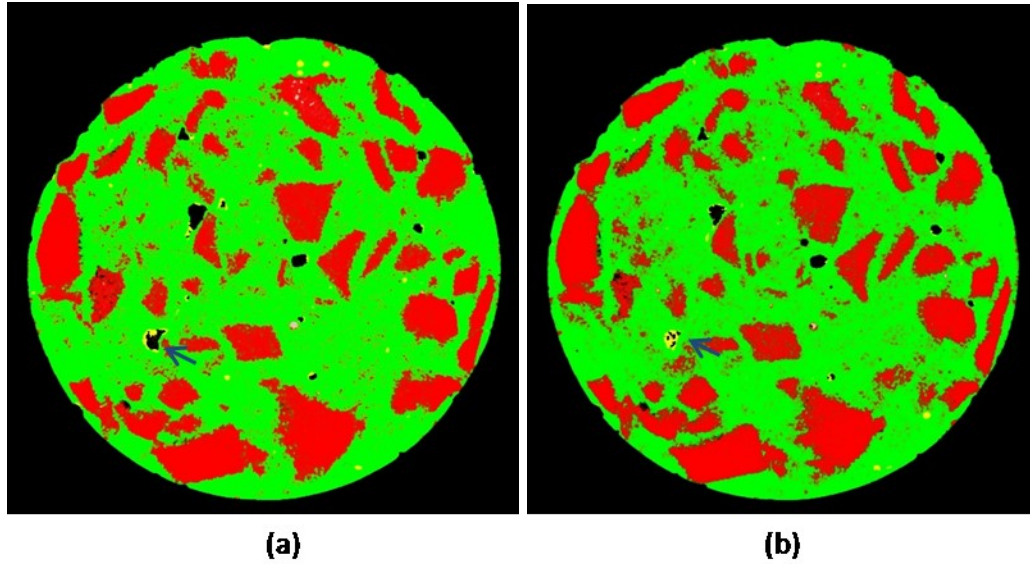


Figure 9-31: Segmented fused CT Slice for Heat-treated Specimen with Normal Potassium at Age 102 Days (a) and 230 Days (b). The Blue Arrow Indicates Pores Ettringite Filling (yellow)

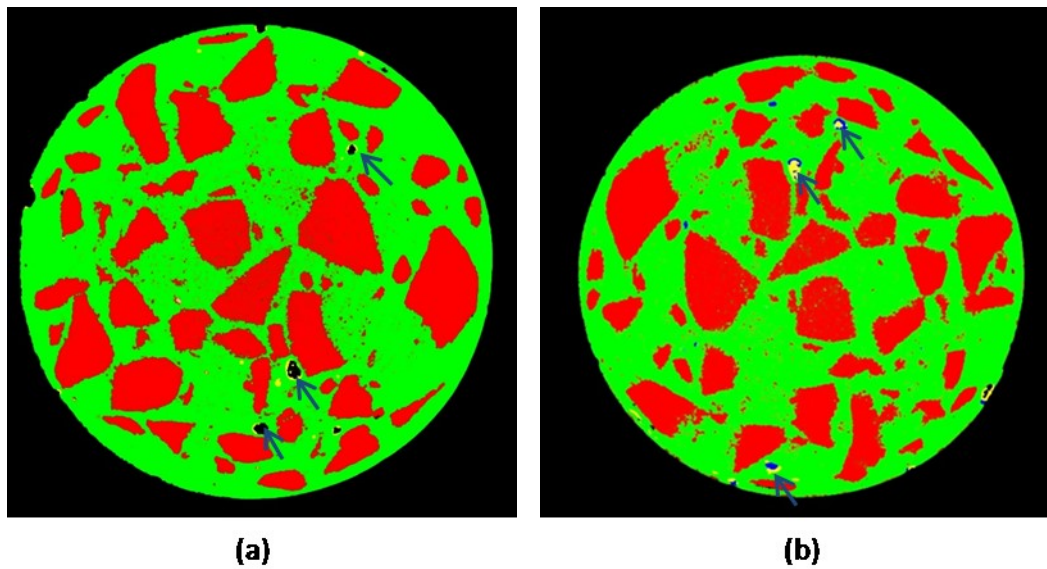


Figure 9-32: Segmented fused CT Slice for Heat-treated Specimen with High potassium at age 102 Days (a) and 230 Days (b). The Blue Arrow Indicates Pore Ettringite Filling (yellow)

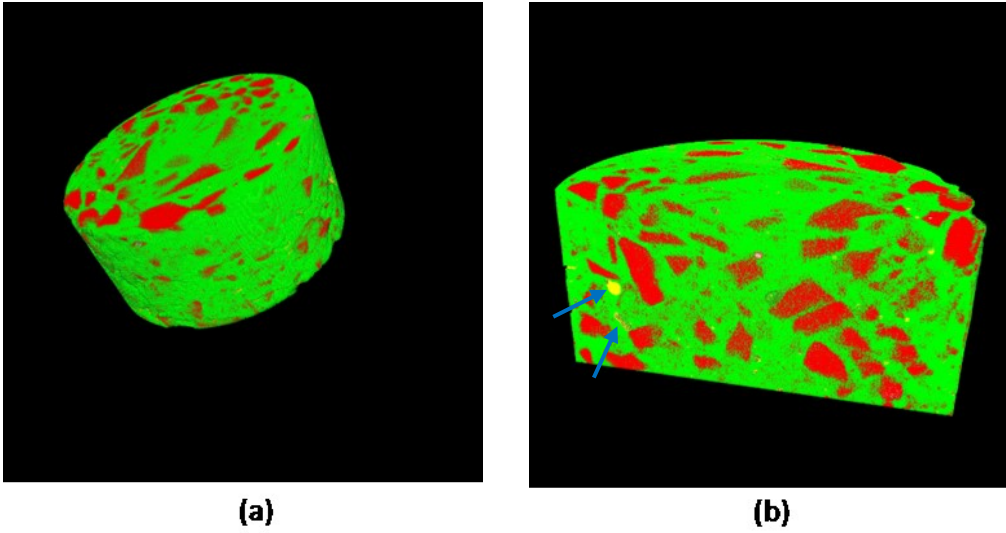


Figure 9-33: 3D Rendering and Section through a Heat-treated Specimen with High Potassium at age 230 Days. The Blue Arrow Indicates Potential Ettringite in Pores

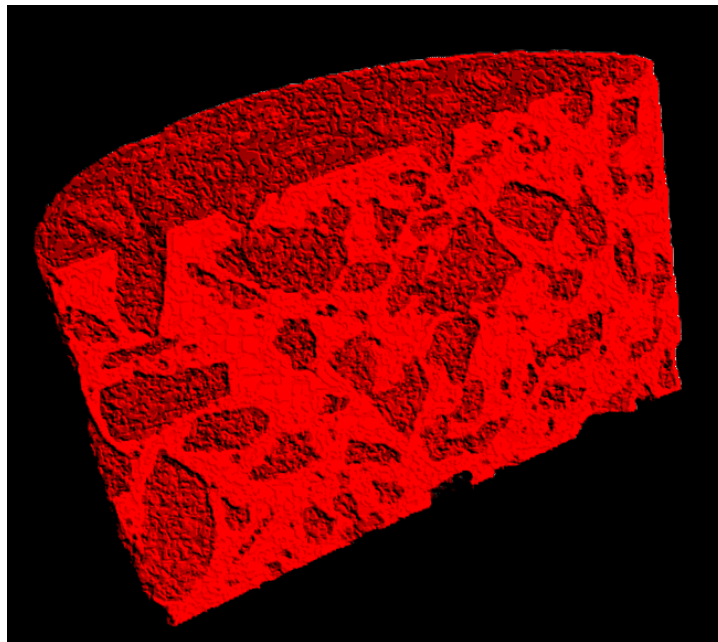


Figure 9-34: 3D Rendering of Paste Stack of Slices for a Heat-treated Specimen with High Potassium at Age 230 Days

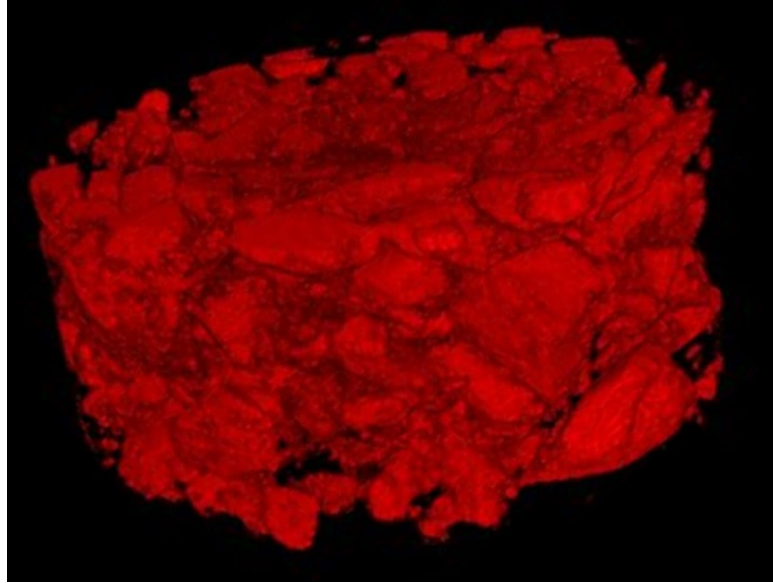


Figure 9-35: 3D rendering of stack of slices from heat-treated specimen with high potassium at age 230 days

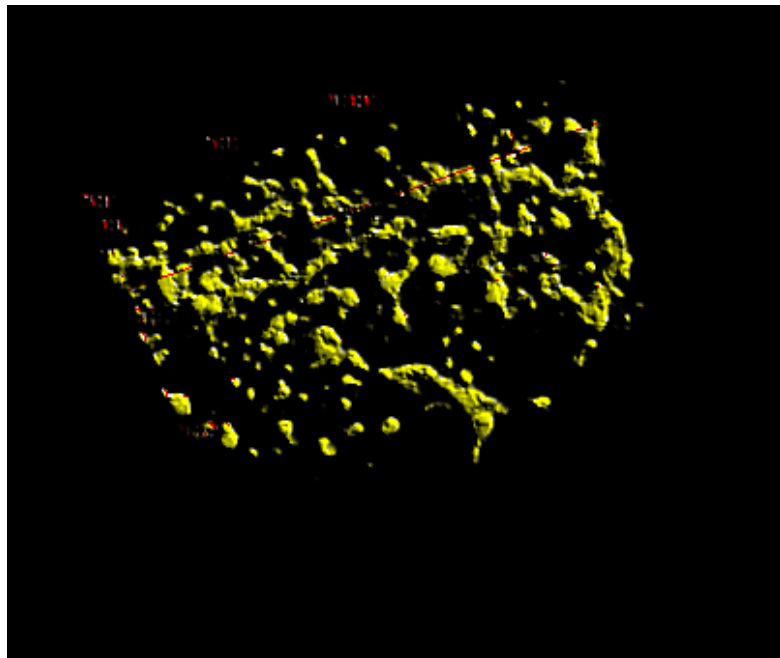


Figure 9-36: 3D Rendering of Suspected Ettringite Stack of Slices from Heat-treated Specimen with High Potassium at age 230 Days

## Chapter 10 : Discussion

### *10.1- Introduction*

Expansion, weight change and compressive strength data of concrete specimens were analyzed for potential correlation. In this chapter, we establish the correlation between the three parameters resulting from DEF in concrete; expansion, weight change and compressive strength, as well as a three-stage model of deterioration of concrete can help explain the mechanism of deterioration observed.

### *10.2- Correlations*

#### 10.2.1. Expansion and Weight Change of Specimens

Potential correlation between specimen length change and weight change, which may result in formation and growth of ettringite, was investigated. In fact, various studies (Grattan-Bellew *et al.*, 1998; Mcmorris, 2003; Shimada *et al.*, 2005; Ceesay, 2007; Ceesay, 2007) have concluded that there is a correlation between the weight change and expansion of concrete. The plot of Figure 10-1 shows that only in heat-treated specimens does expansion vary with weight change. We applied linear regression curves at early age and late age to obtain correlations between expansion and weight changes for those heat-treated specimens.

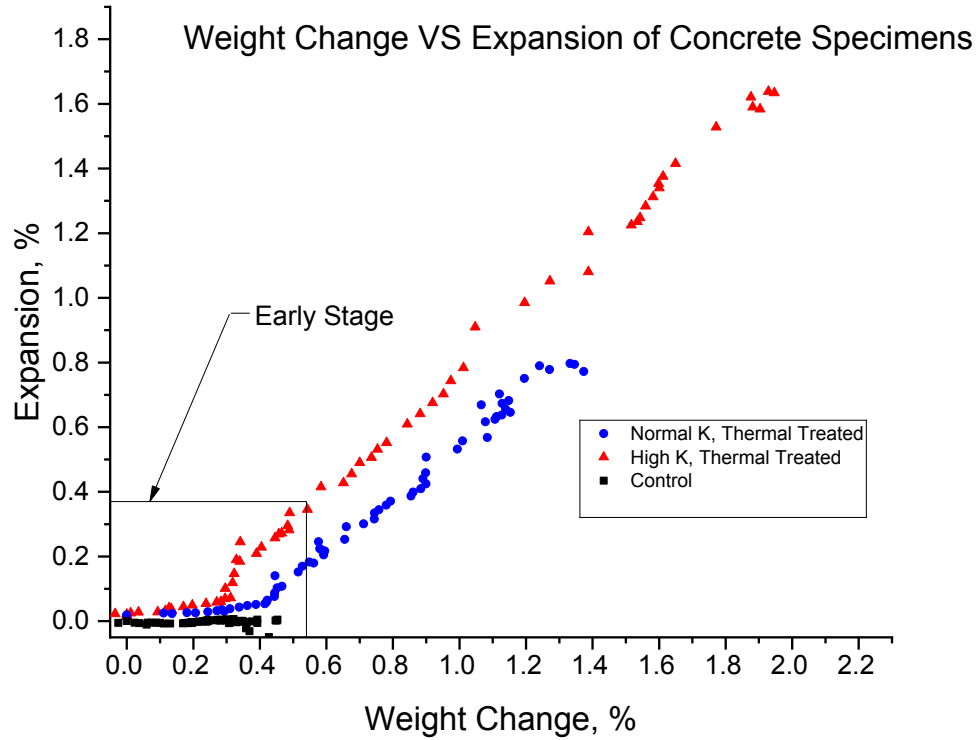


Figure 10-1: Plot of Weight Change VS Expansion of Concrete Specimens

At early age, a linear relation can be found when weight gain reached 0.16% for specimens with high potassium and 0.18% for those with normal potassium (Figure 10-2). The relatively equal values of slope for the two type of specimen (0.134 and 0.149) suggest that the occurrence of the same process in both. Prior to that there is weak correlation between the two characteristics and this can be explained by the fact that cement hydration has not been completed yet and concrete and the intake of water is used in these non-expansive reactions (Clifton e Pommersheim, 1994).

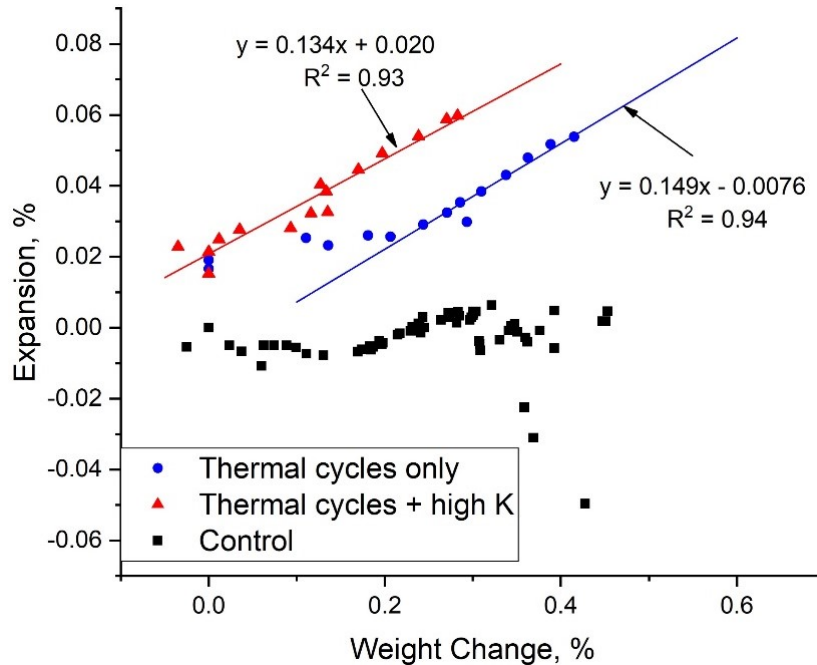


Figure 10-2: Early Age Expansion VS Weight Change of Concrete Specimens

At a later age, plot of weight change VS expansion and curve fitting (Figure 10-3) shows a strong linear relation between expansion and weight change for heat-treated specimen with normal potassium ( $R^2 = 0.997$ ) and high potassium ( $R^2 = 0.9887$ ). The significant weight increase in those specimens is due to the formation of ettringite and the resulting cracks in which water is trapped.

The curve of Expansion against weight change for specimens with normal potassium lag adjusted was also plotted (Figure 10-4). It can be seen that it coincides with the plot for specimen with high potassium, this means that at this stage, both sets expanded in the same manner and that expansion was driven by the same mechanism regardless of the amount of potassium.

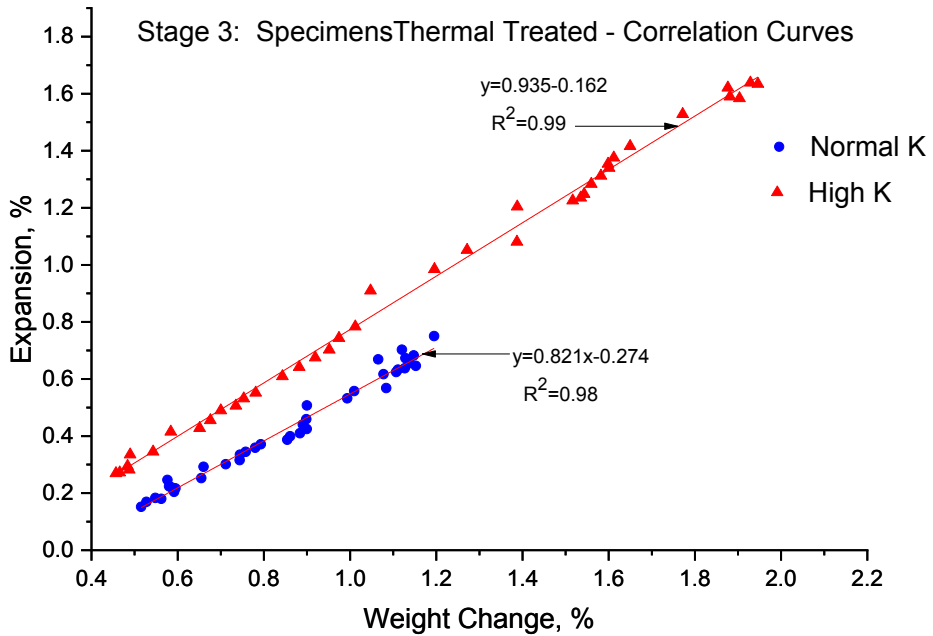


Figure 10-3: Fitting Curve of Late Age Weight change VS Expansion of Heat-treated Specimens.

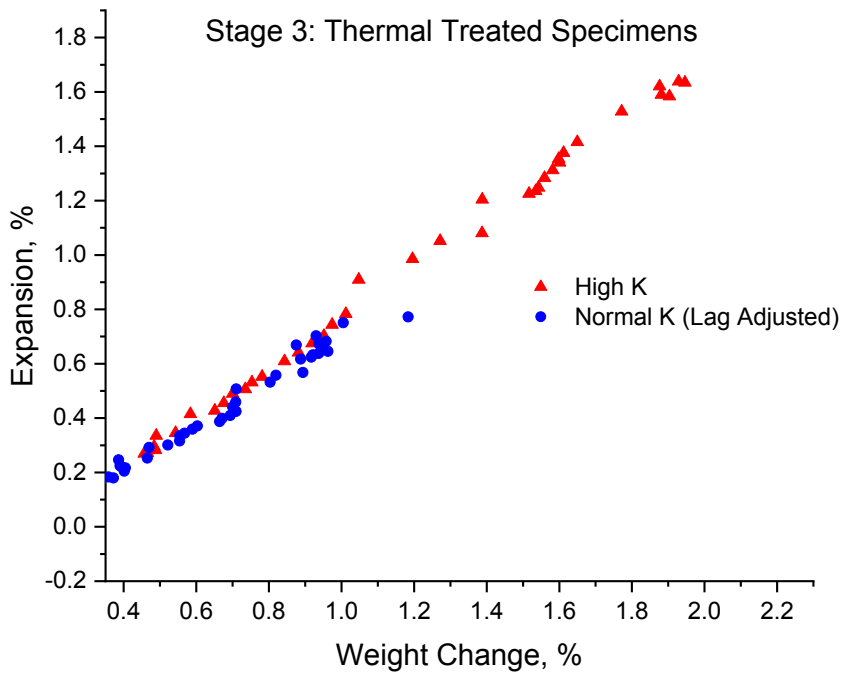


Figure 10-4: Plot of Expansion VS Weight Change of Heat-Treated Specimens with Normal Potassium Lag-Adjusted and With High Potassium Non- Adjusted

Table 10-1: Linear Equation for Expansion of Heat-Treated Concrete Specimens

Specimens	Age	Onset, Days	Slope	Equation	R <sup>2</sup>
Heat-Treated	Early	30	0.149±0.013	y=0.149x-0.0076	R <sup>2</sup> =0.94
	Late	60	0.821±0.02	y=0.821x+0.274	R <sup>2</sup> =0.98
Heat-Treated+K	Early	25	0.134±0.01	y=0.134x+0.020	R <sup>2</sup> =0.93
	Late	60	0.935±0.01	y=0.935x-0.162	R <sup>2</sup> =0.99

### 10.2.2. Expansion and Compressive Strength

Correlation between expansion and compressive strength was also analyzed and despite the limited amount of data on compressive strength (Only 5 points), it can be noted from the plot of Figure 10-5 that both specimens follow the same trend (Both curves have the same shape) and showed that expansion leads to a decrease of compressive strength.

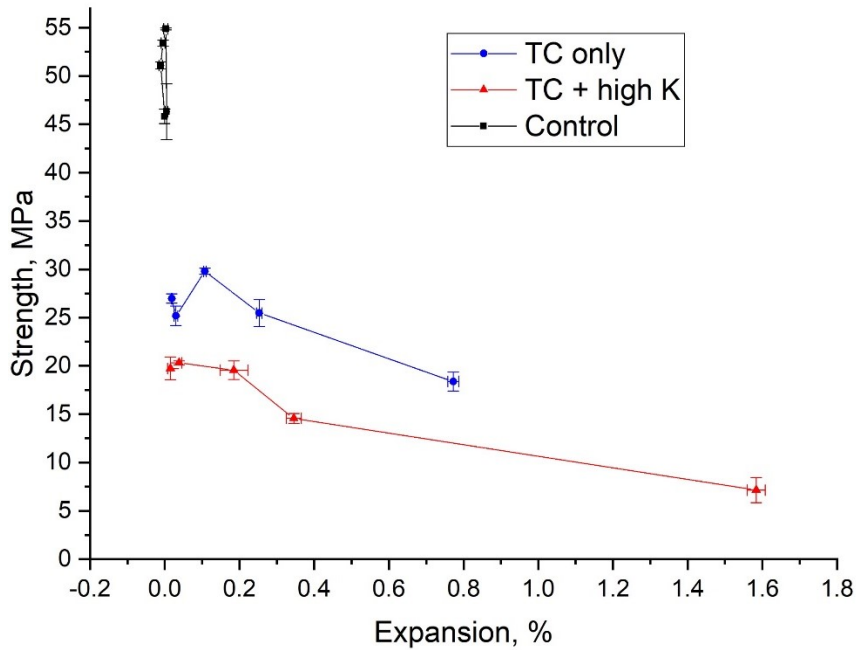


Figure 10-5: Plot of Expansion VS Compressive Strength of Heat-Treated Concrete Specimens

### 10.3- Stage Model of Expansion

Closer investigation of expansion curves (Figure 9-1), curves of weight change (Figure 9-6) and correlation curves (Figures 10-1, 10-2 and 10-3) shows that expansion and weight change in concrete occurred in three distinctive stages as shown in Figure 10-6. In the first stage, the specimens gained weight rapidly but there was little to no expansion. In stage 2, The weight gain was accompanied by a small expansion and in the last stage, weight gain lead to significant expansion of the specimens.

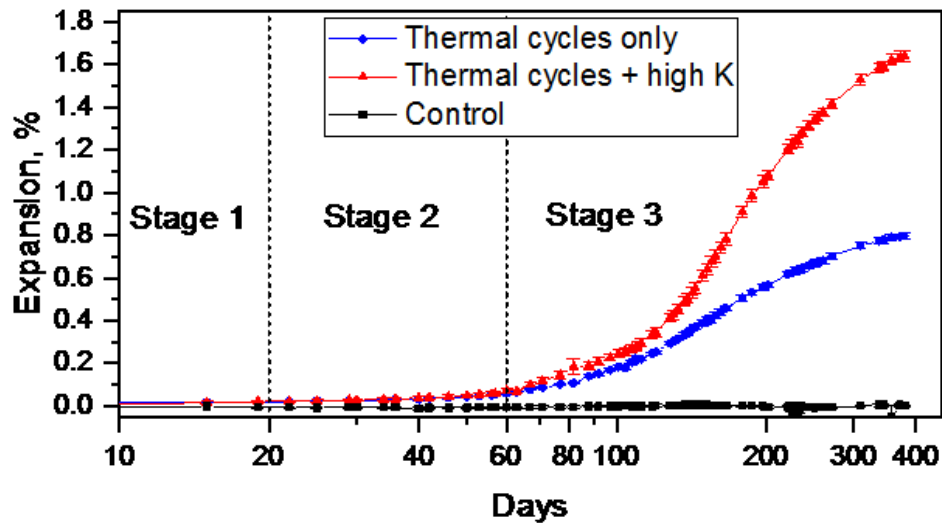


Figure 10-6: Plot of Expansion of Concrete Specimens Showing Three Stages Model

#### 10.3.1. Stage 1: 0 Days to 20 Days of Age: Weight Gain But no Expansion

During the first stage, the weight gain in specimens is not accompanied by any expansion. This corresponds to the period during which cement hydration is accelerated (Shimada *et al.*, 2005). The presence of ettringite is also confirm during this stage by SEM and EDS analysis and it can be suggested that at this stage, ettringite has not yet filled capillary pores and the pores are able to accommodate stresses due to nucleation (Clifton e Pommersheim, 1994). Another explanation is that at this stage concrete has a low strength and can easily accommodate stresses generated by ettringite growth. The morphology of ettringite can

also explain the absence of expansion, as the SEM shows ettringite as spherical crystals layering the pore walls (Figure 9-12). The compressive strength of concrete at this stage increases steadily.

#### 10.3.2. Stage 2: 20 Days to 60 Days: Weight Gain with Little Expansion

At this stage, more ettringite is growing in pores, and swelling pressure creates creep strain on the pore walls. Even though concrete strength has significantly increased, it cannot accommodate the stresses exerted by ettringite on pore walls, leading to brittle failure: microcracks are initiated and expansion is observed. The morphology of ettringite found by SEM at this stage shows clusters of thin needle-like ettringite crystals growing and replacing spherical crystals found in the previous stage (Figure 9-13). The pores are not completely filled and the expansion observed might be explained by the fact that ettringite needles growing across the capillary pores rather than uniformly filling the pore volume exert significant stresses on the pore walls leading to microcracking due to their reduced tip surface (Clifton e Pommersheim, 1994). It is also noted that at this stage, none of the specimens displayed surface cracks. Compression test results show a decrease in the compressive strength for both sets of specimens at around 80 days, which confirm the appearance of brittle micro-cracks.

#### 10.3.3. Stage 3: After 60 Days: Weight Gain Leading to Significant Expansion

At the late stage, Figure 10-1 shows that weight gain is accompanied by significant expansion of the specimens. Concrete strength has increased to the point where resistance to creep develops. At the same time further ettringite deposition takes place in cracks that grow wider and longer. More moisture becomes then available and fuels the growth of ettringite crystals that in turn leads to more cracking. It can also be observed at this stage

that there is a steady decrease in the compressive strength of the specimens, because micro-cracks and voids in the concrete become interconnected, which weakens the microstructure and lead to decrease in concrete strength (Figure 10-5). SEM of voids at the interface of aggregate and paste shows thick needle-like ettringite crystals densely filling the pores (Figure 9-19).

Table 10-2: Summary of Ettringite Morphology VS Age of Heat-Treated Specimens

<b>Stage</b>	Stage 1	Stage 2	Stage 3
<b>Age (Days)</b>	0 to 20	21 to 60	After 60
<b>Ettringite Morphology</b>	Individual sphere shape crystals	Clusters of thin needle-shape crystals	Individual thick needle-like crystals

#### *10.4- Derivation of the Slope for the Late Stage Linear Relationship*

Regression analysis of the expansion and weight gain data of heat-treated specimens has shown that there is a strong linear relation at late age (Figure10-3). A weight gain effect associated with DEF expansion was previously noted in mortar specimens immersed in water (Famy *et al.*, 2001; Aqel e Panesar, 2018). In this section, we develop a theoretical test of the possible mechanism of expansion at late stage. The model is based on the assumption that DEF among all the other types of sulfate attacks is the main cause of expansion. The test is also based on the concept of excluded volume in which the amount of expansion is assumed to be proportional to the difference between the net volume of ettringite form in voids and the original capillarity porosity. ((Clifton e Pommersheim, 1994).

The result of the linear regression analysis showed that the linear expansion is expressed as a function of the weight change by the linear relationship:

$$\varepsilon = a\omega + b \quad \text{Eq. 25}$$

Where:  $\varepsilon$  = Linear expansion =  $\Delta l/l$

( $l$  = initial length)

$\omega$  = normalized weight change =  $\Delta m/m_0$

( $m_0$  = Initial weight)

$b$  = Intercept

$a$  = Slope

The volumetric change can be estimated from both the expansion data and the weight change data. For the expansion data, the volumetric expansion of a prismatic solid can be expressed in terms of the linear expansion as follows:

$$\Delta V = lwh(1 + \varepsilon)^3 - lwh \quad \text{Eq. 26}$$

$$\Delta V = lwh[(1 + \varepsilon)^3 - 1] \approx 3\varepsilon wh \quad (\text{for } \varepsilon \text{ very small}) \quad \text{Eq. 27}$$

where:  $l$  = Length

$w$  = Width

$h$  = Height

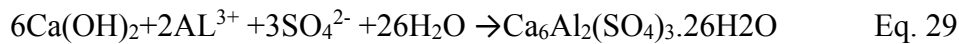
$\varepsilon$  = linear expansion

To estimate the volume change based on the weight change data, it is first necessary to assume that the observed weight increase is due solely to water from the limewater bath becoming bound into the ettringite crystals. This is justified by the fact that the amount of all the constituents of the concrete are fixed from the start by the mix design. Then the mass of ettringite formed  $m_{ett}$  is given by:

$$m_{ett} = \frac{\Delta m}{f_{H_2O}} \quad \text{Eq. 28}$$

$f_{H_2O}$  = Mass fraction of water in ettringite

However, the resulting volume increase must take into account the initial volume of the reactants (Clifton e Pommersheim, 1994). This requires the identification of the reactions involved. It is hypothesized here that this reaction involves the consumption of existing calcium hydroxide (CH) in cracks, voids and the ITZ. This calcium hydroxide is deposited here as the main product of cement hydration. This is based on SEM results which show CH crystals being transformed into ettringite. (See Section 9-4). The chemical reaction for CH attack leading to ettringite is:



This indicates that 6 moles of CH are consumed for each mole of ettringite that is formed.

The expansion factor  $\nu$  is defined as the volume of the reaction products minus the volume of reactants divided by the volume of reactants (Clifton e Pommersheim, 1994).

In this case:

$$\nu = \frac{V_{mEtt} - 6V_{mCH}}{6V_{mCH}} \quad \text{Eq. 30}$$

Where  $V_{mEtt}$  is the molar volume of ettringite and  $V_{mCH}$  is the molar volume of calcium hydroxide. The molar volume is defined as the molecular weight of a substance divided by its density.

$$\text{For ettringite, } V_{mEtt} = 1254.62/1.77 = 708.83 \text{ cm}^3/\text{mol}. \quad \text{Eq. 31}$$

$$\text{For calcium hydroxide, } V_{mCH} = 74.08/2.23 = 33.22 \text{ cm}^3/\text{mol}. \quad \text{Eq. 32}$$

$$\text{Hence } \nu = 2.56. \quad \text{Eq. 33}$$

The mass of calcium hydroxide consumed can be calculated from the mass of ettringite created as expressed in eq. 28

$$m_{CH} = f_{CH} \frac{\Delta m}{f_{H_2O}} \quad \text{Eq. 34}$$

Where  $f_{CH}$  is the mass fraction of calcium hydroxide in ettringite. The volume of CH can be found by dividing this mass by the density of calcium hydroxide.

Therefore, the change in volume calculated from the weight change data is:

$$\Delta V = \frac{f_{CH} \Delta m v}{\rho_{CH} f_{H_2O}} = \frac{f_{CH} v m_0}{\rho_{CH} f_{H_2O}} \omega \quad \text{Eq. 35}$$

Where  $\rho_{CH}$  is the density of calcium hydroxide. The right-hand side of Eq. 35 is obtained from the definition of the normalized weight change variable:  $\omega = \Delta m/m_0$

Setting the volume change estimated from the expansion data Eq. 30 equal to the volume change estimated from the weight change data Eq. 35 and rearranging, we have:

$$\varepsilon = \frac{f_{CH} v m_0}{3lwh\rho_{CH}f_{H_2O}} \omega = \frac{f_{CH} v \rho_{con}}{3\rho_{CH}f_{H_2O}} \omega \quad \text{Eq. 36}$$

Where  $\rho_{con}$  is the density of concrete

Comparing Eq. 36 with Eq. 28 reveals that the late stage slope is therefore given by the equation:

$$a = \frac{f_{CH} v \rho_{con}}{3f_{H_2O} \rho_{CH}} \quad \text{Eq. 37}$$

The density of concrete can be estimated from the mean of the weights of the prisms at the start of the experiment to be  $4.003 \pm 0.015$  kg and the volume of the prisms,  $1659.19$   $\text{cm}^3$ , to be  $2.413 \pm 0.009$   $\text{g/cm}^3$ .

The values for the other parameters in Eq. 37 are:

$$\rho_{CH} = 2.23\text{g/cm}^3$$

$$f_{CH} = 0.354$$

$$f_{H_2O} = 0.373$$

$$V = 2.56$$

Thus, the estimated theoretical slope  $a = 0.876 \pm 0.003$  Eq. 38

A similar development can be made assuming that ettringite is formed by consumption of monosulfate as expressed by Eq. 2. In which case the theoretical slope would be  $a = 0.670 \pm 0.003$ .

The theoretical value of the slope of the linear equation if ettringite is formed by consumption of calcium hydroxide ( $a = 0.876 \pm 0.003$ ) is closer to the experimental values ( $0.82 \pm 0.02$  for specimens with normal potassium and  $0.94 \pm 0.01$  for those with high potassium) compare to the slope for the reaction involving the consumption of monosulfate.

This finding suggests that the mechanism of ettringite formation is by the attack on pre-existing calcium hydroxide crystals given by Eq. 29 instead of the reaction of monosulfate as proposed by the theories described in Section 2.1.3.

## 10.5- Kinetics Modeling of Concrete Deterioration

### 10.5.1. The Avrami Nucleation and growth Model

The Avrami model describes the isothermal transformation that occurs within a fixed volume solid by a nucleation and growth process for which nucleation is spatially random and the linear growth rate  $G$  in any direction is constant. (Thomas, 2007). The model is based on the independent works of Avrami, Kolmogorov and Johnson and Mehl. The Kolmogorov-Avrami-Johnson-Mehl (KAJM) model describes changes in the volume of

the crystals as a function of time during crystallization (Avrami, 1939; Marangoni, 1998; Livingston, 2000). The fraction volume transformed  $X$  is given by the general form of the KAJM equation is expressed as:

$$X(t) = A(1 - e^{-(Kt)^n}) \quad \text{Eq. 39}$$

Where:

$X(t)$  = Fraction volume transformed at time  $t$

$A$  = Normalization constant is the limiting value for  $X(t)$  as  $t$  goes to infinity

$K$  is the overall kinetic rate constant which depend on the temperature

$t$  = Time

$n$  = The Avrami exponent (varies between 1 and 4)

#### 10.5.2. Curve Fitting

There are numerous transformations that occur in concrete where the kinetics can be expressed using the KAJM model. The most common ones are reactions of hydration and deterioration mechanism involving nucleation and growth of crystals like ice and ettringite in hardened concrete (Livingston, 2000; Thomas, 2007). The KAJM model has been used for example to characterize fractal nucleation and growth of products of tri-calcium silicate hydration in concrete (Livingston, 2000; Thomas, 2007).

The KAJM model is used in this study to characterize the kinetics of the nucleation and growth of secondary ettringite in concrete at late stage ( $t_0 = 60$  days). It provides a set of parameters to characterize the DEF induced deterioration process which are more reliable than the expansion observed at a fixed time, as presently used in the ASTM conventional method. This approach can also be used to isolate individual expansion mechanisms if they occur on

different timescales. This analysis thus resolves the contribution of DEF to the overall expansion.

The specimens' expansion data at late stage ( $t_0 = 60$  days) for the three types of specimens were fitted to a KAJM equation of the form:

$$\varepsilon(t) = A(1 - e^{-[K(t-t_0)]^n}) \quad \text{Eq. 40}$$

In which:

$\varepsilon(t)$  = Average expansion at time  $t$  in %

$A$  = Normalization constant related to the number of cracks in the specimen

$K$  is the kinetic rate constant

$t$  = Time in days

$t_0$  is the induction time, which in this case is the delay (in days) between the start of the experiment and time of start of nucleation and growth of ettringite.

$n$  = The Avrami exponent

Figure 10-7 to Figure 10-9 below are synopsis of the results and Table 10-2 provides a summary of the fitting parameters obtained.

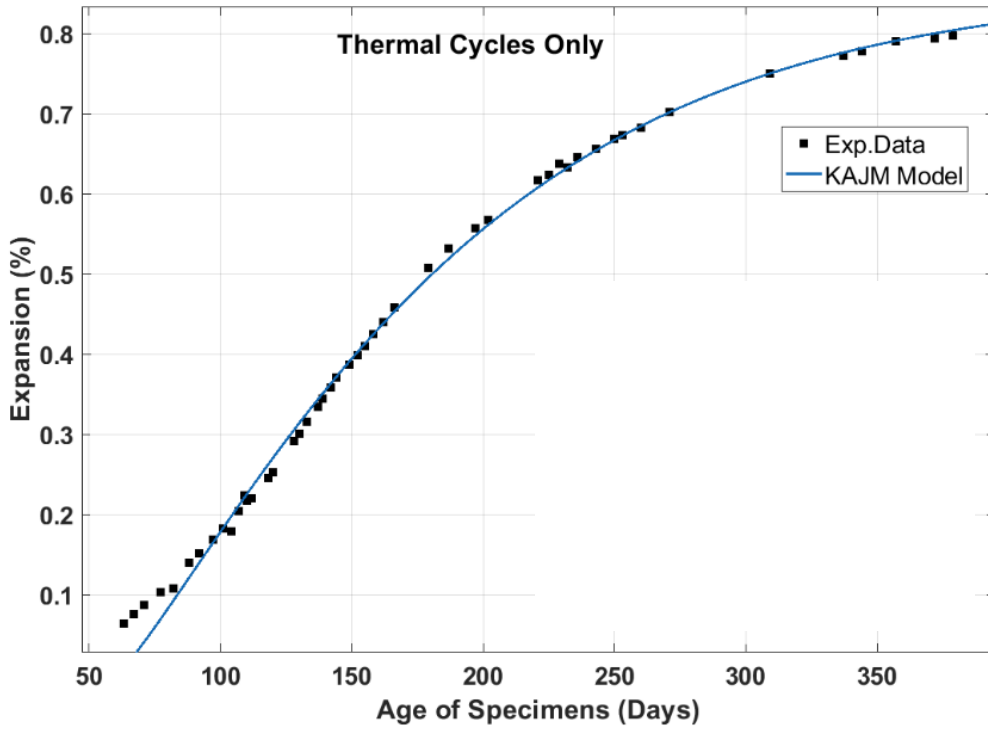


Figure 10-7: KAJM Fitting Curve of Expansion Data for Heat-Treated Specimens with Normal Potassium

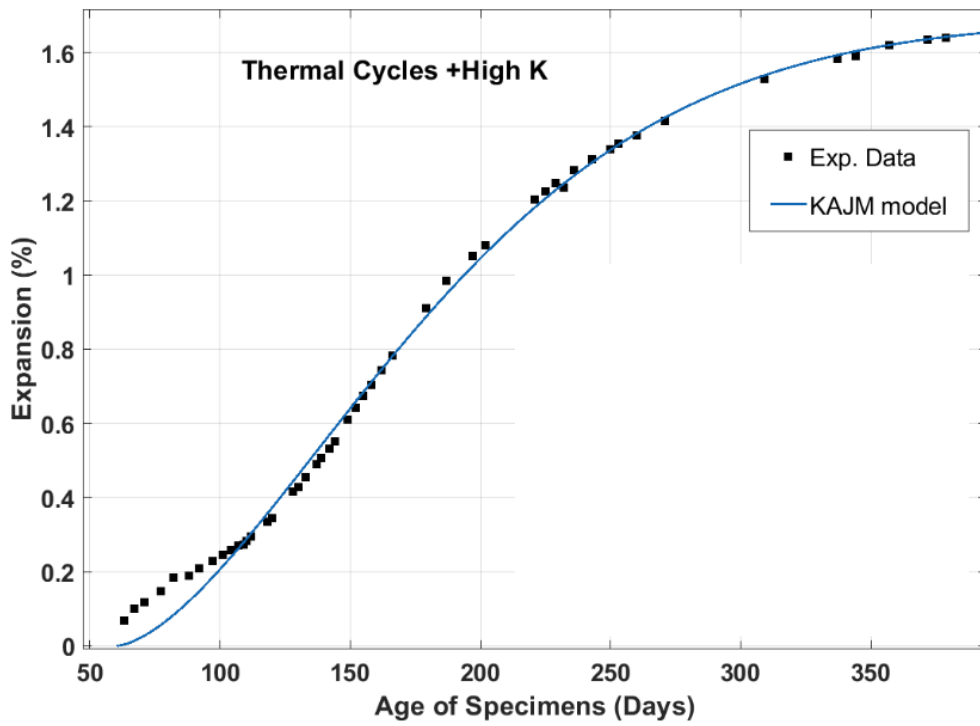


Figure 10-8: KAJM Fitting Curve of Expansion Data for Heat-Treated Specimens with High Potassium

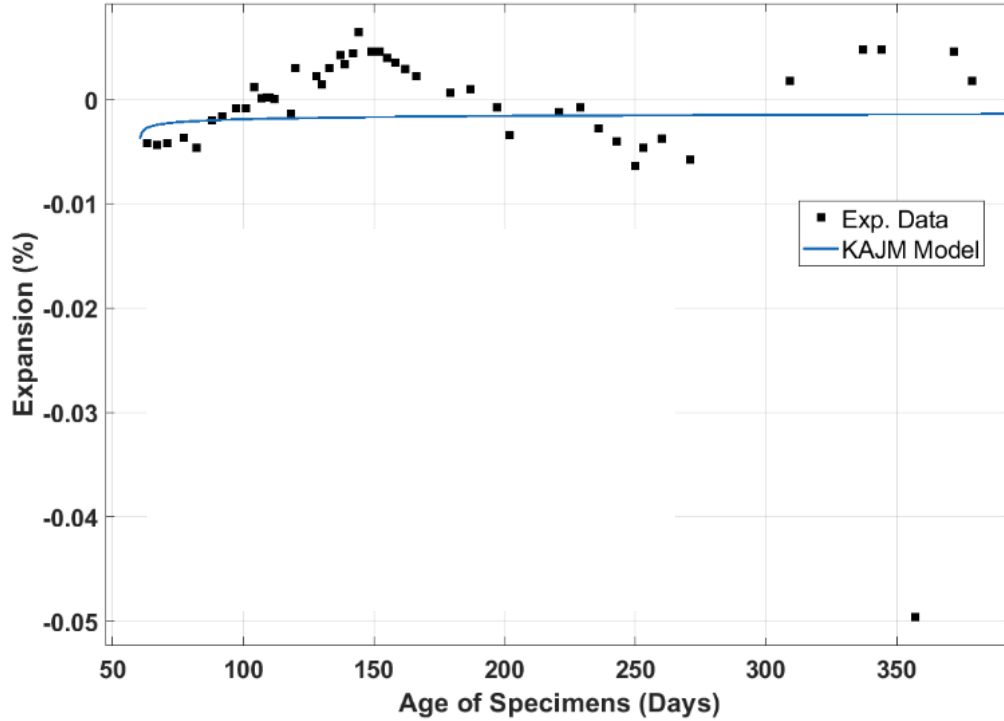


Figure 10-9: KAJM Fitting Curve of Expansion Data for Control Specimens

Table 10-3: Fit Parameters of the KAJM Model for Concrete Specimens Expansion

Specimen	$A$	$K$	$n$	$R^2$	SSE	RMSE
Norm. K, Heat	0.8552	7.5e-03	1.1980	0.9940	0.01605	0.01848
High K, Heat	1.689	7.0e-03	1.595	0.9948	0.07163	0.03904
Control	-0.00806	$\infty$	-0.0004	5.96e-05	0.004277	0.00954

$R^2$ : Coefficient of determination

SSE: Sum of Squared Errors

RMSE: Root Mean Square Error

Figures 10-7, 10-8 and 10-9 are fitting curves of expansion data for heat-treated specimens with normal potassium, with high potassium and control specimens, respectively.

From Table 10-2 and the figures of fitting curves it can be concluded that at late stage (beyond 60 days), there is a good fit between the expansion data and the KAJM model for

heat-treated specimens with normal level of potassium (Figure 10-7) and with high level of potassium (Figure 10-8), with  $R^2$  of 0.99 with 95% confidence interval for both. This suggests that the kinetics of ettringite nucleation and growth in these specimens follows an Avrami model. On the other hand, there is little to no fit of the expansion data for the control specimens as the KAJM model (Figure 10-9) has very low  $R^2$  value of  $5.96 \times 10^{-5}$ .

### 10.5.3. Physical Interpretation of Parameters

#### a) The Rate Constant ' $K$ '

The parameter  $K$  also called the rate constant incorporates the rate of nucleation and growth.  $K$  contains all the temperature dependent terms because thermal activation affects the growth strongly through boundary/interface mobility and because the nucleation density depends very strongly on the driving force. The parameter  $K$  therefore reflects the rate at which reactions are occurring in the concrete specimen. The value of  $K$  observed in specimens with added potassium is similar to that of specimens with normal level ( $7 \times 10^{-3} \approx 7.5 \times 10^{-3}$ ). This means that in both specimens, the reaction resulting in ettringite occurred at the same rate. This can be explained by the fact that the reaction is not controlled or influenced by the potassium content. Since potassium was designed to initiate cracks, it also suggests that the rate of reaction does not depend on the amount of initial cracks in the specimen or the amount of water reaching nucleation sites through those cracks. The rate is most likely controlled by other processes.

#### b) The Asymptotic Expansion Coefficient ' $A$ '

The coefficient  $A$  is a normalization constant which is the limiting value for  $\varepsilon(t)$  when  $t$  goes to infinity.  $A$  is characteristic of the amount of cracks that was initiated in concrete

specimens by the heat cycle at the beginning of the experiment. The higher value of  $A$  for specimen containing additional potassium ( $A=1.69$ ) compare to that of specimens with normal level of potassium ( $A=0.86$ ) suggest that more cracks were initiated in the former by the heat cycle. Since the only difference between the two batches is the amount of potassium, we can hypothesize that additional potassium lead to more microcracking during thermal cycling. This can be explained by the fact that potassium makes concrete more brittle and therefore more prone to cracking.

### c) The Dimensionality ‘ $n$ ’

The parameter  $n$  also called the Avrami exponent present in the model expresses the dimensionality of the transformation and phase change that takes place in the concrete specimen. For  $n = 1$ , the transformation takes place along a line; for  $n = 2$  it occurs on a surface and for  $n = 3$  throughout a volume.  $n$  depends on the nucleation mechanism, growth morphology and the density of nucleation sites (Alexander *et al.*, 2008; Torrens-Serra *et al.*, 2011). The general expression for  $n$  is given by the following equation (Starink, 2001):

$$n = N_{dim}g + B \quad \text{Eq. 41}$$

Where  $g$  is 1 for linear growth or  $\frac{1}{2}$  for parabolic growth,

$B$  is 0 in the case of site saturation (no nucleation during the transformation), or 1 for continuous nucleation (At constant nucleation rate),

$N_{dim}$  is the dimensionality of growth.

If nucleation of ettringite had occurred uniformly in three dimensions, one might expect  $n$  to be 3 or 4 if nucleation and growth occurred concurrently with growth. However, the

values obtained by fitting expansion data is  $n \approx 1.2$  and  $n \approx 1.6$  respectively for the batch thermally heated and the batch with high potassium and thermally treated, which is outside the expected range. One potential explanation is that the growth of ettringite occurs in one dimension as SEM shows that ettringite found at late stage in the specimen have a needle-like (Figure 9-19) or plate-like morphology (Figure 9-20). Another explanation is that the distribution of nucleation sites was non-random and therefore the growth may be restricted to 1 or 2 dimensions (Cahn, 1956). In this case, it can be hypothesized that nucleation occurred at specific sites like the aggregate paste interface (interfacial transition zone) as suggested by the Garboczi model.(Garboczi, 1997). The larger value of  $n$  for the high potassium specimens implies a greater density of microcracks which is consistent with findings for the  $A$  parameter.

#### *10.6- Discussion on the Simultaneous Neutron and X-ray Tomography*

The use of simultaneous neutron and X-ray tomography showed a lot of promise as it was possible to visualize spatial relations between phases, allowing for qualitative analysis. Algorithms have been developed for post-processing issues including beam hardening, registration, noise reduction, however many issues prevent reliable quantitative analysis of the data. Those issues include the resolution, limitations with computational capabilities, reconstruction methods and registration uncertainties

##### 10.6.1. The Effective Image Resolution

The image resolution has various meanings however the one that we refer to in this case is that the resolution is the measure of how close two objects can be to each other and still be visibly resolved or distinguished. The resolution in this case is also the minimum size that an object can have and still be distinguished among surrounding objects. The

resolution for our tomography was estimated to be twice the pixel size, which means  $30\mu\text{m} \times 2 = 60\mu\text{m}$ . Zheng (Zheng *et al.*, 2005) estimated the ITZ thickness to be between in the range of 9 to  $51\mu\text{m}$  for normal concrete, other authors suggest a value of around  $35\mu\text{m}$  (Diamond, 2007). Due to the low resolution, it was not possible to clearly identify and segment the ITZ and identify ettringite crystal.

For the NeXT system, the resolution is a function of the field of view or the dimension of the sample that is being scanned as shown in Table 10-4. A means to improving the resolution is then to use smaller specimens in the experiment. One of the challenges with concrete is therefore to design specimens that are small enough while still being representative sample.

Table 10-4: Detector Pixel Pitch and Field of View Specification

Pixel size ( $\mu\text{m}$ )	Field of view (mm)
6.5	$17 \times 14$
9.0	$23 \times 19$
10.5	$27 \times 23$
15.0	$38 \times 32$
17.2	$44 \times 37$
23.9	$61 \times 52$
30.0	$77 \times 65$
51.4	$131 \times 111$

(Source: LaManna et al. 2017)

### 10.6.2. Computational Resources Limitations

One of the biggest challenges that were encountered was the limitations of the computational resources available. Due to the average size of each data set (average  $\sim 32$  GB). The format adopted by NIST for its acquisition system is TIFF which has the advantage that it stores more information compare to other formats as JPEG, GIF, PNG or

else. The drawback however is that TIFF files require significant storage space. As an illustration, each file had size~16.9 MB. The data set had therefore approximately 30.5GB. Downsizing the data by converting to other format of smaller size or compressing the files would have resulted in loss of information, which can be critical for analysis at the microscopic scale. It was therefore imperative to maintain the same file format throughout the processing. Most computers have a RAM of up to 16 GB. The rule of thumb is that for most image analysis software, the size of the RAM needed to efficiently analyze data has to be 4 times the size of the data. Which meant a computer with RAM of up to 32 GBx4=128 GB. Such computer capability is not always readily available and was not available. One way to mitigate this limitation was to divide the data set in subsets that could be readily handled. While this approach was used for some operations like slice partitioning, 2D histogram generation and pixel classification, other operations like 3D or volume registration required the whole volume be loaded into the computer.

### 10.6.3. Reconstruction and Registration Issues

Registration issues stemmed from problems with the reconstruction. The neutron beam is a cone beam. However, the reconstruction was done with parallel beam method of reconstruction. For a relatively small sample, all the rays reaching the sample seem parallel, however for relatively large specimens; the beam reaches some parts of the specimen at a certain angle. Therefore, neither the parallel beam reconstruction nor the cone beam reconstruction seemed appropriate. An uncertainty is then introduced which trickles down when we try to register neutron and X-ray images.

#### 10.6.4. Issues with Phase Detection and Separation

One of the problems encountered was assignment of pixels to different concrete phases. The process was done by trial and error. The difficulty stems from the fact that each phase gray scale value is not a single value but a range of values or an area on the 2D histogram. The polygon marking boundaries of the said area was manually drawn through trial and error (Figure 10-10). Besides the error induced by the method of determination of polygons, other factors affected the accuracy of phase segmentation including:

- Uncertainty of registration. Registration allows matching each pixel in the neutron image to its corresponding pixel in the X-ray image in order to assign the proper location on the 2D histogram. Misregistration assigns a neutron pixel to a non-corresponding X-ray pixel and therefore a wrong location on the 2D histogram. The accuracy of the phase segmentation is highly dependent on accuracy and the uncertainty of the registration.
- The noise in the image which caused the 2D histogram to be smeared.
- The beam hardening. The segmentation method used was aimed to minimize the effects of beam hardening but it was not possible to completely eliminate it. As can be seen in the 2D histogram of Figure 10-10 the negative values of attenuation coefficient for neutron and X-ray are caused both by beam hardening and the noise in the reconstructed image.

One way of improving accuracy of the segmentation would be to scan samples of each of the phases at the same time with the specimens with the same parameters.

This will then enable calibration of the 2D histogram and more accurately delineate the different phase areas.

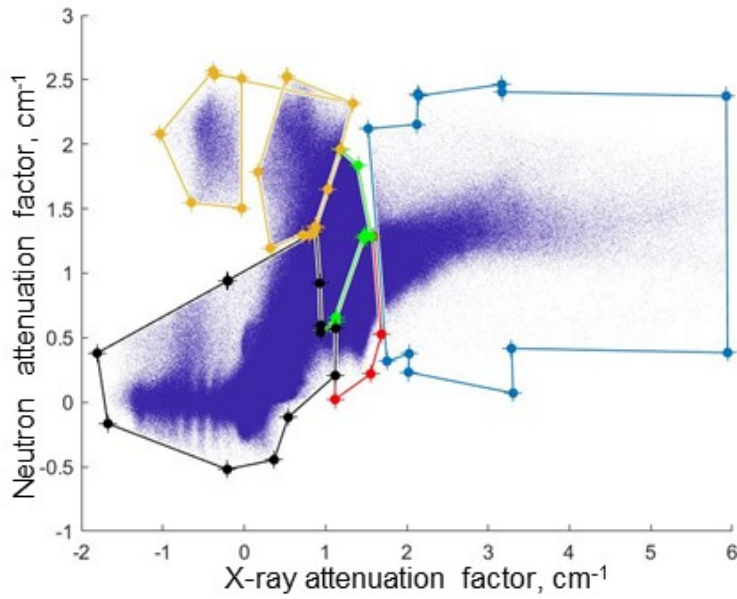


Figure 10-10: 2D Histogram of Pixel Intensities for X-ray and Neutron Volumes with Polygons Drawn for Segmentation

## Chapter 11 : Conclusions and Future Research

### *11.1- Introduction and Summary*

Previous researches have shown that late ettringite formation is an expansive phase that causes microcracking in concrete in order to accommodate the expansive growth of ettringite. The current research project was conducted in order to characterize DEF induced damage in concrete using conventional macroscopic and microscopic techniques and explore the suitability of a novel microscopic method which combines neutron and X-ray tomography to characterize these damages. The main objectives of the study were: (1) to prepare concrete specimens with methods demonstrated to develop DEF and use conventional testing methods such as length and weight change measurement, compressive strength testing and SEM-EDAX to monitor DEF induced deterioration ; (2) to analyze data obtained from those test and determine correlations; (3) to study the kinetics of concrete deterioration associated with DEF ; (4) to demonstrate the suitability of simultaneous neutron and X-ray tomography for the study of DEF in concrete; (5) to perform simultaneous neutron and X-ray tomography of concrete specimens at various age and used advanced computer programs to process data and reconstruct 3D images.

Specimens used for the study were made with concrete using type III Portland cement. In addition, some had additional potassium added to their mix such that their total potassium content was 1.72% and were heat-treated using the Duggan Heat cycle while others, which did not have additional potassium in their mix, were either also heat-treated or left untreated (Control specimens). The use of type III cement, which is a type of cement with high sulfate content, the addition of potassium to the concrete mix and the heat treatment, had the objective of initiating microcracks, promoting the formation of ettringite and accelerating

the expansion of specimens. Throughout the experiment, the specimens were kept in saturated limewater so that water was always available for reaction in pores.

The study was conducted in three phases. In the first phase, the specimens for all the various tests were made and prepared for testing. The second phase consisted of performing conventional testing (Length and weight measurement, compressive strength testing, SEM-EDAX) at defined frequencies to monitor the progress of damages in the specimens at a macroscopic scale. The third phase which ran concurrently to the second phase was dedicated to scanning specimens with the simultaneous neutron and X-ray tomography system (NeXT) at NIST at predetermined intervals.

Once testing was completed, the data were analyzed: conventional tests data were analyzed using statistical methods including correlation analysis and curve fitting. Neutron and X-ray data were preprocessed, and then tomography slices were reconstructed and processed. Reconstructed tomography images were series of slices representing each a section of the specimens. Images from each modality taken at different age were geometrically misaligned one to the other. Likewise, neutron and X-ray images taken at the same age were also misaligned. In order to be analyzed they needed to be registered. MATLAB routines based on the principle of identification of mutual information were developed for monomodal time series registration and multimodal registration. Neutron images as well as X-ray images displayed significant signs of beam hardening with the outer rim of the specimens appearing brighter than the interior. The beam hardening created artifacts such as cupping and streaks that would make it hard to accurately perform image segmentation. Since most common methods to correct for beam hardening are not effective for multiphase material like concrete, an approach was developed which allowed for segmentation without

the need to correct for beam hardening. The method relies on the assumption that beam hardening is a radial function and takes advantage of the fact that circular specimens were used for tomography. Based on this assumption, slices could be divided into rings of successive concentric rings within which the penetrating radiation energy is considered constant. Within each ring, the shift in the pixel intensity due to hardening of the beam was determined and helped adjust the pixel intensity for each phase. Segmentation or pixel assignment was then performed on each ring.

For segmentation, a thresholding method based on histogram peaks to assign pixels to each phase was used. The Neutron and corresponding X-ray images were combined, and the 2-D histograms obtained were used for classification of pixels into the different concrete phases.

## 11.2- *Conclusion of the Study*

### 11.2.1. Conventional Testing Methods

Conventional methods of analysis yield many conclusions:

- Significant DEF developed only in the heat-treated specimens, which suggests that pre-existing microcracks are a necessary condition.
- The mechanism of deterioration of concrete due to DEF occurs in three distinctive stages: in the first stage which correspond to the period of maximum cement hydration, concrete gains weight with little to no expansion. The second stage is characterized by weight gain accompanied by little expansion and corresponds to the period when microcracks are initiated in concrete. In the third phase, weight gain leads to significant expansion due to the growth of ettringite in microcracks

and widening of those microcracks. This stage is also characterized by a steady decrease of compressive strength of concrete.

- The morphology of ettringite found in concrete is different at each of these stages. Ettringite in stage 1 has the morphology of microsphere crystal layering the walls of voids. In stage 2 ettringite is present as cluster or balls of ettringite thin needles, while in stage 3 it is present as thick needle –like crystals.
- There is a strong linear correlation between the weigh change and expansion of heat-treated specimens at the second and third stages. In the last stage, the specimens expanded at greater rate relative to weight change than in the second stage.
- A theoretical derivation of the slope of the relationship of expansion versus weight change in the third stage found that the probable DEF mechanism was the replacement of the pre-existing calcium hydroxide crystals by ettringite
- Non-linear curve fitting of the expansion data of the heat-treated concrete specimens to a KAJM model of phase transformation kinetics yielded several insights:
  - The presence of potassium caused more initial cracks from heat treatment, which suggests that potassium makes concrete more brittle and prone to microcracking from heat.
  - The rate of reaction was not dependent on the amount of microcracking initially present in the specimens.
  - The low values obtained for the dimensionality parameter ‘n’ suggest that ettringite growth does not take place through the entire volume, but only at

specific sites such as cracks, pores and interfacial transition zone between the cement paste and the aggregates.

#### 11.2.2. Simultaneous Neutron and X-ray Tomography

Simultaneous neutron and X-ray tomography is a newly emerging technology for quantitative 3-D analysis of materials nondestructively at the microscopic scale. In this study, we evaluated its use to characterize DEF induced damages in concrete over time. From the feasibility study on the use of simultaneous neutron and X-ray tomography to characterize DEF damage induced in concrete, the following conclusions were reached:

- Through simultaneous neutron and X-ray tomography, it was possible to observe ettringite development in pores of concrete specimens at different ages and it showed that ettringite was visible in pores of heat-treated specimen starting at age 83 days, while they appear later on control specimens.
- Through observation of X-ray images, large cracks were visible in heat-treated specimens at all ages with many of them located around aggregates.
- Segmentation of fused images made of neutron and corresponding X-ray volume allows for reasonably good identification of the main concrete phases such as the aggregates, the paste and pores.
- Due to the low effective resolution of the imaging system on the order of  $\sim 80 \mu\text{m}$ , it was not possible to identify ettringite at the interface of paste and aggregate as its thickness has been estimated to be between 9 and  $50 \mu\text{m}$  for normal concrete.
- Processing data for simultaneous neutron and X-ray tomography presents multiple challenges that need to be resolved: The challenges included the size of the data file  $\sim 32 \text{ GB}$  which requires large computational capability computers, correction

for beam hardening for multiphase material like concrete where common correction methods are not effective, and 3-D or volume registration.

- Algorithms have been implemented for image registration, beam hardening correction and segmentation; however, they need to be fine-tuned and improved for more accuracy.
- With ongoing improvements on the NeXT system that will lead to significant improvement to the resolution of the imaging system, it will be possible to visualize the mechanism of ettringite growth and the associated deterioration.
- With improved resolution and phase segmentation, the methodological approach developed in this study would allow characterization and differentiation of damage induced in concrete by expansive phases such as ASR and DEF.

### *11.3- Recommendation for Future Research*

#### 11.3.1. Future Research with Simultaneous Neutron and X-ray Tomography

Even though in the current experiment with simultaneous neutron and X-ray tomography we were not able to do quantitative analysis due to the various issues mentioned above, this study helped understand the potential of the method to study concrete deterioration mechanisms in general and specifically the damage induced by expansive hydrous phases. Significant improvements have been made on the NeXT system at NIST since the inception of this project in term of image resolution, data processing and image reconstruction, which will allow for imaging with resolution of up to 15 microns and more streamlined data processing. The methodology that was developed and presented in this project can be used for many purposes:

- Non-destructive investigation of DEF, ASR and FT induced damage in concrete over time (4D tomography). This includes characterization and quantification of damage by microscopic analysis of crack distribution and phase distribution.
- Analysis of deformations of concrete specimens over time from displacement of individual voxels from one scan to another by Digital Image Correlation analysis.
- Finite element stress analysis using tomography data to construct a volumetric model of specimens in original undamaged condition.

#### 11.3.2. Other Future Research

- Investigate if there is a threshold level of potassium to initiate DEF in concrete.
- Investigate if there is a threshold curing temperature for initiation of DEF in concrete.
- Investigation of the effect of sodium ion compared to potassium in the initiation of DEF in concrete.

## References

- Alarcon-Ruiz, L. et al. **The Use of Thermal Analysis in Assessing the Effect of temperature on a Cement Paste**. Cement and Concrete Research, v. 36, p. 5, 2005.
- Alexander, K. et al. **Determination of Avrami Parameter in the Case of Non-Isothermal Surface Crystallization of Powdered Glasses**. 16th Conference of glass and Ceramics. Varna, Bulgaria 26-30 Sept. 2008.
- Allen, A. J.; Thomas, J. J.; Jennings, H. M. **Composition and Density of Nanoscale Calcium–Silicate–Hydrate in Cement**. Nature Materials, v. 6, p. 6, 2007.
- Amde, A. M. **UMD/FHWA Studies on Delayed Ettringite Formation**. International Conference on Advances in Concrete and Construction (ICACC2004). Hyderabad, India December 2004.
- Amde, A. M.; Ceary, M.; Livingston, R., A.,. **Investigation of Maryland Bridges for DEF and ASR**. In: Lakshmana, N.;Gopalakrishnan, S., *et al*, International Conference on Advances In Concrete Composites and Structures, ICACS-2005, p.pp. 809-816, January 6-8, 2005.
- Amde, A. M.; Livingston, R., A.,; Azzam, A. **Characterization of Damage and Development of Accelerated Test Method for Delayed Ettringite Formation**. International Symposium on Innovative World of Concrete. Pune, India September 2003.
- Amde, A. M.; Williams, K.; Livingston, R., A.,. **Influence of Fine Aggregate Lithology on Delayed Ettringite Formation in High Early Strength Concrete**. In: BJEGOVIC, D.;BEUSHAUSEN, H., *et al*, RILEM International Workshop on Performance-Based Specification and Control of Concrete Durability, Zagreb. 11-13 June 2014.
- Aqel, M. A.; Panesar, D. K. **Delayed Ettringite Formation in Concrete Containing Limestone Filler**. Materials Journal, v. 115, n. 4, p. 565-575, 2018.
- August, D. **Prof. Rontgen's X rays and their Applications in the New Photography**. Glasgow, Scotland: Bauermeister, F, 32, 1896.
- Avrami, M. **Kinetics of Phase Change. I General Theory**. The Journal Of Chemical Physics, v. 7, p. 1103-1112, 1939.
- Baghdadi, N.; Seignol, J.-F.; Toutlemonde, F. **Chemo-Mechanical Model Describing the Expansion Due to Internal Sulphate Attack: Numerical Simulation**. International RILEM Symposium CONMOD'08', Delft, Netherland , 2008.
- Barbarulo, R.; Peycelon, H.; Prene, S. **The Role of C-S-H and Temperature in Delayed Ettringite Formation**. International RILEM TC 186-ISA Workshop on Internal Sulfate Attack and Delayed Ettringite Formation. Villars, Switzeland , 2002.

Bentz, D. P. et al. **Four-Dimensional X-ray Microtomography Study of Water Movement during Internal Curing**. In: Jensen, O. M.;Lura, P., *et al*, International RILEM Conference : Volume Changes of Hardening Concrete: Testing and Mitigation, Bagneux, France. RILEM Publications S.A.R.L, 2006.

Bentz, D. P. et al. **X-Ray Microtomography of an ASTM C109 Mortar Exposed to Sulfate Attack**. Microstructure of Cement-Based Systems Bonding and Interfaces in Cementitious Materials, Symposia. Boston, MA.: Materials Research Society 1994.

Bentz, D. P. et al. **Microstructure and Transport Properties of Porous Building Materials. II: Three-Dimensional X-Ray Tomographic Studies**. Materials and Structures, v. 33, p. 7, 2000.

Brabant, L. Et Al. **A Novel Beam Hardening Correction Method Requiring No Prior Knowledge, Incorporated Into an iterative reconstruction Algorithm**. NDT&E International, v. 51, p. 68-73, 2012.

Bruneteaud, X. **Etude de l Influence de Differentes Parametres et de leur Interaction sur la Cinetique et l Amplitude de la RSI**. PhD Dissertation. Ecole Centrale de Paris, 2005

Cahn, J. W. **Transformation Kinetics During Continuous Cooling**. Acta Metallurgica, v. 4, n. 6, p. 4, 1956.

Castro, N.; Sorensen, B. E.; Broekmans, M. A. T. M. **Assessment of Individual ASR-Aggregate Particles by XRD**. In: Broekmans, M. A. T. M. (Ed.). Proceedings of the 10th International Congress for Applied Mineralogy (ICAM). Berlin: Springer, Berlin, Heidelberg, 2012.

Cearly, M. **Pilot NDT Field Survey of Maryland Bridges for Delayed Ettringite Formation Damage**. Master Thesis. Department of Civil and Environmental Engineering , University of Maryland, College Park, MD, 2003.

Cearly, M. S. **Characterization of Delayed Ettringite Formation in Maryland bridges**.. PhD. Dissertation. Department of Civil and Environmental Engineering, University of Maryland, College Park, College Park, Md, 2007

Ceesay, J. **Characterization of Damage in Mortar and Concrete Specimen Due to Delayed Ettringite Formation (DEF)**. PhD. Dissertation. Department of Civil and Environmental Engineering, University of Maryland, College Park, Maryland, 2007.

Ceesay, J. et al. **Investigation of Modifications to the Duggan Test for Delayed Ettringite Formation**. The First International Conference on Recent Advances in Concrete Technology. Washington 2007.

Chadwick, J. **Possible existence of a Neutron**. Nature, v. 129, n. 312, p. 1, 1932a.

Chadwick, J. **The Existence of a Neutron**. Proceedings of the Royal Society A, v. 136, n. 830, p. 17, 1932b.

Chen, X. J. et al. **Characterization of Progressive Microcracking in Portland Cement Mortar Using Non Linear Ultrasonics**. NDT&E International, n. 41, p. 7, 2008.

Christensen, A. N.; Jensen, T. R.; Hanson, J. C. **Formation of Ettringite and Monosulfate in Hydrothermal Hydration of Portland Cement and of Calcium Aluminum Oxide-Calcium Sulphate Dihydrate Mixtures Studied by In Situ Synchrotron X-ray Powder Diffraction**. Journal of Solid State Chemistry, v. 177, p. 1944-1951, 2004.

Clifton, J. R.; Pommersheim, J. M. **Sulfate Attack of Cementitious Materials: Volumetric Relations and Expansions**. NISTIR 5390, Gaithersburg, MD., 1994.

Colleparidi, M. **Damage by Delayed Ettringite Formation - A Holistic Approach and New Hypothesis**. Concrete International, v. 21, n. 1, p. 6, 1999.

Colleparidi, M. et al. **Tricalcium Aluminate Hydration in Presence of Lime, Gypsum or Sodium Sulfate**. Cement and Concrete Research, v. 8, n. 5, p. 571-580, 1987.

Collier, N. C. **Transition and Decomposition Temperatures of Cement Phases - A Collection of Thermal Analysis Data**. Ceramic-Silikaty, v. 60, n. 4, p. 6, 2016.

Comi, C.; Fedele, R.; Perego, U. **A Chemo-Thermo-Damage Model for the Analysis of Concrete Dams Affected by Alkali-Silica Reaction**. Mechanics of materials, v. 41, n. 3, p. 21, 2009.

Cruz, R. A. H. et al. **Ultrasonic Pulse Velocity for monitoring The Susceptibility of Concrete to Sodium Sulphate and Wetting-Drying Cycles**. Review of Latin America Metallic Material, v. 36, n. 2, p. 13, 2016.

Dauti, D. et al. **First results on fast neutron tomography of heated concrete**. 5th International Workshop on Concrete Spalling due to Fire Exposure. Exposure, T. I. W. O. C. S. D. T. F. Borås, Sweden 2017.

Day, R. L. **The effect of Secondary Ettringite Formation on Durability of Concrete: A literature Analysis**. Research and Development Bulletin. Skokie, Illinois, U.S.A: Portland Cement Association. 108T 1992.

De Beer, F. C. **Neutron and X-ray Tomography : Non-destructive Analytical Tools for the Characterization of Nuclear Material**. The Journal of the Southern African Institute of mining and metallurgy, v. 115, p. 10, 2015.

De Beer, F. C.; Middleton, M. F.; Hilson, J. **Neutron Radiography of Porous Rocks and Iron Core**. Applied Radiation and Isotopes, v. 61, p. 9, 2004.

Deschenes, D. J. **ASR/DEF-Damaged Bent Caps: Shear Tests and Field Implications**. Master Thesis. Department of Civil engineering, University of Texas at Austin, Austin, Texas, USA, 2009.

Diamond, S. **Physical and Chemical Characteristics of Cement Composites**. Durability of Concrete and Cement Composites, p. 35, 2007.

Divet, L.; Randriambolona, R. **Delayed Ettringite Formation: The Effect of Temperature and Basicity on the Interaction of Sulphate and C-S-H Phase**. Cement and Concrete Research, v. 28, p. 7, 1998.

Duggan, R.; Scott, F. **New test for Deleterious Expansion in Concrete**. In: Science, E. A., Alkali-Aggregate Reaction. 8th International Conference, New York, USA. p.403-408, 1989

Escadeillas, G. et al. **Some Factors Affecting Delayed Ettringite Formation in Heat-cured Mortars**. Cement and Concrete Research, v. 37, n. 10, p. 8, 2007.

Ezzeldeen, R. M. et al. **Automated Image Registration Approaches Using PCNN and Invariant Moments**. International Journal of Intelligent Computing and Information Sciences, v. 8, n. 1, p. 12, 2008.

Famy, C. et al. **Influence of the Storage Conditions in the Dimensional Changes of Heat-Cured Mortars**. Cement and Concrete Research, v. 31, p. 9, 2001.

Famy, C.; Scrivener, L. K.; Brough, R. A. **Role of Microstructural Characterization in Understanding the Mechanism of Expansion Due to Delayed Ettringite Formation**. International RILEM TC 186-ISA Workshop on Internal Sulfate Attack and Delayed Ettringite Formation, Villars, Switzerland, 2002

Fitzpatrick, J. M.; Hill, D. L. G.; Maurer, J., C.R. **Image Registration**. Handbook of Medical Imaging, v. 2, p. 67, 2000.

Flatt, R. J.; Scherer, G. W. **Thermodynamics of crystallization stresses in DEF**. Cement and Concrete Research., v. 38, p. 325-336, 2008.

Fu, Y. **Delayed Ettringite Formation in Portland Cement Products**. PhD. Dissertation. Department of Civil Engineering, University of Ottawa, Ottawa, 1996.

Fu, Y.; Beaudoin, J. J. **Expansion of Portland Cement Mortar Due to Internal Sulfate Attack**. Cement and Concrete Research, v. 27, n. 9, p. 8, 1996a.

Fu, Y.; Beaudoin, J. J. **Mechanism of Delayed Ettringite Formation in Portland Cement Systems**. ACI Materials Journal, v. 93, n. 4, p. 7, 1996b.

Fu, Y.; Beaudoin, J. J. **Microcracking as Precursor to Delayed Ettringite Formation in Cement Systems**. Cement and Concrete Research, v. 26, n. 10, p. 6, 1996c.

Garboczi, E. J. **Stress, Displacement, and Expansive Cracking Around a Single Spherical Aggregate Under Different Expansive Conditions**. Cement and Concrete Research, v. 27, n. 4, p. 6, 1997.

Genoves, V. et al. **Ultrasonic and Impact Spectroscopy Monitoring on Internal Sulphate Attack of Cement-Base materials**. Material and Design, v. 125, p. 9, 2017.

Ghorab, H. Y. et al. **On the Stability of Calcium Aluminates Sulphate Hydrates**. In Pure Systems in Cements. 7th International Congress on Chemistry of Cements, Paris, France. p.496-503, 1980.

Gillot, J. E.; Grabowski, E. **Mechanism of Expansion in Rapid Test Method for Alkali-Aggregate Reaction**. Department of Civil Engineering, University of Calgary. Calgary, Canada. 1990

GOSWAMI, G.; Panigraphy, P. K.; Panda, J. D. **Rapid Strength Prediction of Portland Slag Cement by X-ray Diffractometry**. 16th International Conference on cement Microscopy. Richmond, Virginia, USA: pp.257-268 p. 1994.

Grattan-Bellew, P. E.; Beaudoin, J. J.; Vallee, V.-G. **Delayed Ettringite Formation: Effect of Clinker Particle Size and Composition on Expansion of Mortar Bars**. In: Cohen, M.; Mindess, S., *et al* (Ed.). Materials Science of Concrete: The Sidney Diamond Symposium. Westerville, OH: The American Ceramic Society, p.295-307, 1998.

Gress, D. **Early Distress of Concrete Pavements**. Federal Highway Administration. 1997

Grimal, E. et al. **Creep, Shrinkage, and Anisotropic Damage in Alkali-Aggregate Reaction Swelling Mechanism-Part I: A Constitutive Model**. ACI Material Journal, v. 105, p. 9, 2008.

Hachouf, N. et al. **Characterization And MCNP Simulation of Neutron Energy Spectrum Shift after Transmission through Strong Absorbing Materials And Its Impact on Tomography Reconstructed Image**. Applied Radiation And Isotopes, v. 70, p. 7, 2012.

Hachouf, N. et al. **New Analytical Approach for Neutron Beam-Hardening Correction**. Applied Radiation and isotopes, v. 107, p. 6, 2016.

Heinz, D.; Ludwig, U. **Mechanisms of Subsequent Ettringite Formation in Mortar and Concretes After Heat Treatment.** 8th International Congress on Chemistry of Cement, Rio de Janeiro, Brazil. Secretaria General de 8th CIQC. p.pp. 189-194, 1986.

Heinz, D.; Ludwig, U. **Mechanism of Secondary Ettringite Formation in Mortars and Concretes Subjected to Heat Treatment.** Katherine and Bryant Mather International Conference, Atlanta, Georgia, USA. American Concrete Institute, 1987.

Heinz, D.; Ludwig, U.; Rudinger, I. **Delayed Ettringite Formation in Heat-treated Mortars and Concretes.** Concrete Precasting Plant and Technology, v. 11, p. 6, 1989.

Helal, J.; Sofi, M.; Mendis, P. **Non-Destructive Testing Of Concrete : A Review Of Methods.** Electronic Journal Of Structural Engineering, v. 14, n. 1, p. 9, 2015.

Hime, W. G. et al. **Chemical and Petrographic Analyses and ASTM Test Procedures for the Study of Delayed Ettringite Formation.** Cement , Concrete and Aggregates, v. 22, n. 2, p. 9, 2000.

Hime, W. G. **Clinker Sulfate: A Cause for Distress and a Need for Specification.** Concrete for Environment Enhancement and Protection. London, UK: Spon, E. Spon, F.N.: 9 p. 1996.

Hounsfield, G. N. **Computerized Transverse Axial Scanning (Tomography): Part I. Description of System.** British journal of Radiology, v. 46, p. 7, 1973.

Hussey, D. S. Et Al. **Improving Quantitative Neutron Radiography Through Image Restoration.** Nuclear Instruments And Methods In Physics Research, v. 729, p. 6, 2013.

Banhart, J. et al. **X-ray and Neutron Imaging – Complementary Techniques for Materials Science and Engineering.** International Journal of Material Research., v. 101, n. 9, pp. 1069-1079, 2010.

Jovanovic, Z. et al. **Simultaneous Segmentation and Beam Hardening Correction in Computed Microtomography of Rock Core.** Computers and Geosciences, v. 56, pp. 142-150, 2013.

Jumate, E.; Manea, D. L. **Application of X-ray Diffraction (XRD) and Scanning Electron Microscopy (SEM) Methods to Portland Cement Hydration Processes.** Journal of Applied Engineering Sciences, v. 2(15), n. 15, p. 8, 2012.

Kallmann, H. I. **Neutron Radiography.** Research, v. 1, p. 7, 1947.

Kang, W. X.; Yang, Q. Q.; Liang, R. P. **The Comparative Research on Image Segmentation Algorithms.** First International Workshop on Education Technology and Computer Science. Wuhan, Hubei, China: IEEE: 5 p. 2009.

- Karthik, M. M.; Mander, J. B.; Hurlebaus, S. **ASR/DEF Related Expansion In Structural Concrete: Model Development And Validation**. Construction Building Material, v. 128, p. 10, 2016.
- Ketcham, R. A.; Hanna, R. D. **Beam Hardening Correction For X-Ray Computed Tomography Of Heterogeneous Natural Materials**. Computers and Geosciences, v. 67, p. 13, 2014.
- Khelil, N. **Traitement Electrochimiques de Betons Atteint de Reaction Sulfatique Interne**. PhD. Dissertation. Laboratoire Materiaux et Durabilite des Constructions, Universite Toulouse 3 Paul Sabatier, Toulouse, France. p. 190, 2014.
- Khondker, A.; Lakhani, S. **X-Ray Diffraction: A Comprehensive Explanation for Multipurpose Research**. International Journal of Interdisciplinary Research and Innovations, v. 3, n. 1, p. 5, 2015.
- Kim, F. H. **Dual-Modality (Neutron and X-Ray) Imaging for Characterization of Partially Saturated Granular Materials and Flow Through Porous Media**. PhD Dissertation. Department of Civil Engineering, University Of Tennessee, 2013.
- Kim, F. H. et al. **Characterizing Partially Saturated Compacted-Sand Specimen Using 3D Image Registration Of High-Resolution Neutron and X-Ray Tomography**. Journal of Computing In Civil Engineering, v. 29, n. 6, 2015.
- Klug, H. P.; Alexander, L. E. **X-Ray Diffraction Procedures for Polycrystalline and Amorphous Material**. New York: Wiley Interscience, 1974.
- Krumm, M.; Kasperl, S.; Frantz, M. **Reducing Non-Linear Artifacts of Multi-Material Objects in Industrial 3D computed tomography**. NDT&E International, v. 41, p. 242-251, 2008.
- Kurdowski, W. **Kurdowski Symposium Science of Cement and Concrete, June 20-21, 2001**. Krakow, Poland: Krakow Akapit, 2001.
- Lamanna, J. et al. **Neutron and X-ray Tomography (NeXT) System for Simultaneous, Dual Modality Tomography**. Review of Scientific Instruments, v. 88, n. 11, p. 113702, 2017.
- Lamanna, J. et a. **Simultaneous Neutron and X-Ray Tomography for Quantitative Analysis of Geological Samples**. American Geophysical Union, Fall General Assembly 2016.
- Landis, E. N. et al. **Technique to Measure 3D Work-of-Fracture of Concrete in Compression**. Journal of Engineering Mechanics, v. 125, n. 6, 1999.

Landis, E. N. et al. **Cracking Damage And Fracture In Four Dimensions**. Material Structures, v. 40, p. 8, 2007.

Lawrence, C. D. **Mortar Expansions Due to Delayed Ettringite Formation: Effects of Curing Period and Temperature**. Cement and concrete research, v. 25, n. 4, p. 903-914, 1995.

Lee, D. et al. **Learning Similarity measure for Multi-Modal 3D Image registration**. 2009 IEEE Computer Society Confereneec on Computer Vision and Pattern Recognition Workshops: 186-193 p. 2009.

Lesnicki, K. J. et al. **Characterization of ASR damage in Concrete Using Nonlinear impact Resonance Acoustic Spectroscopy technique**. NDT&E International, v. 44, p. 7, 2011.

Lewis, M. **Heat Curing and Delayed Ettringite Formation in Concretes**. PhD Thesis. University of London: Imperial College of Science, Technology and Medecine 1996.

Lewis, M. C.; Scrivener, K. L.; Kelham, S. **Heat Cured and Delayed Ettringite Formation**. Material Research Society Symposium Proceedings, v. 370, p. 11, 1994.

Li, G.; Le Bescop, P.; Moranville, M. **The U phase formation in cement-based systems containing high amounts of Na<sub>2</sub>SO<sub>4</sub>**. Cement and Concrete Research, v. 26, n. 1, p. 9, 1996.

Liu, X. et al. **Quantitative Imaging of Element Composition and Mass Fraction Using Dual-energy CT: Three-material Decomposition**. The International Journal of Medical Physics Research and Practice, v. 36, n. 5, p. 8, 2009.

Livingston, R., A.; Amde, A. M.; Wallace, D. **Nondestructive Test Field Survey for Assessing the Extent of Ettringite-Related Damage in Concrete Bridges**. 10th International Symposium on the Destructive of Materials. Karuizawa, Japan 2000.

Livingston, R. A. **Fractal Nucleation and Growth Model for the Hydration of Tricalcium Silicate**. Cement and Concrete Research, v. 30, p. 1853-1860, 2000.

Lu, S.; Landis, E. N.; Keane, D. T. **X-Ray Microtomographic Studies Of Pore Structure And Permeability In Portland Cement Concrete**. Materials and Structures, v. 39, p. 10, 2006.

Lucero, C. L. et al. **Using Neutron Radiography to Quantify Water Transport and the Degree of Saturation in Entrained Air Cement Based Mortar**. Physics Procedia, v. 69, p. 9, 2015.

- Ludwig, U. **Problems of Ettringite Formation in Heat Treated Mortars and Concretes**. 11th Building materials and Silicate Conference. SERVICE, E. E. M. Witzmannsberg, Germany: pp. 164-177 p. 1991.
- Lura, P. et al. **Internal Curing with Lightweight Aggregate Produced from Biomass-Derived Waste**. *Cement and Concrete Research*, v. 59, p. 10, 2014.
- Maes, F. et al. **Multimodality Image Registration by Maximization of Mutual Information**. *IEEE Transactions on Medical Imaging*, v. 16, n. 2, p. 12, 1997.
- Manke, I. et al. **In Situ investigation of the Discharge of Alkaline Zn-MnO<sub>2</sub> Batteries with Synchrotron X-ray and Neutron Tomographies**. *Applied Physics Letters*, v. 90, 2001.
- Mannes, D. et al. **Beyond the Visible : Combined Neutron and X-ray Imaging of an Altar Stone from the Former Augustinian Church in Fribourg, Switzerland**. *Archeometry*, v. 56, p. 11, 2014.
- Mannes, D. et al. **Combined Neutron and X-ray Imaging for Non-invasive Investigation of Cultural Heritage Objects**. *Physics Procedia*, v. 69, p. 8, 2015.
- Marangoni, A. G. **On the Use and Misuse of the Avrami Equation in Characterization of the Kinetics of Fat Crystallization**. *Journal of American Oil Chemistry Society*, v. 75, n. 10, p. 1465-1467, 1998.
- Marusin, S. L. **SEM Studies of Concrete Failures Caused by Delayed Ettringite Formation**. 4th Euroseminar on Microscopy Applied to Building Material, Visby, Sweden, 1993.
- Marusin, S. L. **A Simple Treatment to Distinguish Alkali-Silica Gel from Delayed Ettringite Formations in Concrete**. *Magazine of Cement Research*, v. 168, p. 4, 1994.
- Marusin, S. L.. **Sample Preparation - the Key to SEM Studies of Failed Concrete**. *Cement and Concrete Composites*, v. 17, n. 4, p. 8, 1995.
- Matos, L. et al. **The Application of Fluorescence Microscopy and Scanning Electron Microscopy in the Detection of Delayed Ettringite Formation in Concrete**. *Materials Science Forum*, v. 636-637, p. 6, 2010.
- McMorris, N. **The Use of the Impact Echo Method to Detect Delayed Ettringite Formation**. Master Thesis (M S ). Department of Civil and Environmental Engineering, University of Maryland, College Park, 2003.
- McMorris, N. **Linear and Non-Linear Frequency Domain Techniques for Processing Impact Echo Signals to Evaluate Distributed Damage in Concrete**. PhD. DISSERTATION.

Department of Civil and Environmental Engineering, University of Maryland, College Park, College Park, Maryland, USA, p. 165, 2009

Mehta, P. K. **Mechanism of Expansion Associated with Ettringite Formation**. Cement and Concrete Research, v. 3, n. 1, p. 6, 1973.

Meinel, D. et al. **Examination of Damage Processes in Concrete with CT. 5th Conference on Industrial Computed Tomography (iCT2014)**, Wels, Australia, 2014.

Menedez, E.; Vega, L. **Analysis of the Behaviour of the Structural Concrete after the Fire at the Windsor Building in Madrid**. Fire materials, v. 34, p. 13, 2009.

Metalssi, O. O.; Godart, B.; Toutlemonde, F. **Effectiveness of Nondestructive Methods for the Evaluation of Structures Affected by Internal Swelling Reactions: a Review of Electric, Seismic and Acoustic Methods Based on Laboratory and Site Experiences**. Experimental Techniques, v. 39, n. 2, p. 12, 2015.

Morgan, I. L. et al. **Examination of Concrete by Computerized Tomography**. International Concrete Abstracts Portal, v. 77, n. 1, p. 5, 1980.

Muhamad, M. N. et al. **A Time Resolve Synchrotron Energy Dissipative Diffraction Study of the Dynamic Aspects of the Synthesis of Ettringite During Mine Packing**. Cement and Concrete Research, v. 23, n. 2, p. 6, 1993.

Nawy, E. G. **Concrete Construction Engineering Handbook**. 2nd. Boca Raton: CRC Press, 2008.

Oberholster, R. E.; Maree, N.; Brand, J. H. D. **Cracked Prestressed Concrete Railway Sleepers: Alkali-Silica Reaction or delayed Ettringite Formation**. Sixth International Conference on Cement Microscopy. London, UK: pp. 739-749 p. 1992.

Odler, I.; Abdul-Manula; Zhongya, L. **Effect of Hydration Temperature on Cement Paste Microstructure**. Material Research Society, Symposium Proceedings. p.pp. 181-185. 1987.

Odler, I.; Chen, Y. **On the Delayed Expansion of Heat Cured Portland cement Pastes and Concretes**. Cement and Concrete Research, v. 18, p. 5, 1996.

Pavoine, A. et al. **Impact of Drying and Wetting Cycles on Differed Ettringite Formation in Concrete**. Materials and Structures, v. 36, n. 9, p. 7, 2003.

Petrov, N.; Tagnit-Hamou, A. **Is Microcracking Really a Precursor to Delayed Ettringite Formation and Consequent Expansion?** ACI Materials Journal, v. 101, n. 6, p. 6, 2004.

Pettifer, K.; Nixon, P. J. **Alkali Metal Sulfate-A Factor Common to Both Alkali Aggregate Reaction and Sulfate Attack on Concrete.** Cement and Concrete Research, v. 10, p. 9, 1980.

Radon, J. **On the Determination of Functions from their Integral Values Along Certain Manifolds.** IEEE Transactions on Medical Imaging, v. MI-5, n. 4, p. 7, 1986.

Ramadan, E. **Experimental and Theoretical Study of Delayed Ettringite Damage in Concrete.** PhD Dissertation. Department of Civil Engineering Dept, University of Maryland, College Park, MD, 2000.

**RASHID, S.; BARNES, P.; TURILLAS, X. The Rapid Conversion of High Alumina Cement Hydrates as Revealed by Synchrotron Energy Dispersive X-Ray Diffraction.** Advances in Cement Research, v. 4, n. 14, p. 7, 1992.

Roubin, E. et al. **A Nonlinear Meso–Macro Approach to Modelling Delayed Ettringite Formation and Concrete Degradation.** Materials and Structures, v. 47, n. 11, p. 10, 2014.

Sabuncu, M. R. **Entropy-Based Image Registration.** PhD Dissertation. Department of Electrical Engineering, Princeton University, Princeton, NJ. 2006.

Sahu, S.; Thaulow, N. **Delayed Ettringite Formation in Swedish Concrete Railroad Ties.** Cement and Concrete Research, v. 34, p. 7, 2004.

Salgues, M. et al. **DEF Modelling Based on Thermodynamic Equilibria and Ionic Transfers for Structural Analysis.** European Journal of Environmental and Civil Engineering, p. 26, 2014.

Scherer, G. W. **Christallization in Pores.** Cement and Concrete Research, v. 29, p. 1347-1358, 1999.

Scrivener, K. L.; Damidot, D.; Famy, C. **Possible Mechanisms of Expansion of Concrete Exposed to Elevated Temperatures During Curing (Also known as DEF) and Implications for Avoidance of Field Problems.** Cement, Concrete and Aggregates, v. 21, n. 1, p. 9, 1999.

Scrivener, K. L.; Pratt, P. L. **Microstructural Studies of Hydration of C3A and C4AF Independently and in Cement paste.** Proceeding of the British Ceramic Society, v. 35, 1984.

Seignol, J. F.; Baghdadi, N.; Toutlemonde, F. **A Macroscopic Chemo - Mechanical Model Aimed at Reassessment of Delayed - Ettringite - Formation Affected Concrete Structures.** In: Fischinger, M., First International Conference on Computed Technology in Concrete Structures (CTCS), Jeju, Korea, 2009.

Sellier, A.; Multon, S. **Chemical Modeling of Delayed Ettringite Formation for Assessment of Affected Concrete Structures**. Cement and Concrete Research, v. 108, p. 15, 2018.

Shayan, A. **Behavior of Precast Prestressed Concrete Railway Sleepers Affected by AAR. 5th CANMET/ACI International Conference on Fly Ash, Slag, Silica Fume and Natural Pozzolans in Concrete**, (N.R. Swamy Symposium), Milwaukee, USA, 4-9 June 1995.

Shimada, Y. et al. **Chemical Path of Ettringite Formation in Heat-Cured Mortar and Its Relationship to Expansion: A Literature Review**. Portland Cement Association. Skokie, Illinois, USA, p.51. 2005

Stacey, W. M. **Nuclear Reactor Physics, 2nd ed.** Wiley-VCH, 2007.

Starink, M. J. **On the Meaning of the Impingement Parameter in Kinetic Equations for Nucleation and Growth Reaction**. Journal of Materials Science, v. 36, p. 9, 2001.

Stock, S. R. et al. **X-ray Microtomography (microCT) of the Progression of Sulfate Attack of Cement Paste**. Cement and Concrete Research, v. 32, p. 1673-1675, 2002.

Stutzman, P. E. **Scanning Electron Microscopy in Concrete Petrography**. Journal of American Ceramic Society, p. 14, 2001.

Suthakar, R. J. et al. **Study of Image Fusion- Techniques, Method and Applications**. International Journal of Computer Science and Mobile Computing, v. 3, n. 11, p. 469 – 476, 2014.

Tantawy, M. A. **Effect of High Temperature on the Microstructure of Cement Paste**. Journal of Material Science and Chemical Engineering, v. 5, p. 16, 2017.

Taylor, H. F. W.; Famy, C.; Scrivener, K. L. **Delayed Ettringite Formation**. Cement and Concrete Research, v. 31, n. 5, p. 11, 2001.

Thaulow, N.; Johansen, V.; Hjorth, J. **What Caused Delayed Ettringite Formation?** Rambol Bulletin, v. 60, 1996.

Thewlis, J. **Neutron Radiography**. British Journal of Applied Physics, v. 7, n. 10, p. 6, 1956.

Thomas, J. J. **A new Approach to Modeling the Nucleation and Growth Kinetics of the Tricalcium Silicate Hydration**. Journal of the American Ceramic Society, v. 90, n. 10, p. 7, 2007.

Torrens-Serra, J. et al. **Non-Isothermal Kinetic Analysis of the Crystallization of Metallic Glasses Using the Master Curve Method**. Materials, v. 4, p. 13, 2011.

Trtik, P. et al. **Neutron Tomography measurement of Water release from Superabondant polymers in Cement paste.** International RILEM Conference on Material Science-MATCI, 2010, Aachen, Germany.

Trtik, P. **Release of Internal Curing Water from Lightweight Aggregates in Cement Paste Investigated by Neutron and X-ray Tomography.** Nuclear Instruments and Methods In Physics Research, v. 651, n. 1, p. 6, 2011.

Vedalkshmi, R.; Raj, S.; Palaniswamy, N. **Identification of Various Chemical Phenomena in Concrete Using Thermal Analysis.** Indian Journal of Chemical Technology, v. 15, p. 9, 2008.

Viola, P.; Wells Iii, W. M. **Alignment by Maximization of Mutual Information.** International Journal of Computer Vision, v. 24, n. 2, p. 18, 1997.

Vontobel, P.; Lehmann, E.; Carlson, W. D. **Comparison of X-ray and Neutron Tomography Investigation of Geological Material.** IEEE Transactions of nuclear Science, v. 52, n. 1, p. 21, 2005.

Wei-Shan, C. et al. **Simultaneous Neutron and X-ray Imaging of 3D Kerogen and Fracture Structure in Shales.** SPWLA 58th Annual Logging Symposium. Oklahoma City, Oklahoma, USA 17-21 June 2017.

Wyrzykowski, M. et al. **Plastic Shrinkage of Mortars with Shrinkage Reducing Admixture and Lightweight Aggregates Studied by Neutron Tomography.** Cement and Concrete Research, v. 73, p. 8, 2015.

Yan, P. et al. **The Semiquantitative Determination and Morphology of Ettringite in Paste Containing Expansive Agent Cured in Elevated Temperature.** Cement and Concrete Research, v. 31, n. 9, p. 1285-1290, 2001.

Yang, R.; Lawrence, C. D.; Sharp, J. H. **Delayed Ettringite Formation in 4-Year old Cement Pastes.** Cement and Concrete Research, v. 26, n. 11, p. 11, 1996.

Yang, R.; Lawrence, C. D.; Sharp, J. H.. **Effect of Type of Aggregate on Delayed Ettringite Formation.** Advances in Cement Research, v. 11, n. 3, p. 14, 1999.

Zhang, J. K.; Yan, W.; Cui, D. M. **Concrete Condition Assessment Using Impact-Echo Method and Extreme Learning machines.** Sensors (Basel), v. 16, n. 4, 2016.

Zheng, J. J.; Li, C. Q.; Zhou, X. Z. **Thickness of Interfacial Transition Zone and Cement Content Profiles Around Aggregates.** Magazine of Concrete Research, v. 57, n. 7, p. 10, 2005.

Zitova, B.; Flusser, J. **Image Registration Methods: A Survey.** Image and Vision Computing, v. 21, n. 11, p. 24, 2003.

## List of Scientific Contributions

### Papers:

1. Serge Feuze, Richard A. Livingston, Amde M. Amde, Jacob M. Lamanna, David L. Jacobson and Daniel S. Hussey “*Simultaneous Neutron and X-Ray Quantitative Computed Tomography of Concrete Deterioration*” 11th World Conference on Neutron radiography, Sydney, Australia, 2-7 September 2018. (Accepted)
2. Serge Feuze, Richard A. Livingston, Amde M. Amde “*Mechanism of Concrete Deterioration Due to Delayed Ettringite Formation*” (Manuscript)
3. Serge Feuze, Richard A. Livingston, Amde M. Amde “*The Influence of Thermal Cycles and Potassium on the Damage Mechanics of Delayed Ettringite Formation*” 10<sup>th</sup> Conference on Fracture Mechanics of Concrete and Structures (FRAMCOS), 24-26 June, Bayonne, France (Accepted)

### Presentations:

1. Richard A. Livingston, Serge Feuze, Amde M. Amde, Jacob M. LaManna, David L. Jacobson and Daniel S. Hussey “*Current Research In Delayed Ettringite Formation at the University of Maryland*” 9<sup>th</sup> advances in cement Based Material, 12 June, Penn State, PA.
2. Richard A. Livingston, Serge Feuze, Amde M. Amde, Jacob M. LaManna, David L. Jacobson and Daniel S. Hussey “*Fusion of Simultaneous Neutron and X-Ray Computed Tomography Images of Concrete Deterioration*” International Symposium on Nondestructive testing in Civil Engineering (NDT-CE) 2018, New Brunswick, NJ, 27-29 August 2018.
3. Serge Feuze, Richard A. Livingston, Amde M. Amde, Jacob M. Lamanna, David L. Jacobson and Daniel S. Hussey “*Analysis of Concrete Deterioration By Simultaneous Neutron and X-Ray Tomography*” 9<sup>th</sup> American Conference on Neutron Scattering, 27 June 2018, College Park, MD.
4. Richard A. Livingston, Serge Feuze, Amde M. Amde, Jacob M. LaManna, David L. Jacobson and Daniel S. Hussey “*Nondestructive Measurement of Concrete Deterioration by Simultaneous Neutron and X-Ray Quantitative Computed Tomography*” 10th Conference on Fracture Mechanics of Concrete and Structures (FRAMCOS), 24-26 June, Bayonne, France.

### Posters:

1. Richard A. Livingston, Serge Feuze, Amde M. Amde, Jacob M. LaManna, David L. Jacobson and Daniel S. Hussey “*Simultaneous Neutron and X-ray Tomography for Quantitative Analysis of Concrete Deterioration*” ASTM C01-C09 Symposium on Advances in Cement Analysis and Concrete Petrography, 27 June 2018, San Diego, CA